

Novel Optical Sensors for High Temperature Measurement in Harsh Environments

Yibing Zhang

Dissertation submitted to the Faculty of the
Virginia Polytechnic Institute and State University
in partial fulfillment of the requirements for the degree of

Doctor of Philosophy
in

Electrical and Computer Engineering

Dr. Anbo Wang, Co-Chairman
Dr. Ahmad Safaai-Jazi, Co-Chairman
Dr. Gary R. Pickrell
Dr. Ira Jacobs
Dr. Roger H. Stolen

July 24, 2003

Blacksburg, Virginia

Keywords: Fiber optic sensors, Temperature, Birefringence, Polarimetry,

Low-coherence interferometry

Copyright 2003. Yibing Zhang

Novel Optical Sensors for High Temperature Measurement in Harsh Environments

Yibing Zhang

(Abstract)

Accurate measurement of temperature is essential for the safe and efficient operation and control of a vast range of industrial processes. Many of these processes involve harsh environments, such as high temperature, high pressure, chemical corrosion, toxicity, strong electromagnetic interference, and high-energy radiation exposure. These extreme physical conditions often prevent conventional temperature sensors from being used or make them difficult to use. Novel sensor systems should not only provide accurate and reliable temperature measurements, but also survive the harsh environments through proper fabrication material selections and mechanical structure designs.

This dissertation presents detailed research work on the design, modeling, implementation, analysis, and performance evaluation of novel optical high temperature sensors suitable for harsh environment applications. For the first time to our knowledge, an optical temperature sensor based on the broadband polarimetric differential interferometric (BPDI) technology is proposed and tested using single crystal sapphire material. With a simple mechanically structured sensing probe, in conjunction with an optical spectrum-coded interferometric signal processing technique, the proposed single crystal sapphire optical sensor can measure high temperature up to 1600 °C in the harsh environments with high accuracy, corrosion resistance, and long-term measurement stability. Based on the successfully demonstrated sensor prototype in the laboratory, we are confident of the next research step on sensor optimization and scale-up for full field implementations. The goal for this research has been to bring this temperature sensor to a level where it will become commercially viable for harsh environment applications associated with industries.

Acknowledgements

I wish to express my deepest appreciation to Dr. Anbo Wang, and Dr. Ahmad Safaai-Jazi, for serving as my advisors. Without their patient, guidance and constant supports, this dissertation would not have been possible. As mentors and friends, they continually and convincingly conveyed a spirit of adventure and an excitement in regard to research and scholarship during the past years. With their dedication, confidence and incredible achievements, they will continue to be my mentors shedding light on my future journey.

I also would like to sincerely thank Dr. Gary R. Pickrell, Dr. Guy J. Indebetouw, Dr. Ira Jacobs, and Dr. Roger H. Stolen, for serving on my committee and for their encouragements and valuable suggestions to improve the quality of the work presented here. I hope Dr. Guy J. Indebetouw get well soon.

My gratitude also goes to all of my colleagues and friends at Center for Photonics (CPT), which has been shared as a home. Among them, special thanks goes to former CPTers, Dr. Russll G. May, Dr Hai Xiao, Dr. Bing Qi, and Jiangdong Deng, who introduced me to CPT three years ago, as well as current CPTers, Yan Zhang and Xiaopei Chen, for their valuable suggestions and supports to this presented work. I am also grateful to Debbie Collins, Kathy Acosta and Bill Cockey, they have made the CPT a place to work with great pleasure.

Finally, words alone cannot express the thanks I own to my loving wife, Chinge, for her caring, encouragement and sacrifice; to my parents, who raised me and trust me with their endless love; and to my two young sisters, Shudan and Jialing, they remind me that family is more important than any number of academic degrees.

Table of Content

Abstract.....	ii
Acknowledgements	iii
Table of Content.....	iv
List of Figures.....	vii
List of Tables	xiii
Chapter 1. Introduction	1
1.1 Background information on the proposed research	1
1.2 Review of non-optical techniques for temperature measurements	2
1.2.1 High temperature thermocouples	2
1.2.2 Acoustic methods.....	3
1.3 Review of optical techniques for temperature measurements	4
1.3.1 Remote pyrometers	4
1.3.2 Thermometers based on thermal expansion.....	5
1.3.3 Fluorescence thermometers	5
1.3.4 Thermometers based on optical scattering.....	6
1.4 Industrial needs for novel high temperature sensors.....	6
1.5 Special requirements for temperature sensors in coal gasifier.....	10
1.6 Scope of research	12
Chapter 2. Principles of operation of the designed optical sensors.....	13
2.1 Optical sensing elements design	14
2.1.1 Review of EFPI sapphire fiber sensor	14
2.1.2 Broadband polarimetric sapphire sensor.....	17
2.2 Signal processing units	20
2.2.1 Review of signal processing methods for interferometric sensors	20
2.2.2 SCIIB signal processor	21
2.2.3 Spectral domain white light interferometric signal processor	22
2.3 Blackbody radiation subtraction	25
2.4 Configurations of designed temperature sensor systems	27
2.5 Mathematical model for BPDI temperature sensor	30
2.6 Major advantages of BPDI sensor system	34
Chapter 3. Design and implementation of temperature sensor systems.....	36
3.1 Fabrication materials for sensing probes	36

3.1.1 Properties of single crystal sapphire	37
3.1.2 Properties of single crystal zirconia.....	40
3.2 Implementation of sensing probes	41
3.2.1 A sensing probe with a sapphire disk, zirconia prism (SDZP) structure.....	41
3.2.2 A sensing probe with a sapphire prism (SP) structure.....	44
3.2.3 Total internal reflection in the sensor probe	48
3.3 Signal processor and software implementation	49
3.3.1 Signal processor implementation.....	49
3.3.2 Signal processing algorithm development.....	52
3.3.3 Software design and implementation.....	55
3.4 Overview of BPDI temperature sensor system.....	62
Chapter 4. System noise analysis and performance optimization.....	64
4.1 Optical spectrum induced noise.....	64
4.1.1 Wavelength drift	65
4.1.2 Spectral bandwidth broadening/narrowing effects	71
4.2 Degradation effect due to the visibility of the interference spectrum.....	73
4.3 Optical birefringence effects.....	77
4.3.1 Rotation about the slow-axis (i.e. C-axis).....	80
4.3.2 Rotation about the fast-axis (i.e. A-axis)	83
4.3.3 Rotation about an axis 45° from the slow-axis/fast-axis.....	86
4.4 Opto-electronic noise in spectrum measurements	88
4.5 Optical fiber induced noises.....	91
4.6 Summary of system noises and their optimization	92
4.7 Power budget	98
Chapter 5. Performance evaluation of designed temperature sensors	101
5.1 Definitions of performance characteristics	101
5.2 Characterization of white light signal processor.....	103
5.2.1 Capability of compensating optical source power fluctuations	103
5.2.2 Capability of compensating optical fiber transmission loss	106
5.2.3 Capability of compensating temperature fluctuations	107
5.3 Blackbody radiation subtraction	108
5.4 Calibration of BPDI sensing system.....	111
5.4.1 Construction of temperature calibration system	111
5.4.2 Temperature sensor calibration.....	112
5.5 Performance evaluations of BPDI sensing system	115

5.5.1 Repeatability of the measurements	115
5.5.2 Evaluation of accuracy.....	117
5.5.3 Long-term stability tests	118
5.5.4 Sensitivity (resolution) tests.....	120
5.5.5 Hysteresis in the temperature measurements.....	121
5.5.6 Frequency response.....	123
Chapter 6 Expansion of the BPDI sensing technology for other measurements	127
6.1 Multi-parameter measurement toolbox based on optical birefringence	127
6.2 Pressure sensor with temperature compensation capability.....	129
6.3 Rotary displacement sensor	131
6.4 High electrical voltage sensor.....	132
Chapter 7 Conclusions and recommendations for future work.....	134
7.1 Conclusions.....	134
7.2 Suggestions for future works	137
Reference	140
Appendix A: Determination of the refraction angle and refractive index corresponding to the extraordinary waves in the single crystal sapphire	146
Appendix B: Acronym.....	148
VITA	150

List of Figures

Figure 2.1 Schematic design of the sapphire fiber based EFPI sensor.....	15
Figure 2.2 Interference in the FP cavity formed by multimode sapphire fibers.....	16
Figure 2.3 Output spectrum from the EFPI sapphire fiber sensor with cavity length=6.5 μ m.....	16
Figure 2.4 Output spectrum from the EFPI sapphire fiber sensor with cavity length=21.8 μ m.....	16
Figure 2.5 Principle of an interference device using polarized light waves.....	17
Figure 2.6 Conceptual schematic design of the sensing head: broadband polarimetric differential interferometry (BPDI)	18
Figure.2.7 Measured output optical interference signal $I(\lambda)$ from the BPDI sensor ...	19
Figure 2.8 Illustration of the principle of the SCIIB fiber optic signal processor.....	21
Figure 2.9 Illustration of a semi-linear operating range of the interference fringes.....	22
Figure 2.10 Basic structure of optical fiber sensor with white light interferometry.....	23
Figure 2.11 Normalized optical interference fringes for different OPD values (with $\gamma=1$).....	24
Figure 2.12 Theoretical intensity curves of the blackbody radiation above 1000 $^{\circ}$ C for the wavelength range: 800~900nm.	26
Figure 2.13 Relation between blackbody radiation and interference fringes at different temperatures.	26
Figure 2.14 Amplitude response of the IIR filter.....	27
Figure 2.15 Interference curve with blackbody radiation (at 1350 $^{\circ}$ C) subtraction.....	27
Figure 2.16 Temperature measurement systems based on designed sensing elements and detecting units.....	27
Figure. 2.17 Schematic design of the single-crystal sapphire based BPDI optical high temperature sensor.....	29
Figure. 2.18. Interfering mechanism for polarimetric differential interferometer.....	31
Figure 3.1 The approximate transmission bands of standard- and UV-grade sapphire (window thickness of 0.039 inch).	38

Figure 3.2 Hexagonal inner structure of single-crystal sapphire material.....	38
Figure 3.3 A sensing probe with Sapphire Disk Zirconia Prism (SDZP) structure.....	43
Figure 3.4 Optical propagation in the special crystallographic oriented single crystal sapphire right angle prism.	46
Figure 3.5 Single crystal sapphire right angle prism.....	47
Figure 3.6 Sapphire Prism (SP) structure sensing probe.....	47
Figure 3.7 Single channel spectrum domain white light system.....	51
Figure 3.8 Block diagram of the implementation of the OPD calculation algorithm.	56
Figure 3.9 Blackbody radiation subtraction.....	59
Figure 3.10 Electrical square wave used to modulate the LED.....	59
Figure 3.11 Output optical signal from the modulated LED.....	60
Figure 3.12 The mass-centroid method for peaks locating in the spectrum.....	61
Figure 3.13 BPDI system overview.....	62
Figure 4.1 Gaussian spectral intensity profile from a low coherence source (LED) ...	65
Figure 4.2 Central wavelength of the LED dependence on the temperature.....	66
Figure 4.3 Simulated results of the normalized spectrum with center wavelength shift effect.....	68
Figure 4.4 Measurement results of the normalized spectrum at 45°C (the reference is acquired at 20°C)	68
Figure 4.5 OPD measurement uncertainties caused by center wavelength shift ($\delta\lambda$) ($\gamma=1$, $\lambda_p=857\text{nm}$, $L=30\mu\text{m}$, $w=60\text{nm}$).....	70
Figure 4.6 Temperature uncertainty caused by center wavelength shift ($\delta\lambda$) ($\gamma=1$, $\lambda_p=857\text{nm}$, $L=30\mu\text{m}$, $w=60\text{nm}$)	71
Figure 4.7 OPD measurement uncertainties caused by the bandwidth changes (δw) ($\gamma=1$, $\lambda_p=857\text{nm}$, $L=30\mu\text{m}$, $w=60\text{nm}$)	73
Figure 4.8 Temperature uncertainty caused by the bandwidth changes (δw) ($\gamma=1$, $\lambda_p=857\text{nm}$, $L=30\mu\text{m}$, $w=60\text{nm}$)	73
Figure.4.9 Misalignment between the optical polarizer and the sensing element.	74
Figure 4.10. Decomposition and interference of the linearly polarized input light in the polarimeter.	75
Figure 4.11 Visibilities dependence on the misalignment angle α between the light	

polarization direction and principal axes of the sensing element.....	76
Figure 4.12 Experimental interferograms with different visibilities.	77
Figure 4.13 Measured temperature deviation caused by the changes in the visibility of the interferogram.....	77
Figure 4.14 Method of the index ellipsoid to determine the refractive indices of light beams propagating along s direction.	78
Figure 4.15 The refractive index ellipsoid for single crystal sapphire.....	79
Figure4.16 Optical refractive index ellipse for the rotation about the s-axis of the sensing element.....	80
Figure 4.17 Refractive indices and birefringence vs. wavelength for the sapphire sensing element.....	81
Figure 4.18 (a) Refraction angles of the ordinary wave and the extraordinary waves (rotation about the s-axis). (b) The refraction angle difference between the ordinary wave and the extraordinary wave (rotation about the s-axis)	82
Figure.4.19 Sensing element rotation effect on the optical path difference (rotation about the s-axis).	82
Figure4.20. Sensing element rotation effects along s-axis on the OPD measurements.	82
Figure 4.21. Optical refractive index ellipse for the rotation about the f-axis of the sensing element.....	83
Figure 4.22. Refractive index vs. light incident angle for the extraordinary waves.....	84
Figure 4.23. (a) Refraction angles of the ordinary wave and the extraordinary wave (rotation about the f-axis) (b) The refraction angle difference between the ordinary wave and the extraordinary wave (rotation about the f-axis)	85
Figure 4.24. Rotation effects on the optical path difference (rotation about the f-axis)	85
Figure 4.25 Effect of rotation about the f-axis on the OPD measurements.	86
Figure 4.26 Rotation about the 45° axis relative to the s-axis of sensing element.	87
Figure.4.27 Effect on the OPD measurements of rotation about the axis at 45°	

relative to the f-axis of the sensing element.	87
Figure 4.28 CCD array for the optical signal detection in the optical spectrometer.....	88
Figure 4.29 Opto-electronic noise effects on the valley point locations	
determinations.....	90
Figure 4.30 Opto-electronic noise effects on the temperature	
measurement uncertainties.....	91
Figure 4.31 The measured interference spectrum after dark current subtraction.....	94
Figure 4.32 Simulated result for spectrum curve smoothing with small	
window width (w=5)	95
Figure 4.33 Simulated result for spectrum smoothing with a large window	
width (w=80)	95
Figure 4.34 Measured spectrum after curve-smoothing with a window	
width (w=61)	96
Figure 4.35 Optical power losses in the BPDI system.	99
Figure 5.1. Output power levels of the LED with different driving currents.....	104
Figure 5.2. Output spectra of the LED with different driving currents.	104
Figure 5.3 Normalized interference fringes for the LED with different driving	
currents.....	105
Figure 5.4 Temperature deviations vs. optical source output powers.....	105
Figure 5.5 Normalized interference fringes for transmission fiber with different	
attenuations.....	106
Figure.5.6 Temperature deviation vs transmission fiber loss.....	107
Figure.5.7 Experimental results of temperature compensation with the first order	
approximation.....	108
Figure 5.8 Normalization of the optical spectrum.....	109
Figure 5.9 Blackbody radiation effect on the measurements of optical	
temperature signatures.....	109
Figure 5.10 Normalized optical spectra measured at different high temperature	
levels.....	110
Figure 5.11 Temperature acquisition subsystem for the calibration purpose.....	111

Figure 5.12 Real time temperature is related to an OPD value through a GUI interface.....	112
Figure 5.13 Applied temperature during the sensor calibration process.....	113
Figure 5.14 OPDs measured with the BPDI system during the sensor calibration process.....	114
Figure 5.15 The BPDI sensor system calibration curve for a sapphire sensing disk with thickness of 1.5mm.....	114
Figure 5.16 The BPDI sensor system calibration curve for a sapphire sensing prism (equivalent to a sensing disk with thickness of 8mm)	115
Figure 5.17 Repeatability testing results of the temperature measurements.....	116
Figure 5.18 Deviation of the measured temperatures with respect to the reference data.....	116
Figure 5.19 Optical sensing system measurement results vs a B-type thermocouple measured temperatures.	117
Figure 5.20 Deviation between the temperature measurement results from the B type thermocouple and the optical sensing system.....	117
Figure 5.21 Long-term stability testing results.....	120
Figure 5.22 Histogram of temperature measurement.....	121
Figure 5.23 Hysteresis of the BPDI temperature sensor.....	122
Figure 5.24 Rise time characterization of the BPDI sensor system with boiling water.....	126
Figure 5.25 Rise time characterization of the BPDI sensor system with high temperature furnace.....	126
Figure 6.1 An one-end structure version BPDI sensor system	128
Figure 6.2 A two-end structure version BPDI sensor system.....	128
Figure 6.3 Schematic design of BPDI based optical single crystal sapphire high-pressure sensing head.....	130
Figure 6.4 Applied pressure signals on the sapphire sensing element.....	130
Figure 6.5 Pressure signals from the optical sensor.....	130
Figure 6.6 Pressure measurements with the calibrated sapphire pressure sensor.....	130
Figure 6.7 Fiber Optic rotation sensor.....	131

Figure 6.8 Rotation angle measurements with the calibrated fiber optic rotation sensor.	132
Figure 6.9 Sensing head designs for electrical voltage measurement.	133
Figure 6.10 Electrical voltage sensor based on the BPDI technology.	133

List of Tables

Table 3.1 The key features of the optical spectrum analyzer USB2000.....	50
Table 4.1 Noise in the BPDI sensor system and compensation methods.....	93

Chapter 1. Introduction

1.1 Background information on the proposed research

As one of the seven basic quantities used in the SI (International System of Units) system, temperature is probably the most measured physical parameter since virtually every process in nature and in industry is temperature dependent. Its accurate measurement is essential for the safe and efficient operation and control of a vast range of industrial processes. Appropriate techniques and instrumentation are needed depending on temperature measurement requirements in different industrial processes and working environments.

The motivation of this research is to meet the recent increasing needs for temperature sensors capable of operating accurately and reliably in harsh environments, such as coal-based power generation and distribution industries, nuclear power industries, glass and metal manufacturing and processing industries and other high-temperature chemically corrosive environments. In general, optical sensors have many advantages over conventional electronic sensors for applications in harsh environments. These include: small size, light weight, immunity to electromagnetic interference (EMI), resistance to chemical corrosion, avoidance of ground loops, high sensitivity, large bandwidth, capability of remote operation, and potential capability of operating at high temperatures [1]. These advantages have promoted worldwide research activities in the area of optical fiber sensor technologies for harsh environments.

The sensor prototype developed in this research is intended for non-intrusive, direct high temperature measurement, in the primary and secondary stages of slagging gasifiers. These gasifiers are used in the coal-based power generation industries, where a sensor is required to withstand extremely harsh environments imposed by the high temperature, high pressure and corrosive chemical materials. Sponsored by the National Energy Technology Laboratory of the U.S. Department of Energy, the Center for Photonics Technology (CPT) at the Bradley Department of Electrical and Computer Engineering

of Virginia Tech is currently leading the effort in developing this optical sensor technology for real-time high temperature measurements, in collaboration with an industrial partner, Global Energy Technology, Inc.

1.2 Review of non-optical techniques for temperature measurements

In science, temperature is defined in terms of the amount of heat transferred in a Carnot cycle [2]. This is generally not the most practical way of measuring temperature, and in practice many different techniques are used depending on the temperature measurement requirements. In practice, every temperature measurement involves the use of certain calibrated transducers to convert a measurable quantity into a temperature value. Those transducers convert changes in the temperature into other measurable physical quantities, such as volumetric expansion (liquid-filled thermometer), dimensional change (bimetallic thermometer), electromotive force (thermocouple), resistance (resistance temperature detector - RTD), radiated energy (radiation thermometer), or some other characteristics of a material that varies reproducibly with temperature [3-4].

For high temperature measurements over 1000 °C, the existing non-optical measurement techniques are very limited. Possible choices include high temperature thermocouples and acoustic methods.

1.2.1 High temperature thermocouples

A thermocouple is an assembly of two wires of different metals joined at one end, the so-called hot end that will physically locate at the measuring position, and at the other end, the cold junction, that usually works as a reference at 0 °C. The open circuit voltage from these two wires, generated by an electromotive force (EMF) inside the wires, depends on the difference in temperature between the hot and the cold junctions as well as the Seebeck coefficient of the two wire metals. German physicist J.T. Seebeck discovered this thermoelectric effect phenomenon in 1821, so the voltage is accordingly called

Seebeck voltage. Through the known cold junction temperature, the temperature of the hot junction can be obtained from the measured Seebeck voltage.

There are more than 300 types of thermocouple available, which are formed by different metals. Eight types of them are standardized [4], including T, E, K, J, N, B, R, S type thermocouples. Different type thermocouples are characterized to measure temperature up to certain levels with different resolutions. For high temperatures over 1000 °C, Type B, R, S thermocouples are commercially available. In chemically corrosive environments, high temperature thermocouples that utilize precious metals are used and have a limited life of only a few days because of their susceptibility to attack from corrosive chemicals. They drift significantly under high temperature environments for a long-term operation.

1.2.2 Acoustic methods

It is well known that the speed of sound in a material depends on the temperature [5-6]. Temperature can thus be measured by detecting the speed of sound that propagates inside a material. This technology is especially useful for measuring gas temperature in a combustion chamber, where it is difficult to measure the temperature using inserted probes due to low thermal mass and low conductivity of gases, and the strong radiation coupling of the walls of the enclosure to the sensor at high temperatures. Using the gas itself as the temperature sensor overcomes these problems.

The main difficulty with the technique is that the speed of sound is strongly dependent on the composition of the gas along the path, which is generally not constant in the combustion chamber. Furthermore, soot particles slow the acoustic wave significantly, and will result in a large error. Another problem arises from refraction of the sound wave front by the density and temperature gradients in the chamber. These are often turbulent which distort the wave fronts, making the accurate determination of time of flight difficult. Since the sound wave travels with the gas, the apparent speed of sound will also be strongly affected by the flow velocity through the Doppler effect. Practical systems usually compensate for this effect by performing measurements in both directions. The

temperature measurement uncertainty claimed for this method is typically 30°C at 1000 °C [7].

1.3 Review of optical techniques for temperature measurements

Optical sensors are those instruments in which optical signals are changed in a reproducible way by an external physical stimulus such as temperature, pressure, strain, etc. An optical beam is characterized by several variables, such as intensity, spectrum, phase and state of polarization. Many different physical phenomena related to these characteristics are used to perform sensing functions.

Temperature sensors probably constitute the largest class of commercially available optical sensors. Besides bulk optics based optical sensors, a wide variety of temperature sensors using fiber optics have been developed [8]. They offer several significant advantages over electric sensors, such as small size, light weight, immunity to electromagnetic interference, etc. The main existing techniques for optical thermometry are remote pyrometers (or radiation thermometers), thermal expansion thermometers, fluorescence thermometers, and thermometers based on optical scatterings including Raman scattering and Raleigh scattering.

1.3.1 Remote pyrometers

All materials with temperatures above absolute zero degree emit electromagnetic radiation (thermal radiation) and the amount of thermal radiation emitted increases with temperature. The measurement of the amount of thermal radiation emitted by a material can therefore be used as an indicator of its temperature. The basic operating principle of the radiation thermometers is to measure part of the thermal radiation emitted by an object and relate it to the temperature of the object using a calibration curve that has been determined either experimentally or theoretically (from Planck's law) [9]. Typical radiation thermometers measure temperature above 600 °C, this type of instrument dominates the temperature measurement instrument market for temperature over 2000°C.

Dils [10] proposed a fiber optic version of radiation thermometer. In this sensor the end of the fiber is used as a small blackbody cavity, by shearing it at an angle and coating it with a metal, such as platinum, for use as a radiation thermometer. Since the fiber diameter can be very small (<1mm) and the sensor diameter is the same as that of the fiber, such a fiber sensor can measure temperature from 600 °C up to 2000 °C with a fast time response. Adam achieved kHz frequency response with this structure [11].

1.3.2 Thermometers based on thermal expansion

These are sensors that use the temperature dependence of the optical path length in a small optical resonator cavity, i.e a Fabry-Pérot (FP) interferometer in an optical fiber [12]. These temperature sensors measure the change in optical path length of a short piece of material whose thermal expansion coefficient and refractive index as a function of temperature are known. The temperature measurement range is dependent on the fabrication materials. Silica fiber based FP temperature sensor has been demonstrated for temperature measurement up to 800 °C, while single crystal sapphire fiber based FP temperature sensor has been demonstrated for temperature measurement up to 1500 °C [13].

1.3.3 Fluorescence thermometers

This type of sensor measures temperature by detecting the decay time or intensity of a UV stimulated visible fluorescence pulse, which is temperature dependent. In optical luminescence based fiber sensors, a UV light source is focused into an optical fiber, thus illuminating a small sample of luminescent phosphor at the end of the fiber. The decay time or intensity of the UV stimulated visible fluorescence pulse is guided along the fiber and detected to measure temperatures. Some of the most commonly used phosphors are made using a rare-earth element, such as Gadolinium or Europium, doped into a ceramic crystal, such as yttria (Y_2O_3) [14-16]. The strong temperature dependence of the luminescence allows temperature measurement with good accuracy [17]. Such sensors have found applications in the measurement of temperatures within microwave ovens, or in very high-magnetic field regions. Those sensors suffer from background noise and

require complex electrical detecting units for the weak intensity ultrashort optical pulse signals.

1.3.4 Thermometers based on optical scattering

Another class of optical thermometers employs the temperature dependence of scattered light [18]. Rayleigh scattering, resulting from scattering of light by particles smaller than the wavelength of light, depends on both the size and number of scatters present and it is these relationships that enable the effect to be used in a thermometer [19-20]. Raman scattering [21], however, results from the scattering of light off phonons, or vibrational modes of the crystal, and results in two wavelength-shifted scattered light signals. One is called “Stokes scattering”, at a longer wavelength than the incident light, resulting from phonon emission, and the other, at a shorter wavelength, resulting from phonon absorption, is called “anti-Stokes scattering”. The intensity of the anti-Stokes scattering depends strongly on the number of sufficiently energetic optical phonons in the crystal, which is a strong function of temperature. The ratio of the anti-Stokes to Stokes scattering is thus a sensitive indicator of temperature.

1.4 Industrial needs for novel high temperature sensors

The majority of commercially available temperature measurement instruments are made using only a few basic types of instruments: liquid-in-glass thermometers, thermocouples, resistance thermometers and radiation thermometers. These conventional and traditional measurement instruments have been in use for several decades. The major sources of their instability or drift, as well as possible systematic errors, are well understood. As matured technologies, they are also generally unexpensive, and there are large ranges of suppliers offering equivalent plug compatible equipment.

Although these conventional instruments are widely available for scientific and industrial applications, innovation and research and development activities in temperature measurements need to be pursued, because commonly used traditional techniques are not suitable for specific measurement problems, or the performances attainable by these traditional techniques concerning measurement sensitivity, accuracy and range are

limited. The specific measurement requirements become necessary in today's modern industrial environments, including low thermal mass sensors for fast time response, gas temperature measurement, measurement of internal temperature profiles, measurements in hostile environments, e.g., EMI (Electromagnetic interference), radiation, corrosion and intrinsic safety, where the measurement environment should not be affected by the measurement units.

One representative harsh environment is an entrained flow slagging gasifier, which is one of the main units among coal gasification facilities. In the new emerging coal-fired power plants for advanced power generation, the coal gasification technique [22] is developed to generate extremely clean electricity and other high-value energy products. Rather than burning coal directly, coal gasification reacts coal with steam using carefully controlled amounts of air or oxygen under high temperatures and pressures. A gasification-based power plant uses the hot, high-pressure coal gases exiting a gasifier to power a gas turbine. Hot exhaust from the gas turbine is then fed into a conventional steam turbine, producing a second source of power. This unique integrated gasification combined cycle (IGCC) configuration of turbines offers major improvements in power plant efficiencies compared with conventional coal combustion. To optimize performance for these IGCC plants, certain important physical parameters should be monitored and controlled precisely for coal gasification processes [23], such as real-time accurate and reliable monitoring of temperatures at various locations in a coal gasifier, pressure distribution monitoring in a gasifier, burning material flow patterns inside the gasifier control and monitoring, air or oxygen monitoring, etc.

The gasifier must be operated at a temperature high enough for the ash in the fuel, such as coal, to melt and become sufficiently fluid to flow out of the gasifier through the bottom tap-hole. Load changes will also affect the temperature in the gasifier and downstream, and would require adjusting the operating conditions. Operating at a too low temperature would cause the molten slag to become viscous or freeze, plugging up the tap-hole and preventing additional slag from draining out of the gasifier. Eventually the gasifier has to be shut down, cooled off, and the slag, now in the form of a hard vitreous rock, has to be

manually chipped out to be removed from inside the gasifier. The shut down to clean up the slag may take weeks, resulting in a lengthy loss of production. On the other hand, operating at a too high temperature would significantly shorten the lifetime of the refractory lining. In addition, more of the alkali species in the ash would be volatilized, reacting with the ash particles entrained in the gas to form low temperature eutectics which deposit in the cooler sections of the gasifier or on downstream equipment, such as the boiler, causing plugging problems. Operating the gasifier at a too high temperature will also reduce the conversion efficiency of the gasification process in the production of the synthesis gas.

In order to realize the full economic potential of the gasification systems, there is an increasing need to utilize a wide variety of feedstock in addition to coals, such as biomass, refuse, wood wastes, etc., in the gasification plants. The ash properties of these various feedstocks vary significantly, and would thus require operating the gasifier at different temperatures to facilitate slag tapping. The flow condition inside the gasifier is highly turbulent, with many pockets of gas recirculation zones. Temperature in various regions of the gasifier could be widely different. The temperature at the exit of the burners could be above 1927°C (3500F), whereas close to the wall temperature could drop to less than 1316°C (2400F). Real-time accurate and reliable monitoring of temperatures at various locations in a gasifier is thus highly desirable.

Various methods for measuring temperature in harsh environments have been investigated in the past [24-28]. Among these are optical and acoustical pyrometers, and high temperature thermocouples. However, due to the harsh environment involving entrained molten slag, high temperatures and pressures, and corrosive gases, conventional sensors and measurement devices are very difficult to apply [29-33].

In the non-contact optical pyrometers, an infrared transparent high temperature window on the gasifier wall is necessary to maintain a large pressure differential, while allowing transmission of the infrared radiation emitted by the product gases to the detector placed outside the gasifier. Obstruction of the sight-path opening for the pyrometers in the

refractory wall by molten slag is a major problem. Shifting of the refractory lining, which could have a thickness of 2 feet or more, during heat-up and operation processes could also cause blockage of the sight path. In addition, the measurement is also subject to interference from the radiation emitted by entrained particles or the relatively cold refractory walls.

Acoustic pyrometers, which deduce gas temperature along a line of sight by measuring the speed of sound along that line, have also been evaluated for use in gasifiers. Noise in the plant or gasifier, such as from the high velocity burners, soot-blowers, etc., interferes with acoustic temperature measurements.

Current high temperature thermocouples that utilize precious metals drift significantly and have a limited life of only a few days. Slag buildup around the thermocouple is also a problem, forming an insulating layer on the thermocouple.

Direct contact temperature measurement is preferred since it will give the measurement for a specific location. Several of these devices installed at the critical locations inside the gasifier could provide a temperature profile of the gasifier. Flow patterns inside the gasifier could thus be deduced from the temperature profile, and performance of the gasifier could be monitored and improved by making operating adjustments. However, no direct contact-measuring device is available to date due to material issues. The highly corrosive molten slag attacks both metals and ceramics. Ceramic materials are also susceptible to attack from alkali vapors in the gas [34-38]. This situation suggests that innovative techniques that can operate in the gasifier harsh environment for real-time, reliable monitoring of temperature be developed.

In this research program, an optical broadband polarimetric differential interferometric (BPDI) temperature sensor system was proposed and tested using single crystal sapphire material, which possesses high melting temperature (over 2000°C), superior optical transparency, and ability to resist chemical corrosion. With a simple mechanically-structured sensing probe, and optical spectrum-coded interferometric signal processing

techniques, the single crystal sapphire optical sensor can measure high temperature in harsh environments with great accuracy, corrosion resistance and long-term measurement stability.

1.5 Special requirements for temperature sensors in coal gasifier

The optical temperature sensors that can be used in the coal gasifier have to satisfy several special requirements as explained below.

1. High temperature capability

The operating temperature in the coal gasifier is in the range of 1200°C~1600°C, depending on the physical locations in the chamber. The high temperature is the main reason that renders most electronic sensors inapplicable. Some optical sensors cannot be deployed because of the limitations of the thermal properties on the fabrication materials. For example, silica optical fibers can only sustain temperatures up to 800°C before the dopants start to thermally diffuse. To measure high temperatures accurately in a wide measurement range with high resolution, proper fabrication materials are needed, as well as a simple and stable mechanical structure of the sensing probe.

2. High pressure survivability

Pressures as high as 500 psi can be encountered in the coal gasifier chamber. In order to be able to survive in such high pressure environments, the optical temperature sensing probe must be designed and fabricated with enough mechanical strength and with its optical paths entirely sealed to provide the necessary protection.

3. Good thermal stability

The optic temperature sensors designed for the harsh environmental sensing applications must be thermally stable. Temperature-related degradation mechanisms, including thermal shock, thermal cycling, thermal stress, thermal fatigue, and high heat flues, must be considered in the elevated temperature sensor design for long-term stable measurements. Solid mechanical structures and special fabrication materials are needed to increase the thermal stability.

4. Chemical corrosion resistance

With temperatures exceeding 1200°C, pressure exceeding 500 psi, and chemically corrosive agents such as alkalis, sulfur, transition metals and steam, it is hard to find a material that is impervious to such an extensive corrosive attack. Conventionally, commercially available temperature sensors exhibit greatly abbreviated lifetimes due to the harsh environment. Proper fabrication materials are needed to implement the sensing probe.

5. Absolute measurement and self-calibration capability

Optical temperature sensors with absolute readouts are much more attractive for applications in harsh environments because of their no requiring of initialization and recalibration when the power is switched on. In addition, the sensors are required to have self-calibration capability so that the guiding fiber loss variations and the source power fluctuations can be fully compensated, or absolute measurement becomes meaningless.

6. Cost-effectiveness

As the market for optical temperature sensors for harsh environment grows rapidly, the cost of the sensors and instrumentation is becoming a concern of increasing importance. In order to achieve successful commercialization, optical temperature sensor systems must be robust as well as low cost. This requires that the complexity of the sensor system is kept to the minimum and the technique and process of fabricating sensor probes have the potential of allowing mass production.

7. Deployability

Optical temperature sensors designed for harsh environment applications must be capable of remote operation and be flexible enough for easy deployment. Features of mechanical vibration-proof, high mechanical strength, and remote monitoring and control capability are thus necessary.

1.6 Scope of research

In this research, innovative techniques are presented for high temperature sensors capable of operating at temperatures up to 1600°C. These sensors fulfill the need for real-time monitoring and long-term direct measurement of high temperatures in harsh environments.

The efforts devoted to innovative sensing techniques focus mainly on the following issues.

- 1) The study of sensing schemes;
- 2) Cost-effective opto-electronic signal processor design and implementation;
- 3) Fabrication material selection and mechanical packaging structure design of the sensing probe;
- 4) Sensor prototype implementation;
- 5) Optimization of the sensor prototype and performance evaluation;
- 6) Expansion of the developed technologies to sensing applications other than temperature measurement.

The principle of sensing technology is presented in Chapter 2, including sensing schemes, optoelectronic signal processors for temperature information extraction, as well as a mathematical model for the temperature measurements. The work of implementing the sensor prototypes is reported in Chapter 3. Four different optical temperature sensor prototypes were proposed and tested. The optical broadband polarimetric differential interferometric (BPDI) temperature sensor system is chosen as an optimal approach for the high temperature measurement. Chapter 4 is dedicated to the BPDI sensor system performance analysis and performance enhancement. The experiments and results of the BPDI optical temperature sensor are presented in Chapter 5. Chapter 6 discusses the possibility of expanding the application of BPDI technology to sensing applications other than temperature measurements. Chapter 7 summarizes the research work and proposes future research directions and improvements.

Chapter 2. Principles of operation of the designed optical sensors

An optical wave is characterized by several variables such as intensity, spectrum, phase and state of polarization. Many different physical phenomena related to these characteristics are used to perform sensing functions. In the designed novel optical temperature sensors, the temperature information is encoded in the phase, state of polarization, as well as spectrum of the optical wave. This combined sensing scheme guarantees the measurement of absolute high temperature with high accuracy, high resolution, large dynamic measurement range and long-term measurement stability.

An optical measurement system is typically composed of two basic parts. One part is a sensing element, also called transducer. It is a unit to convert measurand into measurable physical signals through certain sensing schemes. The other part is a signal conditioning and processing unit, including optical detecting units, signal amplifiers, supporting electronic circuits, a signal A/D converter, a computer, computer software for signal processing calculations and control, and data presentation elements. This chapter presents the working principles of those separate elements in the optical sensors. Optical sensing elements utilizing different sensing schemes are described in Section 2.1; the signal conditioning and processing units are presented in Section 2.2; Section 2.3 describes the digital signal processing techniques for blackbody radiation background subtraction; the configurations of the potential temperature sensing systems are compared and the BPDI sensor system is selected for further prototype development in Section 2.4; the mathematical model of temperature sensor based on the BPDI technology will be given in Section 2.5. Finally the advantages of the BPDI sensor system are listed in Section 2.6.

2.1 Optical sensing elements design

Because of its high resolution and accuracy, optical interferometry methods are widely employed to build optical sensors by encoding measurand information in the phase of the optical wave through the interference phenomena. There are several different types of interferometric techniques which have been widely used to measure temperature and other physical parameters. These are Mach-Zehnder[39], Michelson, Fabry-Perot, and Sagnac interferometers. Optical fiber Fabry-Perot sensors are highly sensitive to temperature, mechanical vibration, magnetic fields, and acoustic waves [40-41]. Many techniques have been used to create intrinsic or extrinsic Fabry-Perot cavities, such as Bragg gratings in or on the fiber, metal coatings on the end faces of the fiber, and the use of air-glass interfaces at the fiber ends as the reflectors. Although intrinsic Fabry-Perot sensors have been used in the past to measure several physical parameters including temperature, extrinsic Fabry-Perot interferometers (EFPI) have shown their ability to be insensitive to polarization and only sensitive to axial strain components, which gives them an advantage over other electro-mechanical and intrinsic Fabry-Perot sensors.

2.1.1 Review of EFPI sapphire fiber sensor

Silica fiber based EFPI sensors have shown great promise for measuring temperatures (and other physical parameters) below 800°C and have been designed and tested extensively in the Center for Photonics Technology (CPT). At higher temperatures the devices degrade rapidly. The degradation mechanisms fall into two general categories: one is the crystallization of the silica cladding region which degrades the fiber performance, the other is the diffusion of the germanium dopant (used to establish the refractive index gradient between the core and the cladding) from the core region into the cladding, which changes the waveguiding properties of the fiber. By replacing silica fiber with sapphire optical fibers, the sensors can potentially operate at high temperature (up to 1500°C) environments [13].

As shown in Figure 2.1, a sapphire air gapped EFPI sensor head is formed by inserting the lead-in single crystal sapphire fiber into the one end of the sapphire tube and inserting

another short piece of sapphire fiber into the other end of the tube to act as a reflecting surface (target fiber). Both the lead-in and the target sapphire fiber ends are polished to optical quality. While one end of the target sapphire fiber is highly polished, the other end is shattered to prevent any significant reflection that would interfere with the measurements. The light propagating in the lead-in sapphire fiber is partly reflected (7%) at the first sapphire-air boundary. The transmitted light travels through the air gap and is also partially reflected (7%) at the end face of the target sapphire fiber. Reflectance R of the well polished sapphire fiber end surface is approximately 7% as given by the following equation:

$$R = \left[\frac{(n - n')}{(n + n')} \right]^2 \tag{2.1}$$

for wavelength $\lambda=580\text{nm}$, $n=1.768$ is the refractive index of the sapphire fiber, and $n'=1$ is the refractive of the air.

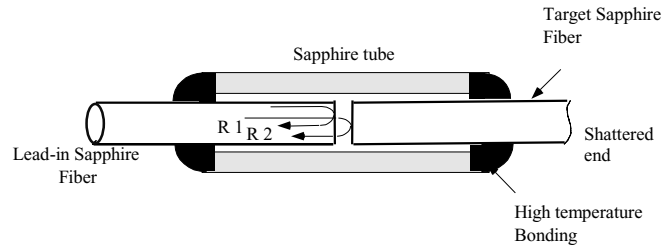


Figure 2.1. Schematic design of the sapphire fiber based EFPI sensor

Commercially available sapphire fiber is actually a thin sapphire rod using air as a cladding, which makes the sapphire fiber have a very large modal volume. With these highly multimode fibers, interference signals are generated with poor visibilities in the FP cavity formed by the ends of the two sapphire fibers. As shown in Figure 2.2, the interference between beams from the same mode order (beam 1 and beam 2) are desired to deduce the cavity length information, while interference between beams from inter-modes (beam 1 and beam 3, or beam 2 and beam 3) will degrade the interference signals, resulting in low interference fringe visibilities. When the low quality interference signals propagate in the multimode fiber, the inter-modal dispersion in the sapphire fiber degrades the interference fringes further, thus it is very difficult to fabricate high quality

sapphire EFPI sensing elements for temperature sensing. In industrial environments where mechanical vibration exists, all of the possible modes in the sapphire fiber can be excited and get involved in the interfering process, the more modes in the sensing head, the lower quality the interference signals.

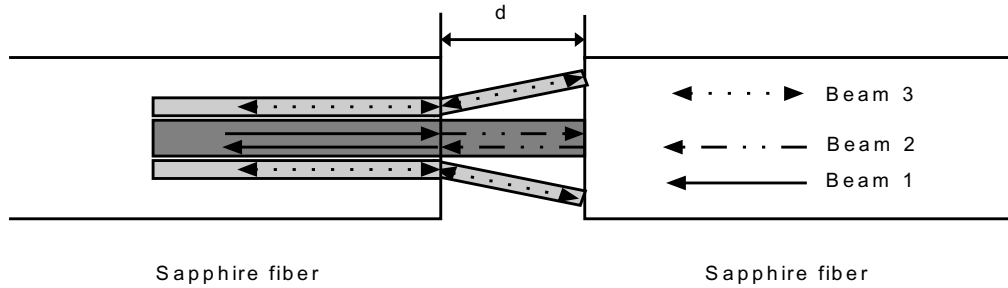


Figure 2.2. Interference in the FP cavity formed by multimode sapphire fibers

The EFPI sensing element was fabricated by Xiao *et al* with two 100 μ m diameter sapphire fibers [13], one single mode silica fiber guides light into the sensing head, and the sensing F_P cavity is kept on an isolated optical table to avoid exciting higher order modes in the sapphire fiber. Figure 2.3 shows the output interference spectrum of the sapphire EFPI sensor with a F_P cavity length of 6.5 μ m. Figure 2.4 shows the output spectrum with a cavity length of 21.8 μ m. As seen in these two figures, when the cavity length increases, the visibility of the interference signals degrades significantly. Those low quality interfering signals can not provide accurate and reliable high temperature measurement in harsh environments.

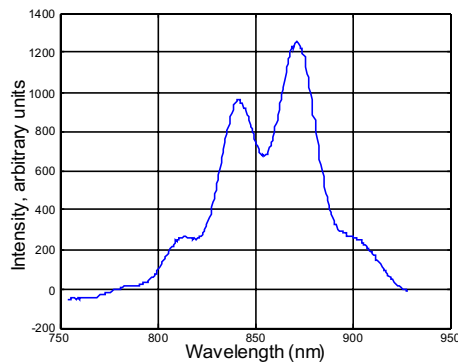


Figure 2.3. Output spectrum from the EFPI sapphire fiber sensor with cavity length=6.5 μ m

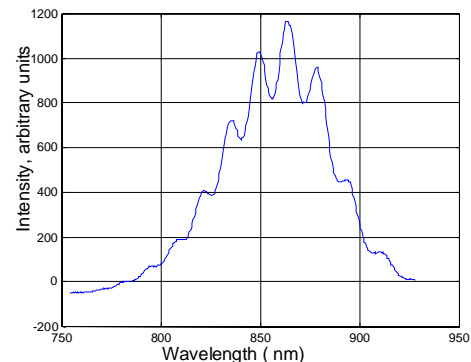


Figure 2.4. Output spectrum from the EFPI sapphire fiber sensor with cavity length=21.8 μ m

2.1.2 Broadband polarimetric sapphire sensor

Polarization is a fundamental property of light that can be used to measure physical parameters in a sensing system. The determination of the state of polarization (SOP) in a system can provide information about photochemical, photo-biological or physical processes. Techniques employing polarized light are already widely adopted in the spectroscopic techniques to provide different types of information about atoms or molecules, such as the electronic structure of the molecules, or orientation of the molecules [42-43].

An interference system utilizing polarized optical waves generally includes a polarizing device that is located between an optical polarizer which sets the state of polarization at the entrance and a polarization analyzer which makes the interfering states of polarization identical. Figure 2.5 makes the general principle of the system clear. The polarizing devices such as phase-shifters or retardators split the incident light wave into two orthogonal linearly polarized waves. Since these two waves propagate at different velocities in the polarizing device, their phases are shifted by a quantity Φ . After analyzed by a polarization analyzer, the emerging optical intensity is a function of the phase shift Φ , which can be used for temperature measurement.

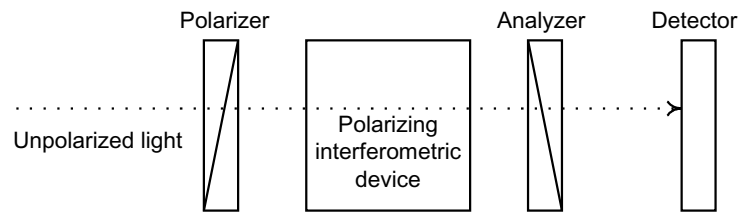


Figure 2.5. Principle of operation of an interference device using polarized light waves

Due to the crystallographic arrangement of the atoms in the single crystal sapphire, the material exhibits an inherent birefringence. For a wavelength $\lambda=589\text{nm}$, $n_o=1.768$, and $n_e=1.760$, so the birefringence is 0.008. The single crystal sapphire disk can thus be used as a sensing element in the polarimeter. Figure 2.6. illustrates the working principle of the sapphire sensing head [44]. One single crystal sapphire disk with inherent birefringence is sandwiched between a polarizer and an analyzer. The polarization directions of the

polarizer and the analyzer are parallel to each other and along the z-axis. The principal axes (f-axis and s-axis) of the sapphire disk are oriented at 45° with respect to the z-axis. At the exit of the disk, the phases of the two orthogonal states are shifted by a quantity Φ and the emergent state of polarization is usually elliptical. In order to recover the phase shift Φ introduced by the disk, the emerging light has to be analyzed through a polarization analyzer. The phase shift is determined by the magnitude of the birefringence and also by the length of the sapphire disk traveled by the two orthogonal linearly polarized light beams. Since both the birefringence and thickness of the sapphire-sensing element are functions of the temperature, the magnitude of the differential phase shift will also be temperature dependent. Therefore, by sensing the magnitude of the phase shift, the temperature can be determined.

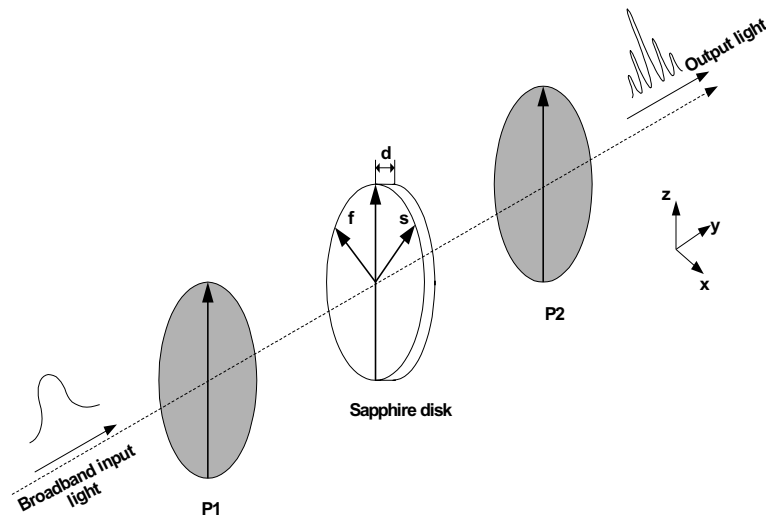


Figure. 2.6. Conceptual schematic design of the sensing head: broadband polarimetric differential interferometry (BPDI)

The phase shift between the two orthogonal linearly polarized light waves is determined by the optical path difference (OPD) between those two linearly polarized light beams, given by:

$$\begin{aligned} \Phi &= 2\pi \times OPD / \lambda \\ OPD &= |n_e - n_o|d \end{aligned} \tag{2.2}$$

where d is the thickness of the sensing element, n_e and n_o represent the two refractive indices corresponding to the two orthogonal linearly polarized light waves, and λ is the

light wavelength. Theoretically speaking, n_e and n_o are wavelength dependent, but their differences are very small in the interested wavelength range from 800nm-900nm. They are approximated as constant in this wavelength range, thus the OPDs for all the wavelength are assumed to be equal. The same OPD will generate different phase shifts at different wavelengths, thus light will experience constructive (corresponding to the phase shift of $2m\pi$, m being an integer) or deconstructive (corresponding to the phase shift of $(2m+1)\pi$, m being an integer) interferences depending on their wavelengths. Utilizing the constructive and deconstructive interference fringes in the broadband spectral domain, shown in Figure 2.7, the temperature dependent OPD can be obtained by calculations, and thus temperature information can be obtained by calibration.

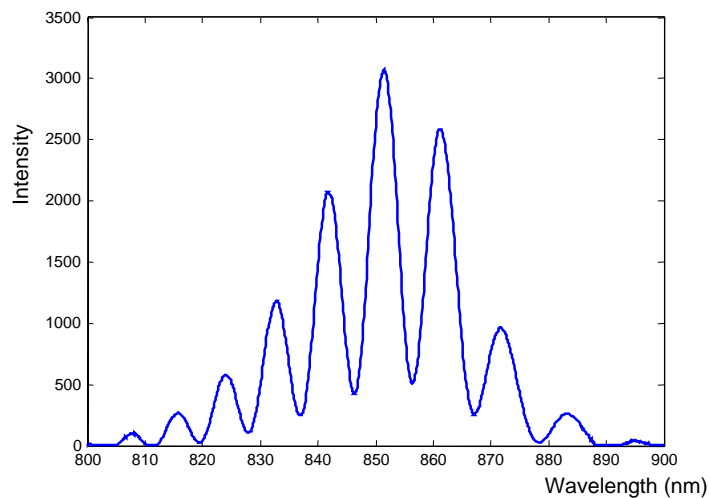


Figure. 2.7. Measured output optical interference signal $I(\lambda)$ from the BPDI sensor

By encoding and decoding temperature information in the phase of an optical signal, this sensor design guarantees self-calibration capability, where the encoded temperature is not corrupted by optical intensity fluctuations from long term operation point of view, hence better measurement repeatability than intensity based optical sensors.

2.2 Signal processing units

2.2.1 Review of signal processing methods for interferometric sensors

As one of the most sensitive measurement methods, optical interferometry has been used in a variety of applications. In coherent mono-wavelength interferometric systems, the most commonly used signal demodulation method is direct interference fringe counting, i.e. using a power meter to detect the intensity of the interference signal generated by the sensor head and an electric counter to count the total number of peaks from a reference point. However, due to the nonlinear and periodic nature of the sinusoidal interference fringes, the fringe counting method suffers from a number of problems such as sensitivity reduction when the sensor reaches the peaks or valleys of the fringes, and fringe direction ambiguity, which practically limited the accuracy of measurement. It was possible to count fringes bi-directionally by using a quadrature-phase-shifted two-interferometer structure [45]. However, it was also found difficult to maintain the exact phase difference between these two interferometers in practical applications.

More recently, Jackson [46], Hogg [47], Steward [48], and Gangopadhyay [49] reported the use of laser wavelength modulation based heterodyne interferometry to demodulate the interference signal of EFPI sensors. However, due to the short initial cavity length of the EFPI sensors, the resolution of the wavelength modulation based signal processing method was limited.

For the polarization interferometry sensor, intensity based polarization quadrature measurement can be carried out to detect the phase delay between the two orthogonally polarized light waves. This method has limited measurement range and suffers from the complex structure of the detection unit. It thus highly depends on the performance of those separate components in the detection unit.

In the CPT, there are two signal processors developed to meet the efficient signal processing needs for interferometric sensors, including polarimetric sensors. They are self-calibrated interferometric/intensity-based (SCIIB) signal processor, and spectral domain white light interferometry (also called low-coherence interferometry) signal

processor. The signal processing units can reliably measure the optical path difference (OPD) that exists between the two interfering optical waves in an interferometer, with high resolution and high accuracy, as well as self-compensation capability for the optical source power drifting and fiber loss variations, which can result in a large measurement error when the signal processing methods based on intensity detection are directly applied.

2.2.2 SCIIB signal processor

As a unique signal processing method, the self-calibrated interferometric/intensity-based (SCIIB) [50] fiber optic sensor successfully combines the advantages of both the interferometric and the intensity-based fiber sensors in a single system. Through a proper design of the sensor head, the SCIIB technology can provide absolute measurement of various parameters with the full self-compensation capability for the source power fluctuation and the fiber loss variations.

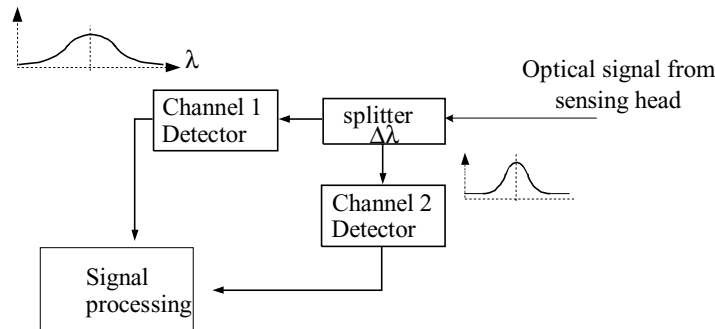


Figure 2.8. Illustration of the principle of operation of the SCIIB fiber optic signal processor

As shown in Figure 2.8, the optical signal from the sensing head is split into two channels with different optical properties through optical filtering. The light in Channel 1 remains its original spectral width (broadband spectrum) while the light in Channel 2 has a narrower spectrum by passing it through an optical bandpass filter. By taking the ratio of these two channels outputs, the optical source intensity fluctuation and transmission fiber loss can be fully compensated.

As mentioned previously, regular interferometric sensors suffer from the disadvantages of sensitivity reduction and the fringe direction ambiguity when the sensor output reaches the peak or valley of an interference fringe. Sensitivity is reduced at the peak or valley of the fringe since at that point the change in optical intensity is zero for a small change in the sensor cavity length. Fringe direction ambiguity refers to the difficulty in determining from the optical intensity whether the sensor OPD is increasing or decreasing. To avoid these two problems, the sensor head has to be operated only over the semi-linear range of a half fringe, as shown in Figure 2.9, so that a one-to-one quantitative relation between the output intensity and the OPD in the sensor head is obtained. Because of this limitation associated with the SCIIB signal processor, spectral domain white light interferometric signal processor is adopted for the high temperature measurement application.

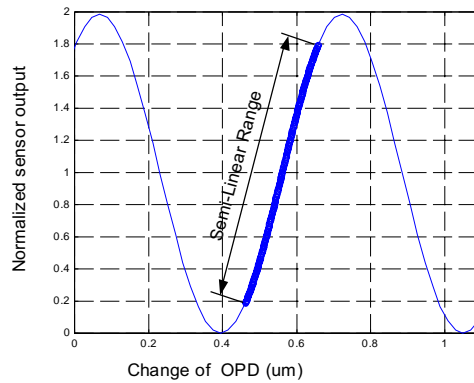


Figure 2.9. Illustration of a semi-linear operating range of the interference fringes.

2.2.3 Spectral domain white light interferometric signal processor

As shown in Figure 2.10, a white light or low coherence interferometric technique uses a broadband light source, such as light emitting diodes (LED), multimode laser diodes or halogen lamps. Its operation principle was first adopted for single mode fiber sensing systems [51] and then in multimode fiber sensing systems [52]. The white light interferometric fiber optic sensor system inherits most of the advantages of the conventional optical interferometers, such as immunity to the light source power drift and variations of fiber transmission losses, and high resolution.

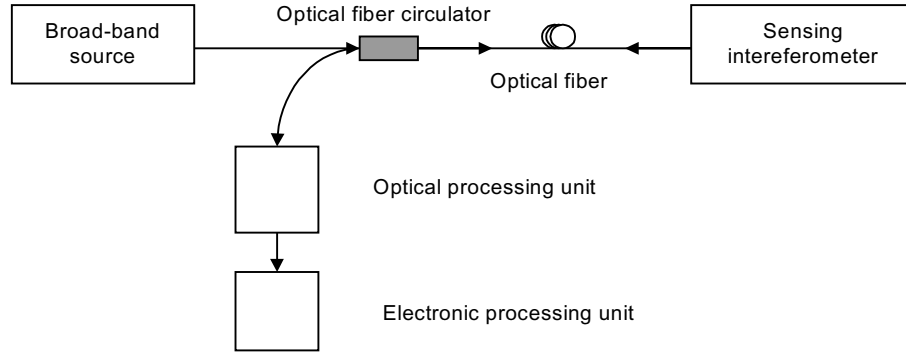


Figure 2.10. Basic structure of optical fiber sensor based on white light interferometry

In the spectral domain white light interferometric signal processor, the optical path difference (OPD) between the two interfering light waves is obtained through interferometric fringe pattern analysis. For low frequency signal detection (typically less than 100 Hz), the spectrum measurement method can provide absolute OPD measurements with high resolution and large dynamic range. Since variations of temperature in the coal gasifier environments are in the low frequency range, a compact white light signal processor based on the spectrum measurement has been adopted in this research.

In the spectrum measurement based white light interferometric system, an optical spectrum analyzer (OSA) is used as the optical signal processing unit. The OSA is composed of a grating and a CCD array. The intensities of the dispersed spectral components of the optical signal are scanned electronically by the CCD array in the OSA. The optical signal is thus converted into an electrical signal and processed in the electronic processing unit.

If we assume that the broadband light source (light emitting diode, LED) in Figure 2.10 has a Gaussian spectral intensity distribution given by

$$I_s(\lambda) = I_0 \exp\left[\frac{-(\lambda - \lambda_0)^2}{(\Delta\lambda)^2}\right] \quad (2.3)$$

where λ_0 is the central wavelength, I_0 is the peak intensity value, and $\Delta\lambda$ is the source spectral width. The two-beam interference signal is then given by:

$$I = I_s(\lambda) \left[1 + \gamma \cos\left(\frac{2\pi L}{\lambda}\right) \right] \quad (2.4)$$

where the factor γ is the visibility of the interference fringes, and L represents the optical path difference (OPD) between the two interference beams. The ideal value of γ will be $\gamma=1$, and it may decrease because of the coherence length of the optical source and the amplitude difference between the two interference optical waves.

After normalizing the interference spectrum given by Equation (2.4) with respect to the source spectrum $I_s(\lambda)$, we have the normalized interference output expressed as

$$I_n = 1 + \gamma \cos\left(\frac{2\pi L}{\lambda}\right) \quad (2.5)$$

It is shown in Equation (2.5) that the output spectrum of the sensor is modulated by a cosinusoidal function due to the interference. As shown in Figure 2.11, interference fringe patterns are different for different OPD values.

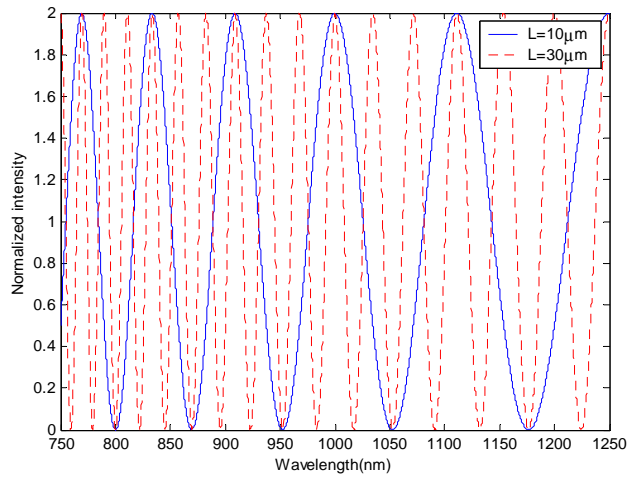


Figure 2.11. Normalized optical interference fringes for different OPD values (with $\gamma=1$).

Because the interference fringe patterns are a function of the optical path difference L , the successful demodulation of this spectral signal can render an accurate and absolute measurement of the L values, which may be related to the physical parameters, such as temperature, pressure, and stain. The L measurement can also be related to biological or

chemical parameters as well. It is these relations that make the spectral domain white light interferometry a powerful tool in the field of optical sensing technologies.

2.3 Blackbody radiation subtraction

As well known, for a cavity with perfectly absorbing (i.e. black) walls at a fixed temperature T , its interior will be filled with radiant energy of all wavelengths. This radiation is called blackbody radiation. The intensity of the blackbody radiation becomes stronger with increasing of the temperature. Since the designed temperature measurement system will be applied to a temperature environment as high as 1600°C , blackbody radiation will be a strong noise background built upon the optical signal emitted from the LED, which is the temperature information carrier.

Based on the Planck's blackbody radiation theory, the radiation intensity is specified by a distribution function K_{λ} , representing radiation emitted into a hemisphere, its unit is $\text{W}/\text{cm}^2\mu\text{m}^{-1}$, such that the total radiation intensity is given by $\int_0^{\infty} K_{\lambda} d\lambda$ and $K_{\lambda} d\lambda$ is the intensity due to radiation with wavelength between λ and $\lambda + d\lambda$. K_{λ} is a universal function, depending only on the temperature and the wavelength, not on the size or shape of the cavity or on the material of its wall.

$$K_{\lambda} = \frac{C_1 \lambda^{-5}}{e^{\frac{C_2}{\lambda T}} - 1} \quad (2.6)$$

where $C_1=3.7405 \times 10^8$, and $C_2=1.4388 \times 10^4$, T is temperature in Kelvin [9]. High temperature sensing systems employ this formula to detect temperature values are called radiation pyrometers. Figure 2.12 shows the blackbody radiation theoretical intensity distribution curves at different temperatures.

As shown in Figure 2.13, blackbody radiation background is superimposed to the optical signals, which are temperature signatures generated by the light from the broadband optical source, and detected by the spectrometer in the optical temperature measurement system. These experimental measurement results show clearly that the blackbody

radiation background increases dramatically with the temperature increase, thus the signal-to-noise ratio (SNR) of the measured spectrum is becoming smaller.

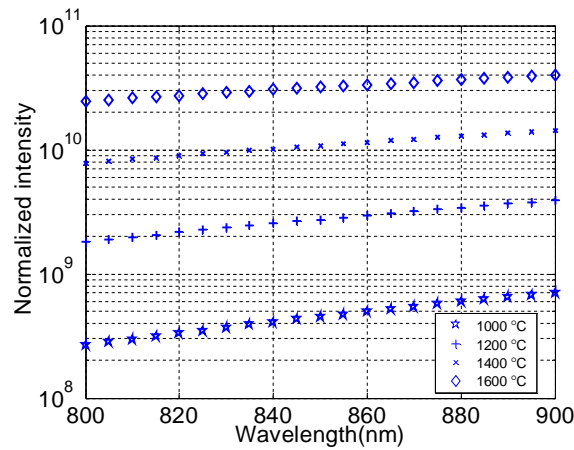


Figure 2.12. Theoretical intensity curves of the blackbody radiation above 1000°C for the wavelength range: 800-900nm.

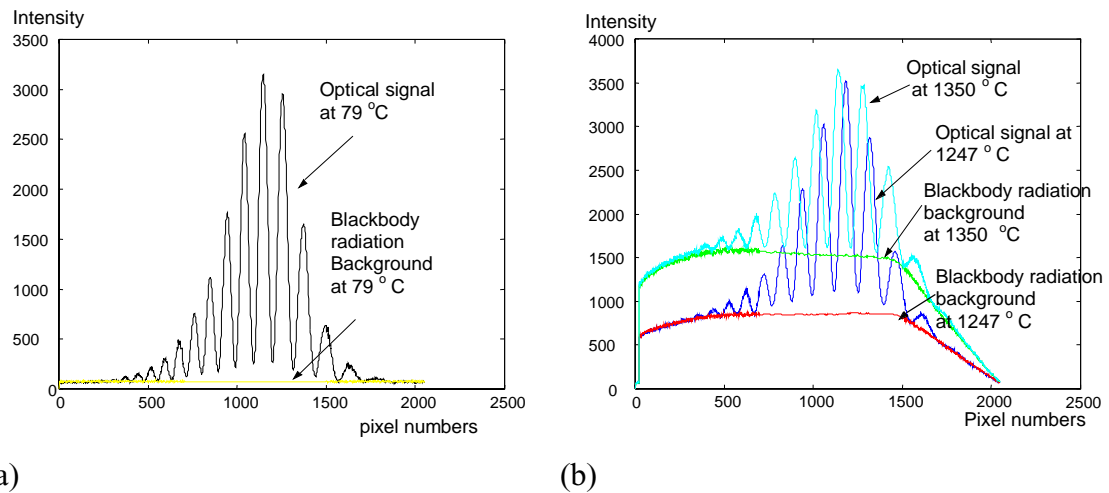


Figure 2.13, Relation between blackbody radiation and interference fringes at different temperatures.

To increase the signal-to-noise ratio in the detected optical temperature signatures, the LED output light is modulated with a certain frequency and converted into AC signals, while the blackbody radiation can be treated as DC signals. Thus the DC background can be subtracted with digital signal processing techniques in the computer. One method to reduce the blackbody radiation is to utilize a band pass digital signal filter [53] (IIR filter, Infinite-Impulse Response filter) filtering out the desired AC optical signal from the LED

only. The background from blackbody radiation will be blocked as a DC component in the detected signals. If the frequency used for the LED modulation is 3 Hz, the designed filter is shown in Figure 2.14, whose pass band covers 2Hz to 5Hz. Using the digital signal filter, the blackbody radiation background is reduced, as shown in Figure 2.15.

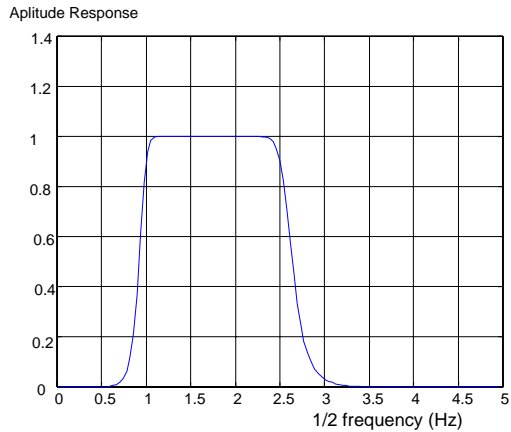


Figure 2.14. Amplitude response of a IIR filter

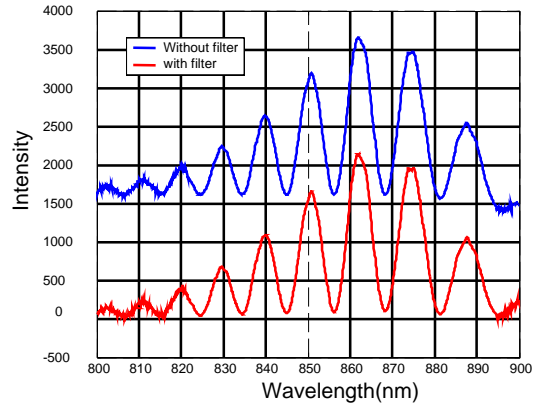


Figure 2.15. Interference curve with blackbody radiation (at 1350 °C) subtraction

2.4 Configurations of designed temperature sensor systems

By employing the previously described optical sensing elements (EFPI sapphire fiber sensor, and polarimetric sapphire sensor) and signal processors (SCIIB signal processor

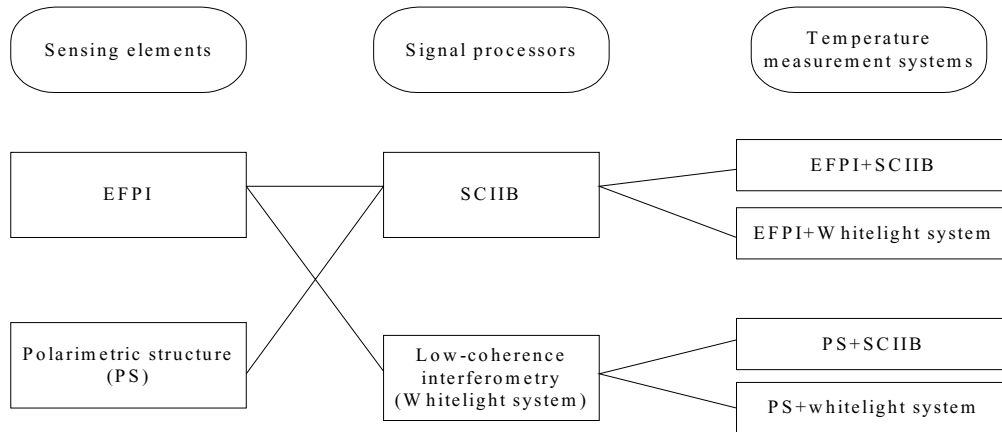


Figure 2.16. Temperature measurement systems based on designed sensing elements and detecting units

and spectral domain white light interferometric signal processor), four temperature measurement systems rooted in the optical interference metrology can be constructed as shown in Figure 2.16.

As discussed in the optical sensing unit section, sapphire fiber based extrinsic Fabry-Pérot interferometric (EFPI) sensing elements are difficult to fabricate and their interfering signals are usually low quality because of the sapphire fiber's multimode nature. This type of optical sensor system has been tried in CPT and proved to be not practical for temperature measurement up to 1600°C. The efforts toward this work is then focused on the development of a polarimetric structure based sensing systems, which only utilize bulk optics made of single crystal sapphire materials. Two systems: PS+SCIIB and PS+white light signal processor are attractive candidates for further development and evaluation.

The PS+SCIIB system is an optical intensity-measurement based polarimetric sapphire sensor. Because of the periodic nature of the interferometric signal, the working point and the working range of the sensor need to be selected properly for the wide dynamic range high temperature measurement. Because the SCIIB signal processor can only operate properly in a limited linear working range of the sinusoidal interferometric signals, the thickness of the sapphire sensing element is one of the keys to control the initial working point and working range of the measurement system. Birefringence of the sapphire material, which is a function of temperature, is another factor to be considered for the sensing element design. The measurement stability is also a concern related to the two-channel structure in the SCIIB signal processor. The long-term stability at different temperature environments of each of those two channels is hardly achievable. Although this system can work through careful sensing element selection and signal processor design, it is hard to maintain long-term accurate temperature measurements.

The PS+whitelight light signal processor, also named as a broadband polarimetric differential interferometric (BPDI) sensor system, on the other hand, can solve the problems associated with the PS+SCIIB system. It is chosen as an optimal approach for

further prototype instrumentation development for high temperature measurement in harsh environments. Based on its interferometric sensing scheme, high resolution and accurate temperature measurement in a very large dynamic range is achievable in this system. The BPDI sensing system monitors temperature in real-time through measuring optical spectrum instead of optical intensities. This assures its relative immunity to optical source power fluctuations and transmission fiber losses, thus providing a high degree of long-term temperature measurement stability.

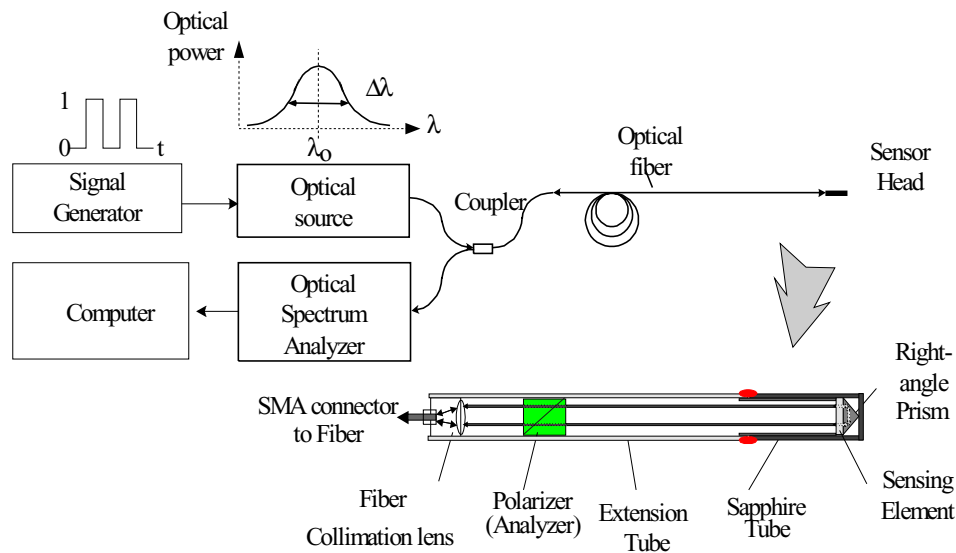


Figure. 2.17. Schematic design of the single crystal sapphire based BPDI optical high temperature sensor.

In many industrial applications, it is not practical to use a transmission version of the polarimetric sensing structure in the sensing probe, because of its two-end structure. A reflection version polarimetric sensing structure setup, which is an one-end structure is thus designed, as shown in Figure 2.17, where only one fiber collimator is used to collimate input light and also re-collect light reflected back from the other end of the sensing probe. The only optical polarizer is used both as a polarizer for the input light and a polarization analyzer for the reflected light in the sensor probe, which not only reduces the cost, but also simplifies the probe mechanical structure. The total sensing probe is then integrated into one solid long tube, which makes it robust enough to survive the harsh environments.

In the sensing system, the broadband light from a high power light emitting diode (LED) is modulated by the signal generator and converted into AC signals for the purpose of the blackbody radiation background subtraction, then injected into a lead-in multimode optical fiber and propagates through a fiber bundle to the sensor head. The light is first collimated by a collimation lens, then converted into a linearly polarized optical beam and travels across a free space enclosed by a high temperature ceramic tube and a single crystal sapphire tube to a single crystal sapphire sensing element. The light is then reflected by a right angle zirconia prism and passes through the sapphire-sensing element again. When the light exits the polarimeter, the two linear polarized light components with a differential phase delay are combined along the polarizer direction to interfere with each other. The output light from the polarimeter is then re-collected by the same input optical fiber bundle and travels back along the optical fiber to the optical detection end, which is a fiber optic PC plug-in spectrometer, composed of a grating and a CCD array. The intensities of the dispersed spectral components of the signal are scanned electronically by the CCD array with a high spectrum measurement resolution. Additional signal processing is performed in the computer to extract the temperature information.

2.5 Mathematical model for BPDI temperature sensor

One way to describe the sensing principle of the optical sensor mathematically is using the Jones matrix method. This method was invented in 1940 by R.C.Jones [55], and is a powerful tool for analyzing the properties of transmitted light through a complex optical system composed of many optical elements. In the Jones matrix method, the state of polarization is represented by a two-component vector. Each optical element can be represented by a 2*2 matrix. The overall transfer matrix for the whole optical system is obtained by multiplying all of the individual element matrices, and the polarization state of the transmitted light is computed by multiplying the vector representing the input beam by the overall matrix. This method deals with mathematical formulas and is very effective for a system with large numbers of optical elements. In this temperature sensor system with a few optical elements, a more simple method is employed with emphasis on the physical activities in the sensing probe.

The optical interfering activity inside the polarimeter is shown in Figure 2.18, where polarization directions of the polarizer and the analyzer are parallel to each other. The input broadband light is polarized by a polarizer P1. The oscillation direction of the electric field vector of the light wave is thus along P1 (z-axis). When this linear polarized light propagates inside a sensing element with optical birefringence, the sensing element behaves as if it split the incident polarization state into two orthogonal linearly polarized states with the same amplitudes, oriented along the principal axes of the sensing element: ordinary ray (along f-axis) and extraordinary ray (along s-axis), resulting from the 45° angle alignment between P1 and the principle axes of the sensing element. Assuming no attenuation in the sensing element, these two rays will propagate independently without changes in their amplitudes, while there will be relative phase delays between them. At the end of the analyzer, only light polarized along the z-axis can pass, where the light is decomposed according to their polarization direction again: the ordinary ray is decomposed into ray1 and ray2, the extraordinary ray is decomposed into ray1' and ray2'. Interfering results between ray2 and ray2' will pass the polarization analyzer, since the polarization directions of the polarizer and the analyzer are parallel to each other.

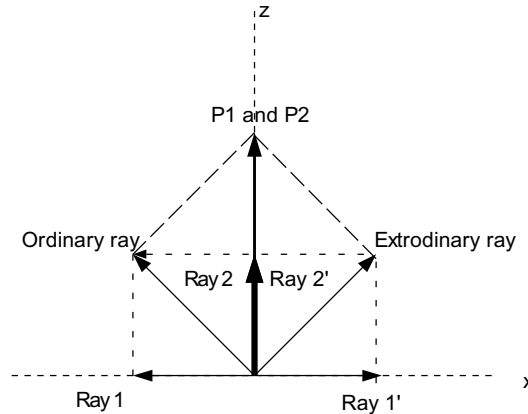


Figure. 2.18. Interfering mechanism for polarimetric differential interferometer

The interfering results can be expressed mathematically as following:

$$\vec{E}_{out} = \frac{1}{2}(\vec{E}_{ray2} + \vec{E}_{ray2'}) \tag{2.7}$$

where \vec{E}_{out} , \vec{E}_{ray2} and $\vec{E}_{ray2'}$ are all vectors. The output optical intensity is then:

$$I = |\vec{E}_{out}|^2 \quad (2.8)$$

It will not only depend on the magnitudes of the interfering electric fields, but also on the phase shift Φ between the two electrical oscillation vectors:

$$\begin{aligned} I_{out} &= \left(\frac{1}{2} E_{ray2}\right)^2 + \left(\frac{1}{2} E_{ray2}\right)^2 + \frac{1}{2} E_{ray2} E_{ray2} \cos \Phi \\ &= \frac{1}{4} E_{ray2}^2 (2 + 2 \cos(\Phi)) \\ &= \frac{1}{2} E_{ray2}^2 (1 + \cos(\Phi)) \\ &= E_{ray2}^2 \cos^2(\Phi / 2) \end{aligned} \quad (2.9)$$

where $\Phi = 2\pi d \Delta n / \lambda$. Since both d and Δn are functions of ambient temperatures, I_{out} will be a temperature encoded signal. To decode the temperature information, a signal processing model in the spectral domain for the white light interferometry is needed.

The interference fringes of a broadband light from the polarimeter form a co-sinusoidal curve after it is normalized with respect to $E_{ray2}^2(\lambda)$ according to Equation (2.9):

$$I_n(\lambda) = \cos^2\left(\frac{\pi d \Delta n}{\lambda}\right) \quad (2.10)$$

where the product of d and Δn is a function of temperature, physically representing the optical path difference (OPD) between the two orthogonal linearly polarized light waves.

$$f(T) = d(T) \times \Delta n(T) \quad (2.11)$$

where,

$$\begin{aligned} d(T) &= \alpha_{//c-axis}(T) \times (T - T_0) \\ \Delta n(T) &= n_o(T) - n_e(T) \end{aligned} \quad (2.12)$$

where $\alpha_{//c-axis}$ is the coefficient of thermal expansion along the C-axis of single crystal sapphire. According to reference [54], for the temperature range 325-950K:

$$\alpha_{//c-axis}(T) = 0.6582 \times 10^{-5} + 0.4995 \times 10^{-8} \times (T - 273) + 0.2578 \times 10^{-11} \times (T - 273)^2, (T's \text{ unit in } K)$$

and the refractive indices (n_o and n_e) also depend on the temperature, they are changed along with temperature in the level of $10^{-6}[K^{-1}]$.

From the detected optical spectrum, an internally developed algorithm [66] is employed to measure the OPD $f(T)$ values between the two orthogonal linearly polarized light beams in the sensing element, which is uniquely related to the differential phase delay between the two orthogonal linearly polarized light beams. The algorithm used to calculate $f(T)$ from the transmitted interferometric spectrum is described below.

According to Equation (2.10), the normalized interferometric spectrum consists of a series of maxima or minima, shown as peaks and valleys in the spectrum at certain wavelengths. These special points have a fixed phase relation. For example, the phase difference between the two adjacent peaks (or valleys) is 2π . Therefore, by detecting the spectral locations of the peaks or valleys in the interference spectrum, we can obtain OPD values by applying Equation (2.10). Assuming the wavelengths of two consecutive peak points are λ_1 and λ_2 ($\lambda_1 > \lambda_2$) in the interference spectrum, their interference orders will be different by 1 and represented by m and $m+1$. For λ_1 and λ_2 :

$$\begin{aligned} \frac{2\pi f(T)}{\lambda_1} &= m 2\pi \\ \frac{2\pi f(T)}{\lambda_2} &= (m+1) 2\pi \end{aligned} \quad (2.13)$$

With these two equations, the interference order number m for the peak related to the wavelength λ_1 can be determined, as well as the OPD values related to the interference signals:

$$\begin{aligned} m &= \frac{\lambda_2}{\lambda_1 - \lambda_2} \\ f(T) &= d(t)\Delta n(T) = \frac{\lambda_1 \lambda_2}{\lambda_1 - \lambda_2} \end{aligned} \quad (2.14)$$

By employing the white light interferometry method to measure the OPD values in the sensing element, and relating them to the temperature by calibration, this sensor system takes into account two factors at the same time: one is the dimensional changes of the sensing element and the other is the refractive indices changes with the temperature. These two factors completely characterize the sensing element behaviors at different temperature levels. Thus this design provides a method for reliable absolute measurement of temperature.

2.6 Major advantages of BPDI sensor system

In addition to the general advantages associated with optical sensors, such as lightweight, remote operation, immunity to EMI, electrically non-conducting, and chemical inertness, the BPDI sensor system incorporates a spectrometer with a polarimeter for the purpose of measuring polarization properties as a function of wavelength, offering the following major advantages over the other sensors designed for high temperature applications:

1. Absolute measurement in a wide dynamic temperature range.

BPDI technology extracts absolute temperature information by absolute measurement of the phase delays, which are more attractive in applications for the harsh environments because of its no requirement of initialization and/or calibration when power is switched on. The one-to-one relation between the phase delays and the temperatures makes it possible to measure temperature in a wide dynamic range without ambiguity, which is usually associated with the periodic nature of the interference signals.

2. Minimized complexity in signal processor.

The BPDI sensor system uses a compact PC-plug in optical spectrum analyzer as an optical signal processor, and a digital computer for signal decoding to extract the temperature information. The complexity of the signal processor is then kept to its minimum level; the stability of temperature measurements is thus increased.

3. Self-compensation capability.

The BPDI sensor system monitors temperatures in real-time through measuring optical spectrum instead of optical intensity. This guarantees its relative immunity to optical source power fluctuations and transmission fiber losses, thus providing a high degree of long-term measurement stability.

4. Deployment flexibility.

The BPDI optical temperature measurement system takes advantages of both optical fibers and bulk optics to simplify the design of the sensing head. Bulk optics is convenient for reducing the required tolerances on optical alignment and also for reducing the sensitivity to mechanical vibrations. The optical fiber can transmit light over a long distance with small attenuation and are easily implemented in industrial environments because of their small size, lightweight and immunity to electromagnetic interference (EMI).

5. Ultra-high sensitivity.

The BPDI sensor system offers high measurement resolution since the essence of the sensing scheme is based on interferometry.

Chapter 3. Design and implementation of temperature sensor systems

This chapter will describe the design and implementation of the temperature sensor systems. As presented in Figure 2.16, four types of temperature measurement systems rooted in the optical interference metrology can be constructed: EFPI+SCIIB, EFPI+white light interferometric system, PS+SCIIB, and PS+white light interferometric system. Based on the comparative evaluation and analysis of the experimental results on these four different temperature sensing schemes, the PS+white light interferometric system, also named as broadband polarimetric differential interferometric (BPDI) system, is chosen for further prototype instrumentation development.

The implementation of the BPDI sensor system includes both hardware and software design and implementation. Hardware implementation includes fabrication materials selection for the sensing probe, sensing element structure design and fabrication, sensing probe mechanical assembly, and signal processor implementation. Software design and implementation includes algorithm development and implementation for temperature measurements based on the white light interferometry, and digital signal processing for the blackbody radiation background subtraction in the computer. In this chapter, Section 3.1 introduces the properties of the materials for the sensing probe fabrication. Section 3.2 presents the sensing probe prototypes based on the different sensing element structures. Section 3.3 concentrates on the signal processor implementation, algorithm and digital signal processing software development issues. Finally Section 3.4 provides an overview of the implemented BPDI sensor system.

3.1 Fabrication materials for sensing probes

Commercially available conventionally temperature sensors exhibit greatly abbreviated lifetimes in harsh environments, where high temperature, high pressure, chemical corrosion, strong electromagnetic interference, and high energy radiation exposure exist simultaneously. In the primary and secondary stages of a two stage slagging

gasifier, the temperature measurement devices are subjected to such extremely harsh conditions. With temperatures exceeding 1400°C, pressure exceeding 400 psig, and chemical corrosive agents such as alkalis, sulfur, transition metals and steam, it is hard to find a temperature sensor that is impervious to such an extensive corrosive attack.

Very limited materials are available to fabricate an optical sensor to be physically present in such harsh environments for direct temperature measurement. For example, no polymer materials can survive temperatures up to 1600 °C; only a few expensive metals, such as platinum and tungsten, have higher melting points over 1600 °C, but they can hardly resist the chemical oxidization, sulfidation, carbonization, and nitridation agents. Some special alumina ceramics can survive both high temperature and oxidization environments, but not all of them are optically transparent. Bearing in mind the requirements on the thermal properties, chemical stabilities, and optical properties of the materials, single crystal sapphire and fully stabilized single crystal zirconia are very attractive optical materials for high temperature measurement in harsh environments.

3.1.1 Properties of single crystal sapphire

Unlike other ceramic materials, such as polycrystalline alumina, single crystal sapphire (Al_2O_3) is expected to show superior corrosion resistance because of the elimination of polycrystalline grain boundaries, which have been proven to be vulnerable to corrosion attack [38]. Single crystal sapphire is actually single crystal aluminum oxide ($\alpha\text{-Al}_2\text{O}_3$). Optical grade single crystal sapphire with very low scattering or distortion is commercially available and widely employed for infrared optical windows and domes that must survive in the most demanding environments, such as the head of the laser-guide missiles in battle fields.

- ***Optical properties of single crystal sapphire***

Light transmission in single crystal sapphire material is better than 80% from a wavelength of 0.3 microns in the UV band, through the visible range of 0.4-0.7microns to

5.5 microns in the IR band. In Figure 3.1, the transmission band for a sapphire window with a thickness of 1mm (.039 in) provides a nearly uniform transmission of 85% [56]. The perfection and purity of the UV grade sapphire crystals offer a transmission capability superior to that of the standard grade sapphire. Sapphire’s lower surface scattering losses at the IR wavelengths also require less rigorous surface polishing.

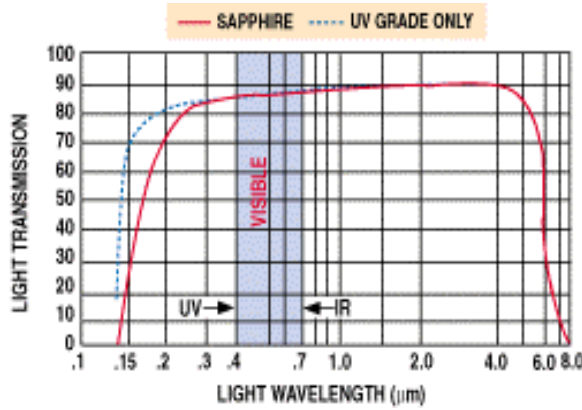


Figure 3.1. The approximate transmission bands of standard- and UV-grade sapphire (window thickness of 0.039 inch).

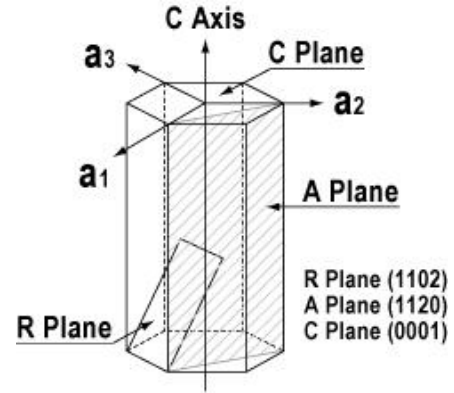


Figure 3.2. Hexagonal inner structure of single crystal sapphire material.

Single crystal sapphire, processing hexagonal crystal structure as shown in Figure 3.2, and has two principal optical axes, along which the refractive indices are different. The unique crystallographic axis is the C-axis, also called optical axis. The refractive index along this axis is n_o . The refractive index along A-axis is n_e . For single crystal sapphire $n_e < n_o$, the values of n_e and n_o are temperature dependent. They can be obtained from the following approximate formula at room-temperature [57], the unit of the wavelength λ is micron (μm):

$$\begin{aligned}
 n_o^2 - 1 &= \frac{1.4313493\lambda^2}{\lambda^2 - 0.0726631^2} + \frac{0.65054713\lambda^2}{\lambda^2 - 0.1193242^2} + \frac{5.3414021\lambda^2}{\lambda^2 - 18.028251^2} \\
 n_e^2 - 1 &= \frac{1.5039759\lambda^2}{\lambda^2 - 0.0740288^2} + \frac{0.55069141\lambda^2}{\lambda^2 - 0.1216529^2} + \frac{6.5927379\lambda^2}{\lambda^2 - 20.072248^2}
 \end{aligned}
 \tag{3.1}$$

- ***Thermo-optic properties of single crystal sapphire***

Since the propagation speed of light in a particular direction in a crystal is a function of the electron density distribution, and the electron probability density distribution is related to the spacing between adjacently bonded atoms, thus the spacing between the atoms affects the speed of light propagation directly. Temperature is one of the main factors affecting the refractive index of solid materials. The thermal expansion coefficients of sapphire are different along the A-axis and C-axis. The change in spacing between the adjacent atoms in each of these directions will be different for a given temperature change. This suggests that the magnitude of the birefringence of the single crystal sapphire will be changing with temperature. With the temperature increase, the atomic arrangements inside the sapphire material are becoming more homogenous, thus the difference between the refractive indices along the A-axis and the C-axis are becoming smaller, i.e. the birefringence is becoming smaller, which has been observed in our experiments.

- ***Thermal stability of single crystal sapphire***

Single crystal sapphire can operate at high temperatures and survive high stress induced by rapid heating. However, the resistance to thermal stress is limited by a loss of mechanical strength at elevated temperature [58-62]. At temperature above 400 °C a dramatic decrease in the sapphire's compressive strength along the C-axis occurs due to the activation of the deformation twinning on the rhombohedral planes.

Various ways to increase the strength of sapphire have been explored, including heat treatments, and doping and improvement of fabrication techniques. Heat treatments at 1450°C for 48 hours in flowing oxygen increase the compressive strength by 60% and biaxial flexure strength by 45% at 600°C. Doping with Mg achieves 160% strength increase over the undoped and unheat-treated baseline strength [63-64].

- ***Mechanical properties of single crystal sapphire***

On the Mohs scale of hardness, which assigns a unit of 10 to diamond, sapphire is rated at 9, quartz at 7, and glass at 4.5–6.5 [56]. Sapphire is an ideal material for the windows that must withstand great pressure or vacuum. In contrast to other available optically transparent materials, sapphire also offers maximum resistance to abrasion and scoring.

- ***Chemical inertness of single crystal sapphire***

Sapphire's chemical inertness in the presence of a wide variety of reagents at temperatures greater than 1000°C makes it ideal for chemical industrial applications. For example, silica becomes soluble in hydrofluoric acid at room temperature, but sapphire exhibits no solubility in alkalies or acids, including hydrofluoric acid. At elevated temperatures, other acids (e.g., hydrochloric acid and nitric acid) attack silica, but not sapphire [56].

3.1.2 Properties of single crystal zirconia

Pure Zirconia (Zirconium dioxide) has a high melting point (2700°C) and a low thermal conductivity as well as chemical corrosive resistance. Its polymorphism, however, restricts its widespread use in ceramic industry. During a heating process, zirconia will undergo a phase transformation process. The change in volume associated with this transformation makes the usage of pure zirconia in many applications impossible. Addition of the appropriate amount of some oxides, such as CaO, MgO, or Y₂O₃, into the zirconia structure results in a solid solution, which is a cubic form and has no phase transformation during heating and cooling. This solid solution material is termed as stabilized zirconia, which is a valuable refractory [56].

Because of its cubic inner structure, the refractive index of the single crystal zirconia is constant, regardless of the crystal orientation, so there is no birefringence associated with the single crystal zirconia. Without adding additional birefringence to the sapphire sensing element, it is thus used as a right angle prism reflector behind the sapphire

sensing element at the end of the sensor probe to reflect light back, forming an one-end probe structure. Another advantage associated with this reflector is that no refraction or reflection (i.e., no scatter) occurs, when light passes from grain to grain of the cubic material.

3.2 Implementation of sensing probes

This sensor system is designed to measure high temperatures directly in harsh environments. The sensing element should thus be physically located in the place where temperature needs to be measured. Certain protection for the sensing element is necessary in such aggressive environments, so that the sensor can monitor the temperature with reliability and durability. Due to its high melting temperature (over 2000°C), superior transparency, and ability to resist corrosion, single crystal sapphire material is chosen to be used as both sensing elements and protection materials for the sensing probe packaging in the designed temperature sensing system.

Following the working principle of the sensor described in Chapter 2, the sensing head structure can be implemented as either a two-end structure (a transmission version of the polarimeter) or a one-end structure (a reflection version of the polarimeter). In most industrial applications, a sensing probe with a one-end structure is more convenient to be deployed, since all of the necessary optical components can be integrated into one solid tube, input light and output light are all at the same end of the sensing probe instead of two separate ends. In this research, two one-end structured sensing probe prototypes were developed with different sensing element structures. One is the sapphire disk, zirconia prism (SDZP) structure, and the other is the sapphire prism (SP) structure.

3.2.1 A sensing probe with a sapphire disk, zirconia prism (SDZP) structure

This structure is a very straightforward implementation of the polarimetric sensor in a reflection mode. In this reflective polarimeter, a light reflector with high temperature survivability is necessary. In low temperature environments, a mirror is commonly used

as a light reflector. The mirror is usually made by coating one surface of a glass plate with different materials, typically dielectrics or metals. Such dielectric or metal coatings can hardly survive the high temperature and chemically corrosive environments, either because the coating materials degrade at high temperature in the chemically corrosive environments, or because the coefficient of thermal expansion (CTE) of the materials do not match well with those of the glass substrate, causing thermal stress on heating or cooling, so that they cannot stick to the substrate and function as a mirror in the high temperature/corrosive environments. Instead, a right-angle prism is an attractive design since the total internal reflection is employed inside to change the light propagation direction by 180°. In the prism, only one type of material is employed, thus the CTE matching problem is avoided for the high temperature applications.

The SDZP structure of sensing probe is shown in Figure 3.3. In this structure, a sapphire sensing disk and a zirconia right angle prism are used, and packaged into a solid sapphire tube for protection. Both the thickness and the birefringence of the sapphire disk change along with temperature changes, thus the temperature information can be obtained by measuring the OPD between the two orthogonal linearly polarized light waves in the sapphire sensing disk. The OPD is related to both the thickness d , and the birefringence Δn of the sensing disk by:

$$OPD = |n_e - n_o|d = \Delta nd \quad (3.2)$$

The polarizer used in this system is an optical grade calcite Glan-Thompson polarizing prism. The light is first collimated by a collimation lens then converted into a linearly polarized optical beam that travels across the free space enclosed by a high temperature ceramic tube and a single crystal sapphire tube to the single crystal sapphire disk (with thickness of 1.5mm and diameter of 30mm). In the sensing probe, the sapphire disk is arranged such that the linear polarization direction of the input light is at 45 degrees with respect to its fast and slow axes. When passing through the sapphire disk, the two linearly

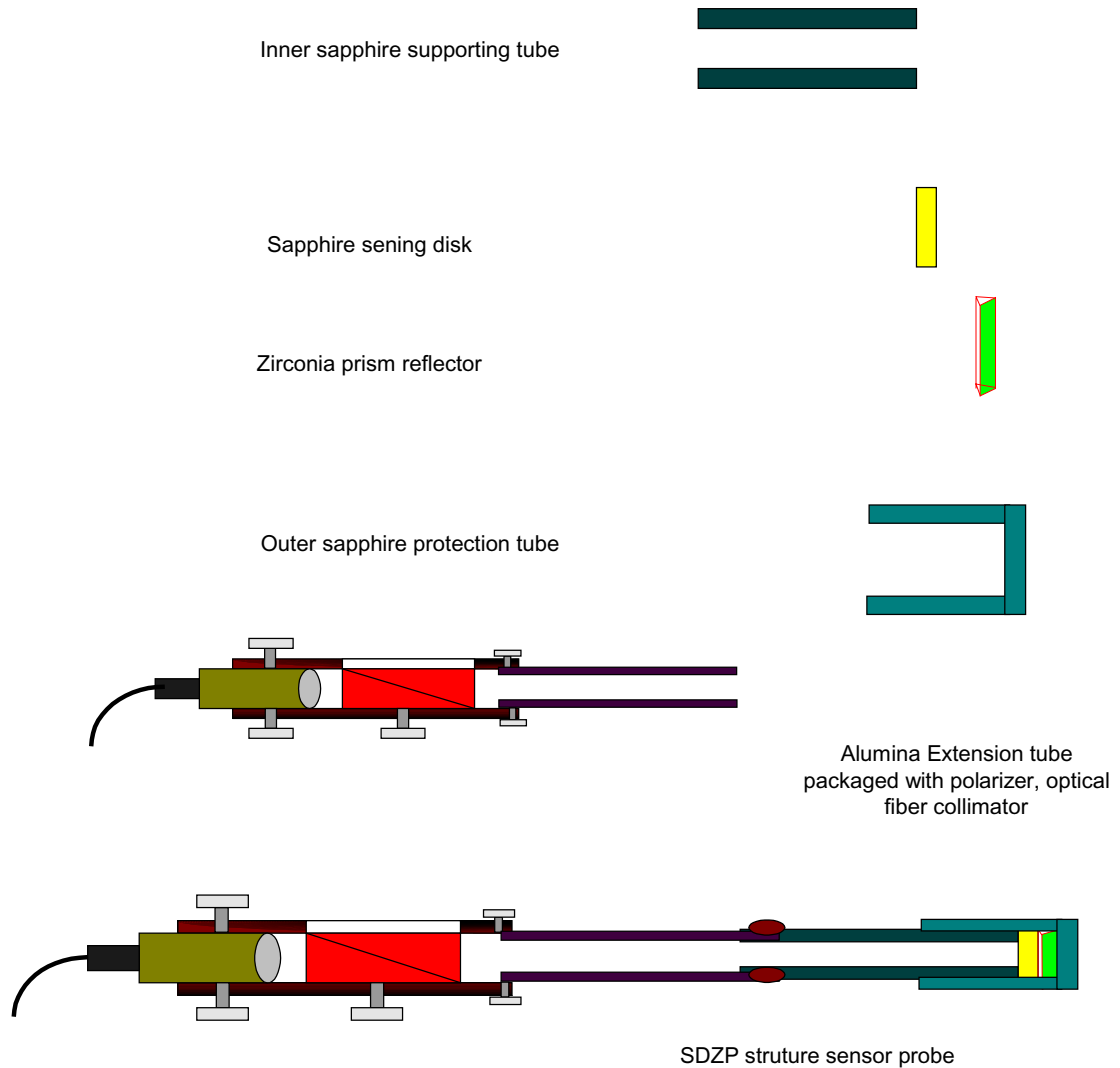


Figure 3.3 A sensing probe with a Sapphire Disk, Zirconia Prism (SDZP) structure

polarized light components along the fast and slow axes experience a differential phase delay due to the sapphire material birefringence and its thickness. The light, containing the two orthogonal linearly polarized light components, is then reflected by the right angle zirconia prism and passes through the sapphire sensing element again, doubling the differential phase retardation. Since the right-angle zirconia prism has no inner birefringence because of its inner cubic crystallographic structure, no additional differential phase delay will be added in the detected optical signals. When light exits the polarimeter, the two linearly polarized light components with a differential phase delay are combined along the polarization direction of the analyzer and interfere with each

other. The output light from the polarimeter is then re-collected by the same input optical fiber bundle and travels back along the optical fiber bundle to the optical detection end which is a fiber optic PC plug-in spectrometer, composed of a grating and a CCD array. Additional signal processing is performed in the computer for temperature information extraction. With the protection of the single crystal sapphire outer tube, the end of the sensor head is heated in a high temperature furnace up to 1600°C and temperature is measured. The measured results are indicative of high accuracy and high resolution.

An extension tube for the sensor head is necessary to avoid thermal damage to the optical fiber collimator and the optical polarizer. These components cannot survive high temperatures over 200°C. The total sensing tube will thus be about two meters long together with the extension tube.

3.2.2 A sensing probe with a sapphire prism (SP) structure

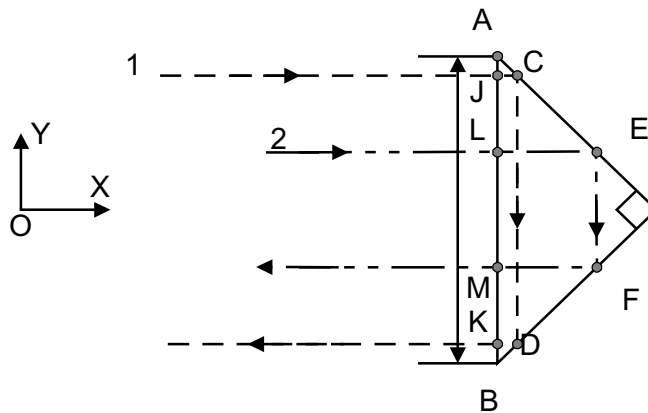
The previously developed sensing probe prototype utilized single crystal sapphire disk as a sensing element and a single crystal zirconia prism as the light reflector in the sensing location. These materials do not have the same CTEs. This may generate instability for the mechanical packaging in high temperature environments. This structure also suffers additional optical reflection losses at the surfaces of the zirconia prism besides the sapphire disk surface reflection losses. From a cost minimization standpoint, an additional single crystal zirconia light reflector will cost more. In the new version of the sensing probe, a novel single crystal sapphire right angle prism, functioning as both a sensing element and a light reflector, is employed. This single crystal sapphire prism possesses a special geometrical structure and crystallographic orientation for those dual functions.

The inherent birefringence property of the single crystal sapphire is needed for the prism to function as a sensing element. As shown in Figure 3.4 (a), when light passes through the right angle prism, it will propagate in three different directions. Beam 1 propagates along JC in the +X direction, along CD in the -Y direction, and along DK in the -X

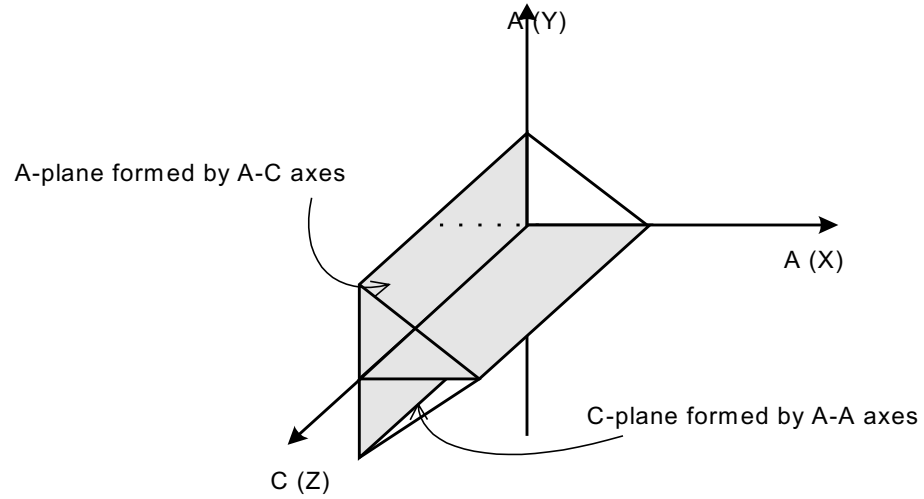
direction. Beam 2 propagates along LE in the +X direction, along EF in the -Y direction, and along FM in the -X direction. Different incident light beams encounter different path lengths in different directions. The crystallographic orientation of the prism is selected as follows. The base of the sapphire prism is A-plane, while both the smaller sides of the prism are C-plane, as shown in Figure 3.4(b). With this crystallographic orientation, when light propagates in the x-direction, such as JC and LE, it experiences the birefringence generated by both the A-axis and C-axis. Because of the symmetric inner atomic structure of the single crystal sapphire, when light propagates in the y-direction, such as CD and EF, it also experiences the birefringence generated by both the A-axis and C-axis. Therefore the total birefringence will be equal regardless of the paths in which optical beams propagate. According to the geometric relationships, all light beams will experience the same length equal to AB when they propagate in the prism. Thus the OPDs for all the input light waves in the prism are:

$$\begin{aligned} OPD_{beam1} &= (|JC| + |CD| + |DK|)\Delta n = |AB|\Delta n \\ OPD_{beam2} &= (|LE| + |EF| + |FM|)\Delta n = |AB|\Delta n \end{aligned} \tag{3.3}$$

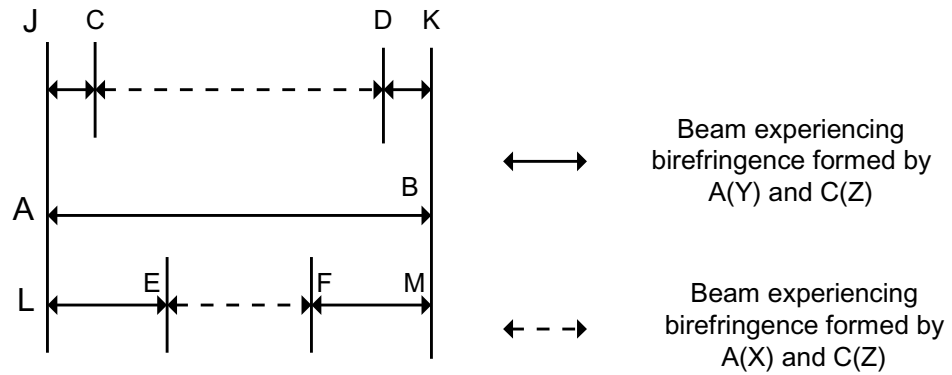
This prism thus functions equivalent to a sensing disk with thickness of the length AB, as well as a light reflector. Figure 3.5 shows the designed geometrical dimensions of the prism and three pieces of the novel single crystal sapphire prisms.



(a) Optical propagation path in the prism

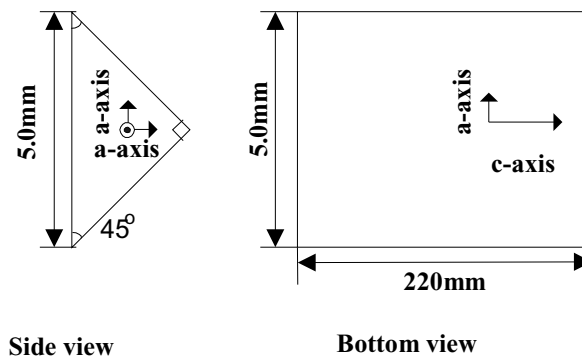


(b) Crystallographic orientation in the prism



(c) Optical path in the sapphire prism is equivalent to the optical path in the sapphire disk

Figure 3.4. Optical propagation in special crystallographic oriented single crystal sapphire right angle prism.



(a) Geometrical sizes of the prism



(b) Fabricated single crystal sapphire right angle prisms

Figure 3.5 Single crystal sapphire right angle prism

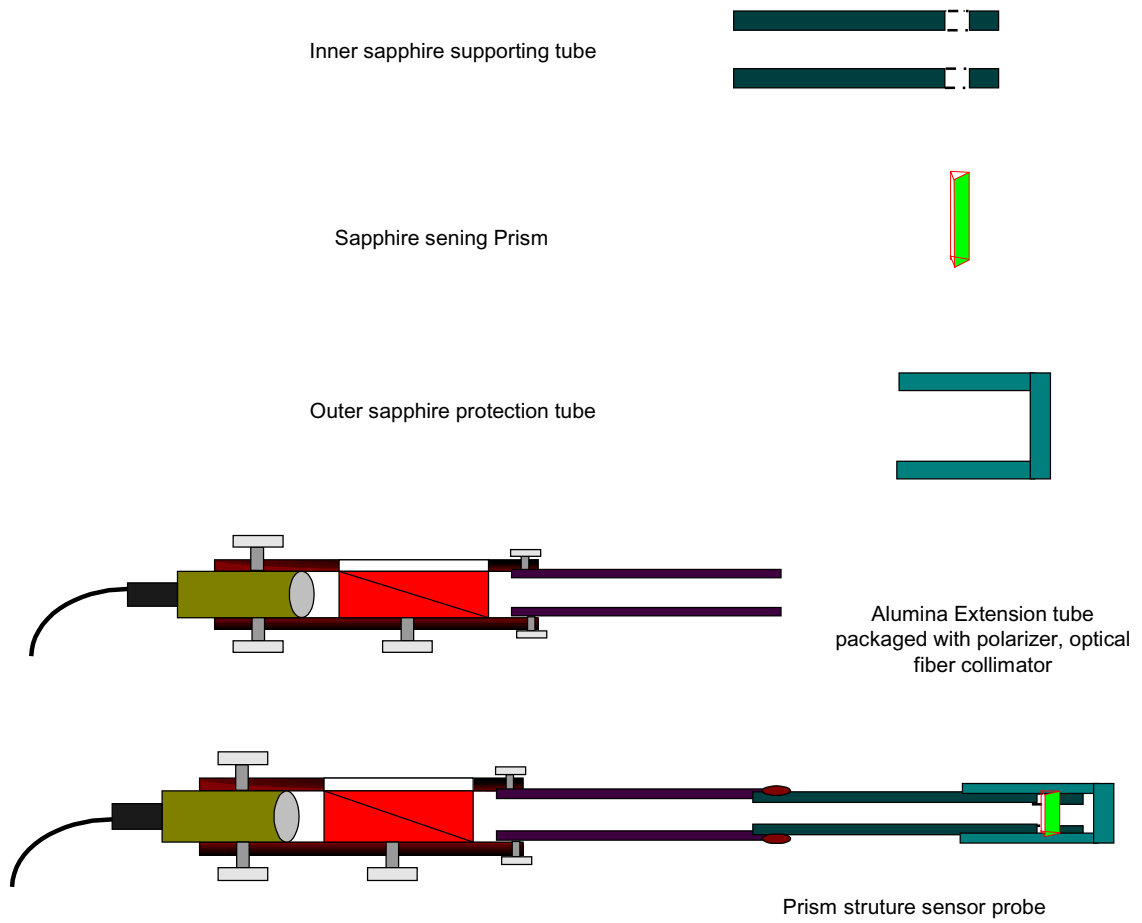


Figure 3.6 Sensing probe with a Sapphire Prism (SP) structure

With a single right angle prism at the end of the sensing probe, the mechanical structure of the sensing head is simplified, as shown in Figure 3.6. The sensing prism is fixed at the end of the inner supporting tube, in which a slot of the correct size to fit the prism is machined. The outer protective sapphire tube covers the inner tube and the sensing prism, with a certain amount of free space between its end and the sensing prism so that the prism can expand freely when the temperature increases. The total sensing tube is about two meters long together with the extension tube, which is used to avoid thermal damage to the optical fiber collimator and the optical polarizer at the other end of the sensing probe.

3.2.3 Total internal reflection in the sensor probe

The right angle prism works as a light reflector in the sensing probe. We want to analyze the optical loss at the reflection surface and the changes of the optical wave polarization states when the light is reflected.

The total internal reflection angle, also called critical angle θ_c for the single crystal zirconia –air interface is:

$$\theta_{c-zirconia} = \sin^{-1}(n_{air} / n_{zirconia}) = \sin^{-1}(1/2.12) = 28.1^\circ \quad (3.4)$$

Total internal reflection angle for the single crystal sapphire-air interface is:

$$\theta_{c-sapphire} = \sin^{-1}(n_{air} / n_{sapphire}) = \sin^{-1}(1/1.76) = 34.7^\circ \quad (3.5)$$

With a 45° reflection angle at the prism-air interface, which is larger than the critical angle, light is totally reflected without loss in those right angle prisms. The light propagation direction is then changed by 180° at the end of the sensing probe by two total internal reflections in the right angle prisms.

In the prism reflector, light is reflected by the total internal reflection, the Jones matrix method can be used to analyze the electric field polarization direction changes at the reflection surfaces [66]. The electric field vector of the input light is related to the electric field vector of the output light by:

$$\vec{E}_{out} = T\vec{E}_{in} \quad (3.6)$$

the Jones matrix T is given by

$$T = \begin{pmatrix} \rho_x & 0 \\ 0 & \rho_y \end{pmatrix} \quad (3.7)$$

where,

$$\begin{aligned} \rho_x &= \frac{1 + i\alpha}{1 - i\alpha} \\ \rho_y &= \frac{n_0^2 + in^2\alpha}{n_0^2 - in^2\alpha} \\ \alpha &= \frac{(n^2 \sin^2 \psi - n_0^2)^{1/2}}{n \cos \psi} \end{aligned} \quad (3.8)$$

n is the refractive index of the single crystal sapphire or the single crystal zirconia, $n_0=1$ is the refractive index of air, and ψ is the incident angle of light in the prism, which is 45° , for light reflected at the critical angle,

$$\begin{aligned} \psi_c &= \sin^{-1}(n_0/n) \\ \rho_x &= \rho_y = 1 \end{aligned} \quad (3.9)$$

then the Jones matrix reduces to an identity matrix, which means the total internal reflections in the right angle prism do not change the polarization directions of the reflected light, thus no additional phase shift will be induced between the two orthogonal linearly polarized light waves.

3.3 Signal processor and software implementation

3.3.1 Signal processor implementation

An important part of the spectral domain white light interferometry signal processor is the spectrometer. The performance of the whole system, such as measurement resolution and stability, are highly dependent on the performance of the spectrometer. In a traditional spectrometer based system where a cumbersome and expensive spectrometer is used, the strict requirements to environmental conditions exclude the possibility to use this kind of instrument in real industrial fields. In the designed system, a compact fiber

optic spectrometer (USB2000 manufactured by Ocean Optics, Inc.) is used. Its key features are listed in Table 3.1.

Table 3.1. The Key Features of the optical spectrum analyzer USB2000:

Computer interface	Universal Serial Bus (RS-232 available on side connector)
Integration time	3 milliseconds-65 seconds
Data transfer rate	Full scans (2048 wavelengths) into memory every 13 milliseconds
Dimensions: (Length*Width*Hight)	3.5" x 2.5"x 1.31" 89 mm x 64 mm x 34 mm
Weight	0.45 lb. without cable 0.60 lb. with cable
Detector	2048-element linear silicon CCD array
Effective range	800-900 nm
Sensitivity (estimate)	86 photons/count;
Signal-to-noise	250:1 (at full signal)
Dark current noise	2.5-4.0 pA (RMS)
Slits	optical fiber is entrance aperture
Focal length	42 mm (input); 68 mm (output)
Resolution	~ 0.3 nm-10.0 nm FWHM
Stray light	< 0.05% at 600 nm; < 0.10% at 435 nm; <0.10% at 250 nm
Fiber optic connector	SMA 905 to single-strand optical fiber (0.22 NA)

The input fiber is connected to the spectrometer directly through a SMA connector. Inside the spectrometer, a 1200 line holographic grating is used to diffract the input light on a 2048 pixels CCD array. The output electrical signals from each pixel in the CCD array will be read out serially and converted into digital format by a built-in analog/digital (A/D) card. The measured spectrum is then transferred into a computer for further signal processing. Figure 3.7 shows the structure of a single channel spectral

domain white light signal processor, including an optical fiber coupler, an optical spectrometer, a LED light source and an electrical power supply.

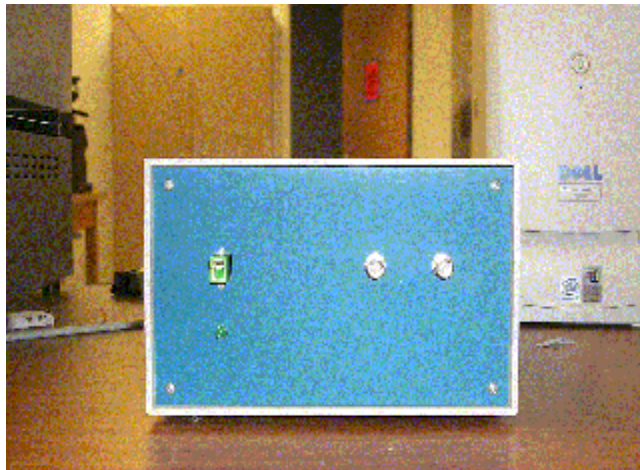
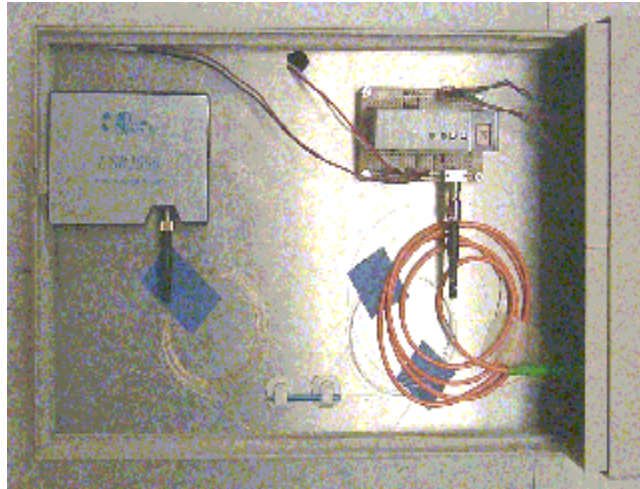
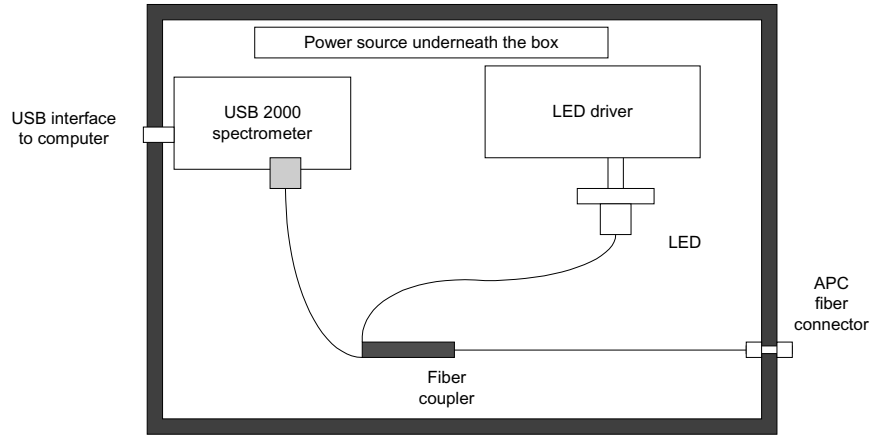


Figure 3.7. Single channel spectral domain white light signal processor

3.3.2 Signal processing algorithm development

According to the working principle of the white light interferometry shown in Equation (2.5), OPD between the two orthogonal linearly polarized light beams can be obtained from the measured spectrum fringe patterns. The existing algorithms for the OPD calculations either possess high resolution with limited measurement range (such as the peak tracing method), or large dynamic measurement range with limited resolution (such as the two-point method). A novel algorithm is then adopted for the BPDI sensor system to achieve both high resolution and large dynamic range simultaneously.

Peak tracing method

Based on the measured spectrum fringes patterns, the value of the OPD can be obtained through tracing a special point in the interference fringes (such as one peak point). In this method, the wavelength λ_m of a peak point in the interference spectrum satisfies the relationship:

$$\frac{2\pi L}{\lambda_m} = \frac{2\pi d \Delta n}{\lambda_m} = m2\pi \quad (3.10)$$

where the spectral order m is a non-negative integer. Equation (3.10) can be rewritten into the following form:

$$L = \frac{m2\pi\lambda_m}{2\pi} = m\lambda_m \quad (3.11)$$

To calculate the OPD value L from a special peak wavelength λ_m , the interference order m must be known first. For the selected peak, the identification of the interference order m is difficult so that the unambiguous operating range of the OPD is limited in only half of the wavelength range. The resolution of this peak tracing method is mainly dependent

on the resolution of the spectrometer as shown in Equation (3.11). The relative uncertainty of the measurement can be described as

$$\left| \frac{\Delta L}{L} \right| \cong \left| \frac{\Delta \lambda}{\lambda} \right| \quad (3.12)$$

where $\Delta \lambda$ is the measurement resolution of the wavelength, determined by the measurement resolution of the spectrometer.

Two-point method

To increase the measurement range of the OPD values, two special points instead of one point in the interference spectrum need to be used for the absolute measurement. Suppose λ_1 and λ_2 ($\lambda_1 > \lambda_2$) are the wavelengths of the two adjacent peak points in the interference spectrum. Their interference orders are m and $m+1$. From Equation (2.10),

$$\begin{aligned} \frac{2\pi L}{\lambda_1} &= m2\pi \\ \frac{2\pi L}{\lambda_2} &= (m+1)2\pi \end{aligned} \quad (3.13)$$

The OPD can be determined,

$$L = \frac{\lambda_1 \cdot \lambda_2}{\lambda_2 - \lambda_1} \quad (3.14)$$

The wide dynamic measurement range can then be obtained by using two special wavelengths, as long as the two such special wavelengths exist (two peaks or two valleys) in the spectrum pattern, the OPD can then be calculated by Equation (3.14). In this case, the relative uncertainty induced by the spectrometer is

$$\left| \frac{\Delta L}{L} \right| \cong \left| \frac{\lambda_2}{\lambda_2 - \lambda_1} \right| \cdot \left| \frac{\Delta \lambda_1}{\lambda_1} \right| \quad (3.15)$$

If the central wavelength of the light source (LED) is 850nm, for the operating range of OPD (40-60 μm), this factor $\left| \frac{\lambda_2}{\lambda_2 - \lambda_1} \right|$ is about 110—150. Thus, this method has lower resolution in a large dynamic measurement range compared to the peak tracing method.

New algorithm

Combining the advantages of the two methods described above, a novel data processing algorithm has been developed in CPT [66], which can achieve both high resolution and large dynamic range.

The basic idea of this method is to use two peak points in the interference spectrum to get a rough OPD value first (large dynamic range is then achieved); this rough OPD is then used to determine the rough order number m_r of a special peak point in the interference fringes. Then, an accurate m_a value will be recovered from the rough m_r . From Equation (3.11), the accurate OPD can be calculated based on the accurate m_a and the peak wavelength location in the spectrum (high resolution is thus achieved).

The algorithm used to recover the accurate m_a is the following:

In Equation (3.11), for a given peak, m is a constant value. For adjacent peaks, the difference between the interference orders is 1. For example, if m for one peak is 12, then for the adjacent peaks the interference order will be 13, 14, 15...and 11, 10, 9....By calibration, the value of m for a special peak (m^o) can be acquired accurately and stored in computer. When the rough m_r value for any peak has been acquired, the accurate m_a will be obtained from m^o by adding the integer part in the difference between the rough m_r and m^o . The whole process of demodulating OPD from the interference spectrum can then be separated into two sub-processes: the calibrating sub-process and the measuring sub-process.

With the white light interferometer system in a stable condition, the OPD is set to a known value L_0 . The m^o of a peak in the interference spectrum can be calculated accurately from the L_0 and the wavelength λ_0 . This is the calibrating sub-process.

With known m^o , the measuring sub-process can be carried out as follows:

1. Use the two peak points in the interference spectrum to acquire a rough value of L_r using Equation (3.14);

2. Select a peak point near the center of the interference spectrum, then use the wavelength of this peak and the rough L_r from previous step to calculate a rough m_r ';

3. The accurate m_a can be calculated from m_r and the stored m_o from:

$$m_a = m_o + \text{int}(m_r - m_o + 0.5) \quad (3.16)$$

Where function $\text{int}(\dots)$ means to take the integral part.

4. The accurate OPD can be calculated from the accurate m_a and the wavelength of the peak with Equation (3.11).

3.3.3 Software design and implementation

Advanced computer software has been developed to demodulate the OPD values from the interference spectral patterns, based on the novel data processing algorithm presented previously. The software program is implemented in the combination of Microsoft Visual Basic and C++ languages so that both the graphic interfaces and high computational speed are achieved and optimized. The block diagram of the program is shown in Figure 3.8.

The program is described in detail below:

Initialization

The program starts with the hardware initialization, which includes the initialization of the spectrometer. Then most of the important parameters, which are stored in the computer, will be restored in the memory of the computer. These data include the parameters for setting up the spectrometer such as the integration time, scanning time interval, the calibrated interference order m_o value, the reference spectrum of the light source, the dark current noise of the spectrometer, and the calibration curve of the temperature sensor.

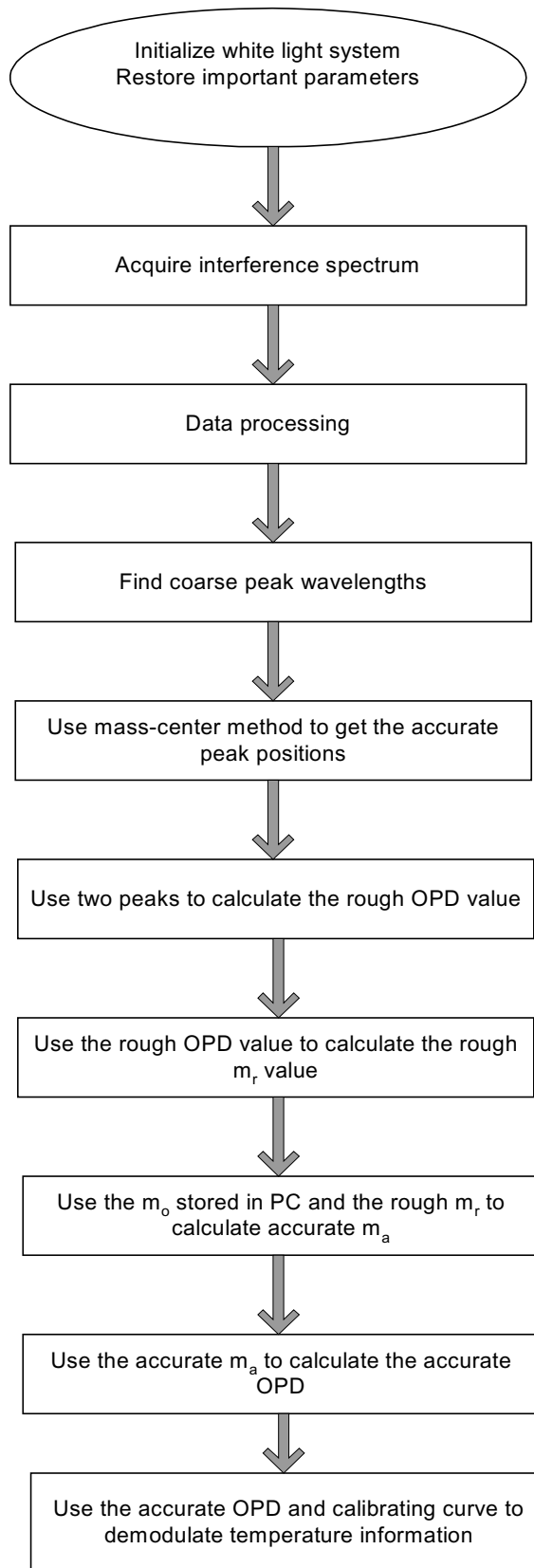


Figure 3.8. Block diagram for the implementation of the OPD calculation algorithm

Spectrum acquisition

The interference spectrum from the sensor head will be sampled according to the given time interval. Once the optical signal is coupled into the spectrometer through a SMA connector from the optical fiber, the divergent light emerged from the optical fiber will be collimated by a spherical mirror. Then, a plane grating is employed to diffract the collimated light. A second spherical mirror then focuses the diffracted light and an image of the spectrum is projected onto a 1-dimensional 2048 pixels linear CCD array. The CCD array is actually serially connected reverse-biased photodiodes, they discharge a capacitor at a rate proportional to the photon flux. When the integration period of the detector is complete, a series of switches closes and transfers the charge of each pixel to a shift register. After the transfer to the shift register is complete, the switches open and the capacitors attached to the photodiodes are recharged and a new integration period begins. At the same time as light energy is being integrated, the spectrum data is read out of the shift register by a built-in A/D card. In the last step, the spectral data will be acquired by a computer through a USB interface.

Data processing

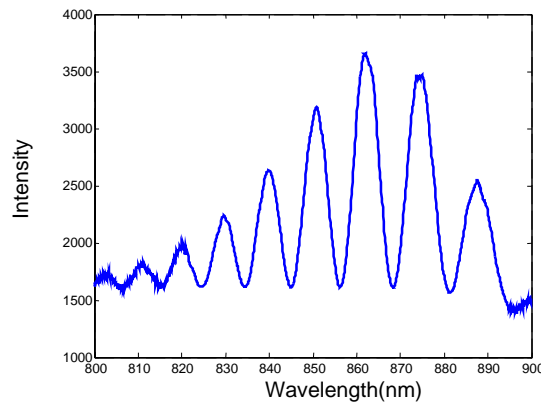
To demodulate the temperature information from the interference spectrum accurately, an advanced data processing algorithm has been developed and implemented in the Microsoft Visual Basic environments. This part is the core of the whole program, and will be discussed in several sub-steps, as data pre-processing for blackbody radiation background subtraction, peaks and valleys localization and signal demodulation for the temperature measurement.

Data pre-processing

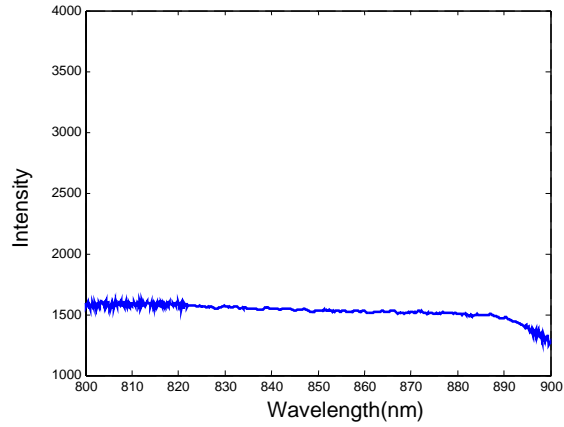
The original spectrum data from the spectrometer is a 1x2048 array, which composes the received light signals from the 2048 pixels of the CCD array. To recover the interference spectrum, the calibrating curve of the CCD array is used to calculate the optical wavelengths according to the serial number of array. To remove the dark current noise of the CCD detector and other background noise, a dark spectrum stored in the computer is

subtracted from the measured spectrum. The dark spectrum is pre-acquired when the light source is not powered.

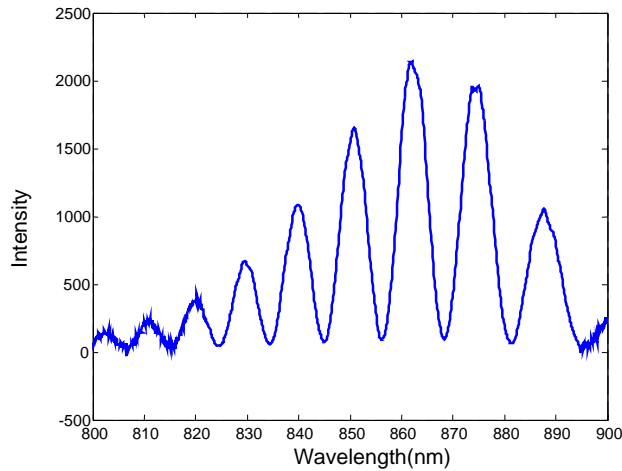
As discussed in Chapter 2, modulation of the optical signal is needed to convert the temperature probing light into AC signals, so that the blackbody radiation background can be subtracted as a DC signal. The straightforward way to implement this modulation and demodulation scheme is to modulate the optical source with a square wave with certain frequency, so that the probing light will be on and off following the square wave. When the probing light is on, the detected signals will contain both the blackbody radiation and optical signals with temperature information. The measured optical spectrum is as shown in Figure 3.9 (a). When the probing light is off, only blackbody radiation background is detected by the spectrometer as shown in Figure 3.9(b). Since the blackbody radiation background is a slowly changing signal that follows the temperature changes, it can be treated as constant during the time interval when the probing light is on and off. Thus, the blackbody radiation can be subtracted, resulting in a spectrum as shown in Figure 3.9 (c). The square wave used to modulate the LED is shown in Figure 3.10. The frequency of the square wave is 8Hz. The modulated output light from the LED is shown in Figure 3.11. The light intensity curve is measured with a low quality optical detector, so the signal noise ratio is poor, which does not represent the real optical signal intensity levels.



(a) Measured spectrum in the presence of blackbody radiation at 1200 °C



(b) Measured spectrum of blackbody radiation at 1200 °C



(c) Spectrum after blackbody radiation subtraction at 1200 °C

Figure 3.9 Illustrating a blackbody radiation subtraction

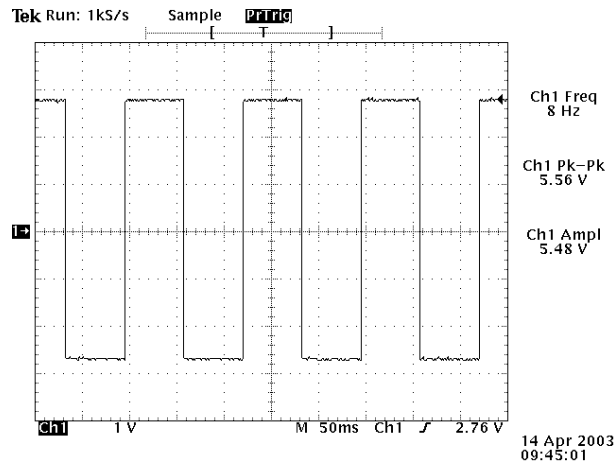


Figure 3.10 . Electrical square wave used to modulate the LED

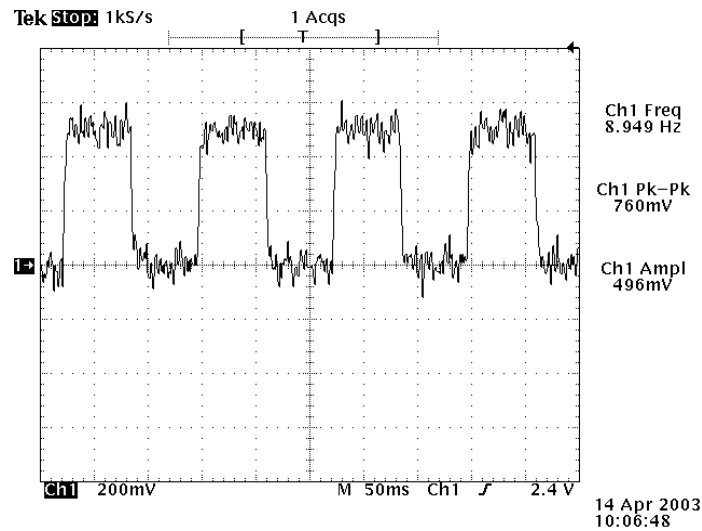


Figure 3.11. Modulated output optical signal from the LED

Peaks and valleys localization

Desired peak positions in the interference spectrum are selected to demodulate the OPDs between the two orthogonal linearly polarized light waves. The valley positions in the interference spectrum can also be located with a similar method. The technique for locating peaks is described as follows:

The first step is to find the coarse locations of the peaks by a smart comparison algorithm. The basic idea of this algorithm is to find all the local maximum points in a special range in the interference spectrum. The size of the searching range, which is defined as the window size of the peak searching, must be large enough to eliminate the influence of the noise. To avoid missing some peaks, the window size must be smaller than the space between adjacent peaks.

After the coarse positions of the peaks are found, a mass-centroid algorithm is applied to find the accurate positions of the peaks. The basic idea of the mass-centroid algorithm is shown in Figure 3.12. If the function $Y(x)$ is symmetric around its peak position, then the peak position coincides with the x coordinate of the centroid of $Y(x)$.

As shown in Figure 3.12, the peak position X_0 can be calculated from:

$$X_0 = \frac{\int_{-\infty}^{+\infty} xf(x)dx}{\int_{-\infty}^{+\infty} f(x)dx} \quad (3.17)$$

From Equation (2.5), around the peak point, the spectrum is a symmetrical function of the wave number $k=1/\lambda$. So the spectrum $y(\lambda)$ needs to be expressed in terms of the wave number first (from $\{y_i, \lambda_i\}$ to $\{y_i, k_i\}$).

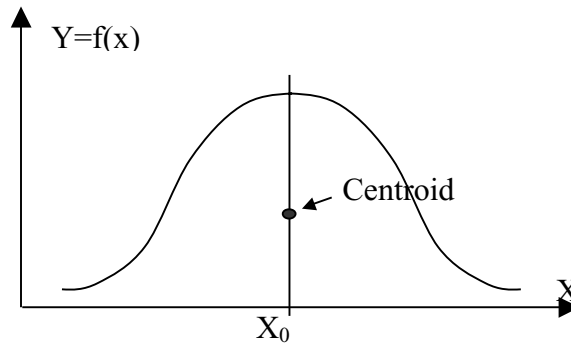


Figure 3.12 Mass-centroid method for peaks locating in the spectrum

With the normalized spectrum $\{y_i, k_i\}$, the accurate peak positions can be calculated from the coarse peak positions:

$$k_i = \frac{1}{\lambda_i}$$

$$k_m^p = \frac{\sum_{i=-\infty}^{+\infty} y_i k_i (k_i - k_{i-1})}{\sum_{i=-\infty}^{+\infty} y_i (k_i - k_{i-1})} \quad (3.18)$$

$$\lambda_m^p = \frac{1}{k_m^p}$$

Demodulation of the temperature information

Once the peak positions are acquired, the temperature can be demodulated as described below:

A coarse OPD is calculated using two peak positions, and then the rough m_r value for a selected peak near the center wavelength is determined. Using the calibrated m_0 value

stored in the computer, the accurate m_a value is obtained and then is used to calculate the accurate OPD values. Finally, using the calibration curve, the temperature is extracted from the accurate OPDs.

3.4 Overview of BPDI temperature sensor system

Based on the BPDI technology, a portable temperature-sensing probe is formed, where the sensing element is located at the end of the sensing probe. This structure of the sensing head is simplified by eliminating one polarizer and one light collimator compared with the two-end structure.

In Figure 3.13, the broadband light from a high power light emitting diode (LED, $480\mu\text{W}$ output after coupling into a $200\mu\text{m}$ diameter pigtail fiber), has a center wavelength at 850nm and its spectrum covers a range from 800nm to 900nm . The modulated light pulses (represented by yellow blocks) are injected into a 2-meter long lead-in multimode optical fiber bundle and propagates to the sensor head. The polarizer used in this system is an optical grade calcite Glan-Thompson polarizing prism. The light is first collimated by a collimation lens, then converted into a linearly polarized optical beam and travels across a free space enclosed by a high temperature ceramic tube and a single crystal sapphire tube to a sensing element.

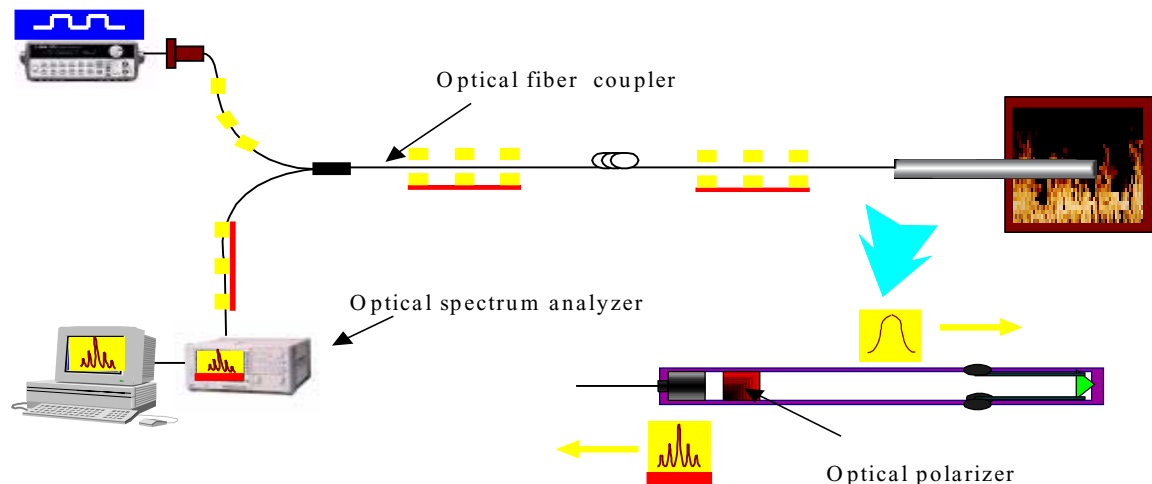


Figure 3.13. BPDI sensor system overview

The sapphire-sensing element is arranged such that the input linear polarization direction of light is at 45 degrees with respect to its fast and slow axes. When light passing through the sapphire sensing element, the two linearly polarized light components along the fast and slow axes experience a differential phase delay due to the sapphire birefringence and its thickness. The light, containing the two orthogonal linearly polarized light components with relative phase delays, is then reflected by a reflector, the reflector can be a single crystal zirconia right angle prism or a sapphire sensing right angle prism. The output light from the sensing probe is then re-collected by the same input optical fiber bundle and travels back along the optical fiber to the optical detection end, which is a fiber optic PC plug-in spectrometer, composed of a grating and a CCD array. The intensities of the dispersed spectral components of the signal are scanned electronically by the CCD array, with a spectral resolution of 0.3nm. Additional signal processing is performed in the computer. As a temperature reference, a type K thermocouple (resolution 0.05 °C) is used for temperatures lower than 200 °C, and a type B high-temperature thermocouple (resolution 0.2 °C under 500 °C and 0.1°C above 500 °C) is used for temperatures above 200 °C. The sensor head is heated in a high temperature furnace up to 1600°C for its performance testing.

The total length of the sensing probe is 2 meters long and fabricated with high temperature ceramic material with a low thermal conductivity, which is sufficient to isolate thermal damage of the optical elements (optical fiber, collimation lens and polarizer) from sensing location (temperature over 1600°C). After passing through 4 meters long free space (round trip in the sensing probe), it is usually difficult to re-collect optical energy into the optical fiber. To solve this problem, a fiber bundle with one fiber at the center surrounded by six fibers is used. The diameter of each fiber is 200µm. Light exits from the center fiber, the other six fibers re-collect light reflected back from the sensing probe, through a diameter of 22mm collimation lens with a 35mm focal length. About 10% of the input light can be recollected from the sensing probe with this collimation lens and the fiber bundle, thus the recollected optical power is sufficient to be detected by the CCD array in the spectrometer.

Chapter 4. System noise analysis and performance optimization

As an optoelectronic measurement system, the performance of the BPDI sensor is limited by the noise associated with individual electronic and optical components and their combined effects. A detailed analysis of these noise effects on the system performance is a very important design step since it provides a guideline to achieve an optimal system performance.

As discussed in Chapter 3, the optical components in the BPDI sensor system include an optical source (LED), an optical fiber, an optical collimator, a polarizer, and an optical sensing element. In order to achieve the desirable performance of the sensor system, it is necessary for these optical components to perform their functions accurately. Unfortunately, environmental perturbations, such as temperature variations and mechanical vibrations, can easily introduce noise to the system through the interaction between the optical components and the host media. These noises may cause the optical components to deviate from their desired functions and result in measurement errors.

Instead of analyzing the noise performance of each of the individual optical components in the sensor system, we study the all-possible degradation factors on the temperature signatures, i.e the normalized interference spectrum. This chapter is dedicated to discuss these degradation factors, including the optical spectrum characteristic variations relative to the pre-stored optical source spectrum used for the normalization; the visibility of the normalized spectrum; the mechanical vibrations; transmission fiber generated spectrum distortion and electrical noise inside the spectrometer. These degradation factors might be due to noises generated by one single component or combined noises from several different components. The advantage of this method is to get a systematic view and then design compensation methods to optimize the system performance.

4.1 Optical spectrum induced noise

The BPDI sensor system measures temperatures through detecting the OPDs in the

sensing element sandwiched in a polarimeter in the optical spectral domain. The optical power fluctuation of the source is no longer a concern in this system, while the spectrum characteristic changes will affect the OPD measurement thus the temperature measurement accuracy.

The output spectrum of the LED is pre-measured and pre-stored in a computer as a reference spectrum for the normalization purposes. Suppose the central wavelength of the reference spectrum is λ_0 and the spectral bandwidth of the light source is w , then the spectral intensity distribution of the LED radiation can be approximated as a Gaussian curve as shown in Figure 4.1:

$$I(\lambda) = I_0 \exp\left(-\frac{(\lambda - \lambda_0)^2}{w^2}\right) \tag{4.1}$$

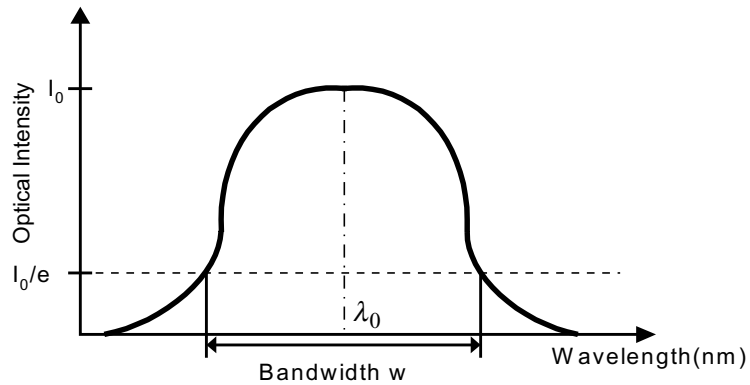


Figure 4.1 Gaussian spectral intensity profile from a low coherence source (LED)

When the ambient conditions change, the wavelength of the LED will drift, i.e the center wavelength λ_0 is changed, or the spectral bandwidth is broadened or narrowed. Most likely, the changes of these two factors will occur simultaneously during the temperature measurement process. To illustrate their effects on the temperature measurement, these two cases will be analyzed separately.

4.1.1 Wavelength drift

Two components in the BPDI sensor system may induce the center wavelength drifts: the LED source and the optical spectrometer. The measurements from the optical

spectrometer are temperature dependent, resulting from the temperature dependent performances of its components (the volume grating and the CCD array). Also determined by the characteristic of the fabrication materials of the semiconductor optical sources, the spectrum of the LED is temperature dependent, and the central wavelength of the LED will shift to longer wavelength as the temperature increases. When the temperature changes from T_0 to T , the central wavelength of the LED will drift from λ_0 to λ_T . In the designed working temperature range from $-50\sim 80$ °C, which is normally experienced by the electronics at the room environments, λ_T can be expressed in term of the temperature T :

$$\delta_\lambda = \lambda_T - \lambda_0 = a(T - T_0) = a\Delta T \quad (4.2)$$

where a is a constant, and roughly equals to $0.2\text{-}0.3\text{nm}/^\circ\text{C}$.

The temperature dependence of the light source in the BPDI sensor system is measured experimentally. The light source is kept in an electric oven; the spectrometer and the sensing head were kept in the room environment. The temperature of the oven is increased to 50°C , and kept at that temperature for about 2 hours. Then the temperature was decreased to room temperature slowly (in about 3 hours). During the temperature decreasing process, a thermocouple is used to monitor the temperature in the oven, and the output spectrum of the LED is measured by the OceanOptics spectrometer. Figure 4.2 shows the test results. The temperature coefficient of the LED is estimated to be about $0.27\text{nm}/^\circ\text{C}$.

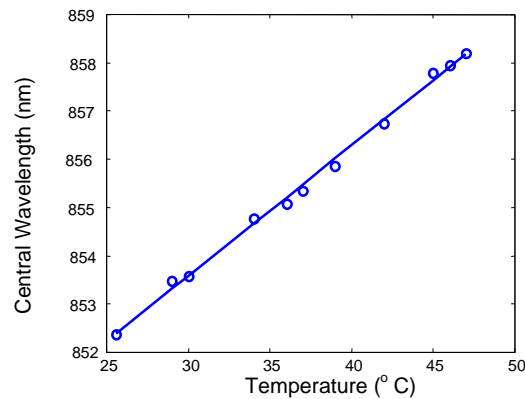


Figure 4.2 Temperature dependence of the central wavelength of the LED

Without wavelength drifts, sinusoidal curves defined by Equation (2.5) containing temperature information, is obtained after normalization of Equation (2.4) to Equation (2.3). Suppose the wavelength of the peak point is λ_p , from Equation (2.5), at the peak point, we have:

$$\left. \begin{array}{l} \cos\left(\frac{2\pi L}{\lambda_p}\right) = 1 \\ \sin\left(\frac{2\pi L}{\lambda_p}\right) = 0 \end{array} \right\} \Rightarrow \frac{2\pi L}{\lambda_p} = 2k\pi \Rightarrow L = k\lambda_p, \text{ k is a positive integer} \quad (4.3)$$

With a known k value, we can calculate OPD from λ_p , which in turn can be related to temperature information by calibration.

Since no method can be used to acquire the spectrum of the LED in real time for the interference spectrum normalization, the pre-recorded reference spectrum acquired at temperature T_0 is used to normalize the interference spectrum acquired at temperature T . The normalized spectrum $N(\lambda)$ is then expressed as:

$$N(\lambda) = \frac{\exp\left(-\frac{(\lambda - \lambda_T)^2}{w^2}\right)}{\exp\left(-\frac{(\lambda - \lambda_0)^2}{w^2}\right)} (1 + \gamma \cos\left(\frac{2\pi L}{\lambda}\right)) \quad (4.4)$$

The normalized curve is a product of the sinusoidal curve, which contained the OPD information for the temperature measurements, and the ratio between the two optical spectrum curves corresponding to different temperatures. This ratio is not equal to unity because of the center wavelength drift. One normalized curve is plotted in Figure4.3, where the OPD is chosen to be $9.2\mu\text{m}$, the spectral width w is 27nm , visibility of the interference spectrum γ is 0.5 , and the shift of the central wavelength is 5nm . Figure 4.4 shows the measured normalized spectrum when the temperature was increased to 45°C (the reference spectrum was acquired at 25°C). Obviously, with the use of a reference spectrum acquired at different temperatures, the normalized spectrums are deformed from

the sinusoidal curve and the peak/valley locations in the interference spectrum are shifted.

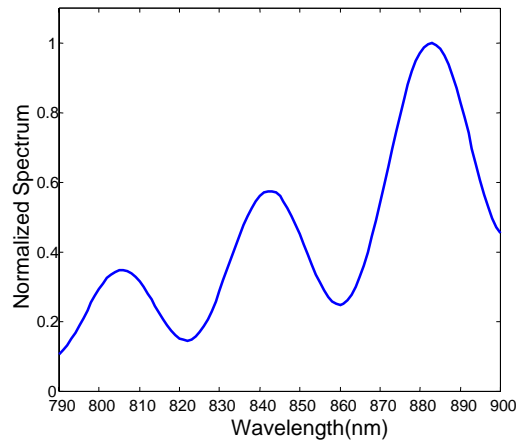


Figure 4.3 Simulated results of the normalized spectrum with center wavelength shift effect

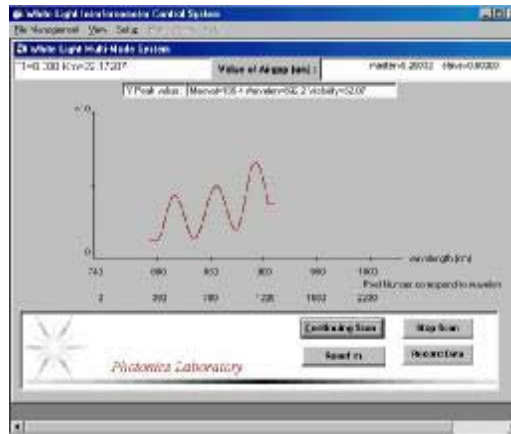


Figure 4.4. Measurement results of the normalized spectrum at 45°C (the reference is acquired at 20°C)

Let us analyze quantitatively the temperature uncertainty caused by the center wavelength drift.

After the center wavelength of the spectrum drifts to λ'_0 , the output spectrum from the LED source becomes:

$$I(\lambda) = I_0 \exp\left(-\frac{(\lambda - \lambda'_0)^2}{w^2}\right) \quad (4.5)$$

Because of the wavelength drift, the temperature measurement will be affected, and the new normalized curve will be:

$$N(\lambda) = \frac{I'(\lambda)}{I(\lambda)} = \frac{\exp\left(-\frac{(\lambda - \lambda'_0)^2}{w^2}\right)}{\exp\left(-\frac{(\lambda - \lambda_0)^2}{w^2}\right)} (1 + \gamma \cos\left(\frac{2\pi L}{\lambda}\right)) \quad (4.6)$$

Assuming that $\delta\lambda = \lambda'_0 - \lambda_0$, and consider $|\delta\lambda/\lambda_0| \ll 1$, then using a first order approximation yields,

$$\frac{\exp\left(-\frac{(\lambda - \lambda'_0)^2}{w^2}\right)}{\exp\left(-\frac{(\lambda - \lambda_0)^2}{w^2}\right)} \approx \left(1 + \frac{2(\lambda - \lambda_0)}{w^2} \delta\lambda\right) \quad (4.7)$$

The normalized Equation (4.6) becomes:

$$N(\lambda) = \frac{I'(\lambda)}{I(\lambda)} = \left(1 + \frac{2(\lambda - \lambda_0)}{w^2} \delta\lambda\right) \times \left(1 + \gamma \cos\left(\frac{2\pi L}{\lambda}\right)\right) \quad (4.8)$$

The shifted peak position λ'_p can be acquired by differentiating Equation (4.8) and setting it equal to zero,

$$\begin{aligned} \frac{\partial N}{\partial \lambda} \Big|_{\lambda=\lambda'_p} &= \frac{2\delta\lambda}{w^2} + \frac{2\pi L \gamma}{\lambda_p'^2} \sin\left(\frac{2\pi L}{\lambda_p'}\right) + \frac{2\delta\lambda}{w^2} \gamma \cos\left(\frac{2\pi L}{\lambda_p'}\right) \\ &+ \frac{2(\lambda'_p - \lambda_0)\delta\lambda\gamma}{w^2} \times \frac{2\pi L}{\lambda_p'^2} \times \sin\left(\frac{2\pi L}{\lambda_p'}\right) = 0 \end{aligned} \quad (4.9)$$

Because $\Delta\lambda = \lambda'_p - \lambda_p \ll \lambda_p$, from Equation (4.3), we obtain,

$$\begin{aligned} \cos\left(\frac{2\pi L}{\lambda_p'}\right) &\approx 1 \\ \sin\left(\frac{2\pi L}{\lambda_p'}\right) &\approx \sin\left(\frac{2\pi L(\lambda_p - \Delta\lambda)}{\lambda_p^2}\right) = \sin\left(2k\pi - \frac{2\pi L \Delta\lambda}{\lambda_p^2}\right) \approx -\frac{2\pi L \Delta\lambda}{\lambda_p^2} \end{aligned} \quad (4.10)$$

Substituting these two equations into Equation (4.9) and assuming that $\delta\lambda/w \ll 1$, $\Delta\lambda/\lambda_p \ll 1$, a first order approximation yields:

$$\lambda'_p = \frac{(1+\gamma)\lambda_p^4}{4\pi^2\gamma L^2 w^2} \delta\lambda + \lambda_p \quad (4.11)$$

From Equation (3.11), the OPD demodulated from the shifted peak wavelength λ'_p is:

$$L'_\lambda = m\lambda'_p = \frac{\lambda'_p}{\lambda_p} L \quad (4.12)$$

Using Equation (4.11) and Equation (4.12), we obtain:

$$L'_\lambda = L + \frac{(1+\gamma)\lambda_p^3}{4\pi^2\gamma L w^2} \delta\lambda \quad (4.13)$$

Equation (4.13) is used to evaluate the wavelength shift induced OPD measurement uncertainties (δOPD) in Figure 4.5. The temperature measurement uncertainties can be obtained from Figure 4.6 through the calibration relation between the OPD and the temperature.

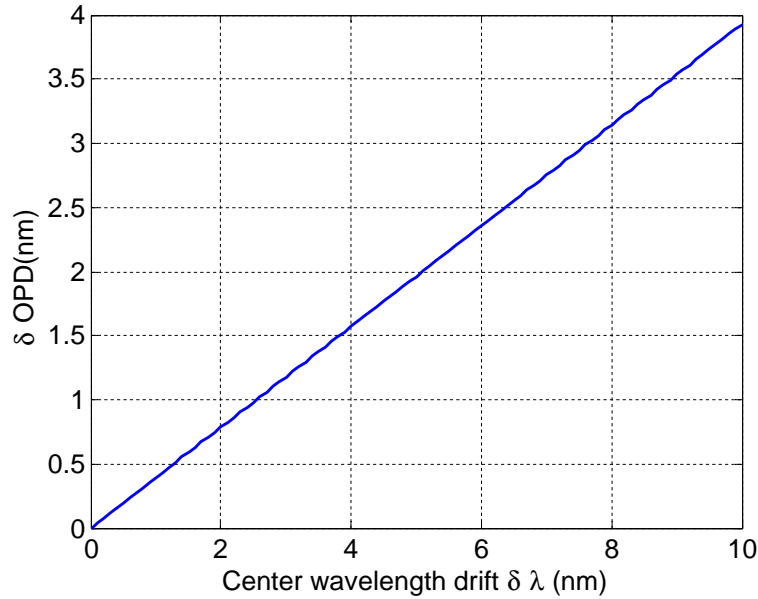


Figure 4.5. OPD measurement uncertainties caused by center wavelength shift ($\delta\lambda$) ($\gamma=1$, $\lambda_p=857\text{nm}$, $L=30\mu\text{m}$, $w=60\text{nm}$)

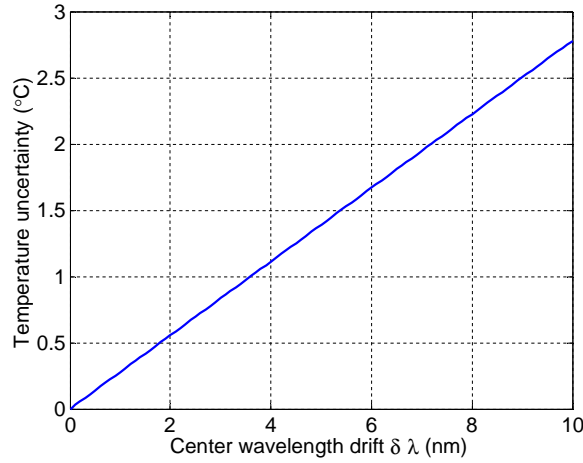


Figure 4.6. Temperature uncertainty caused by center wavelength shift ($\delta\lambda$) ($\gamma=1$, $\lambda_p=857\text{nm}$, $L=30\mu\text{m}$, $w=60\text{nm}$)

4.1.2 Spectral bandwidth broadening/narrowing effects

According to the Gaussian curve approximation of the output spectrum of the LED, shown in Equation (2.3), spectral bandwidth is another factor that can induce errors in the temperature measurements. To see the effect of the spectral bandwidth changes on the temperature measurements qualitatively, assuming that the center wavelength is fixed, a first-order approximation is used to analyze the normalized spectral curves. The spectrum curve with bandwidth change δw relative to the original bandwidth w can be described as:

$$I_w(\lambda) = I_0 \exp\left(-\frac{(\lambda - \lambda_0)^2}{(w + \delta w)^2}\right) \quad (4.14)$$

The normalized interference fringes will then be:

$$N_w(\lambda) = \frac{I_w(\lambda)}{I(\lambda)} = \frac{\exp\left(-\frac{(\lambda - \lambda_0)^2}{(w + \delta w)^2}\right)}{\exp\left(-\frac{(\lambda - \lambda_0)^2}{w^2}\right)} \left(1 + \gamma \cos\left(\frac{2\pi L}{\lambda}\right)\right) \quad (4.15)$$

Assuming that $|\delta w/\lambda_0| \ll 1$, yields a first order approximation:

$$\frac{\exp\left(-\frac{(\lambda - \lambda_0)^2}{(w + \delta w)^2}\right)}{\exp\left(-\frac{(\lambda - \lambda_0)^2}{w^2}\right)} \approx \left(1 + \frac{2(\lambda - \lambda_0)^2}{w^3} \delta w\right) \quad (4.16)$$

So the normalized Equation (4.15) becomes:

$$N_w(\lambda) = \frac{I_w(\lambda)}{I(\lambda)} = \left(1 + \frac{2(\lambda - \lambda_0)^2}{w^3} \delta_w\right) \times \left(1 + \gamma \cos\left(\frac{2\pi L}{\lambda}\right)\right) \quad (4.17)$$

The shifted peak position λ_p' can be acquired by differentiating Equation (4.17) and setting it equal to zero. Doing so gives,

$$\begin{aligned} \frac{\partial N_w}{\partial \lambda} \Big|_{\lambda=\lambda_p'} &= \frac{4(\lambda - \lambda_0)\delta_w}{w^3} + \frac{2\pi L \gamma}{\lambda_p'^2} \sin\left(\frac{2\pi L}{\lambda_p'}\right) + \frac{2(\lambda - \lambda_0)\delta_w}{w^3} \gamma \cos\left(\frac{2\pi L}{\lambda_p'}\right) \\ &+ \frac{4(\lambda - \lambda_0)\delta_w \gamma}{w^3} \times \frac{2\pi L}{\lambda_p'^2} \times \sin\left(\frac{2\pi L}{\lambda_p'}\right) = 0 \end{aligned} \quad (4.18)$$

Assuming that $\delta_w \ll w$, and noting that in regions around the peaks in the interference fringes:

$$\begin{aligned} \cos\left(\frac{2\pi L}{\lambda_p'}\right) &\approx 1 \\ \sin\left(\frac{2\pi L}{\lambda_p'}\right) &\approx \sin\left(\frac{2\pi L(\lambda_p - \Delta\lambda)}{\lambda_p^2}\right) = \sin\left(2k\pi - \frac{2\pi L \Delta\lambda}{\lambda_p^2}\right) \approx -\frac{2\pi L \Delta\lambda}{\lambda_p^2} \end{aligned} \quad (4.19)$$

then substituting these two equations back into (4.18), and further considering that $\delta_w/w \ll 1$, and $\Delta\lambda/\lambda_p \ll 1$, yields the following first order approximation,

$$\lambda_{p-w}' = \frac{(1 + \gamma)\lambda_p^4}{2\pi^2 \gamma L^2 w^3} \delta_w + \lambda_p \quad (4.20)$$

Using Equation (3.11), the OPD demodulated from the shifted peak wavelength λ_{p-w}' will be:

$$L_{\lambda-w}^p = m \lambda_{p-w}' = \frac{\lambda_{p-w}'}{\lambda_p} L \quad (4.21)$$

From Equation (4.20) and Equation (4.21), we obtain:

$$L_{\lambda-w}^p = L + \frac{(1+\gamma)\lambda_p^3}{2\pi^2\gamma L w^3} \delta w \quad (4.22)$$

This equation can be used to estimate the OPD measurement errors caused by the spectrum bandwidth changes as shown in Figure 4.7; Figure 4.8 shows the temperature measurement uncertainty caused by the spectrum bandwidth changes.

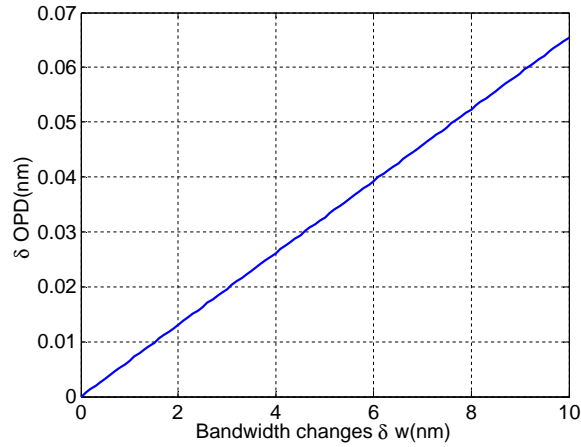


Figure 4.7. OPD measurement uncertainties caused by the bandwidth changes (δw) ($\gamma=1$, $\lambda_p=857\text{nm}$, $L=30\mu\text{m}$, $w=60\text{nm}$)

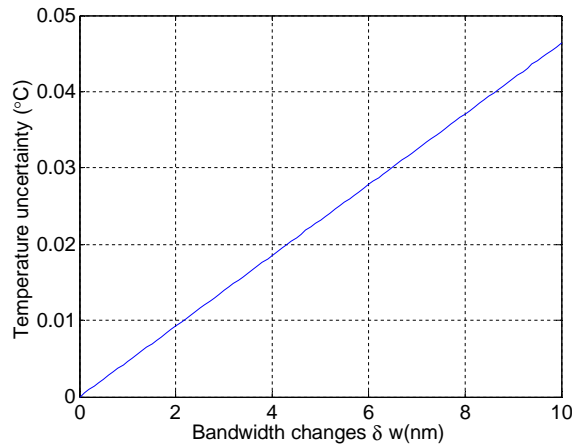


Figure 4.8. Temperature uncertainty caused by the bandwidth changes (δw) ($\gamma=1$, $\lambda_p=857\text{nm}$, $L=30\mu\text{m}$, $w=60\text{nm}$)

4.2 Degradation effect due to the visibility of the interference spectrum

The visibility of the interference spectrum may be influenced by the optical polarizer extinction ratio, the optical alignment between the polarizer and the sensing element, and the collimation quality of the optical collimator. Among these factors, for the given

qualities of the polarizer and the optical collimator, the influence from the optical alignment between the optical polarizer and the sensing element is dominant. The optical alignment changes are also unavoidable in industrial fields where the mechanical vibration problem is severe. The following analysis is using the optical misalignment caused visibility changes to evaluate the temperature measurement uncertainty. The sensing element is intentionally rotated relative to the polarizer within a plane normal to the light propagation direction, as shown in Figure 4.9, so that the visibilities are changed.

The results shown in Equation (2.9) assume that the polarization direction P of the input light beam is at 45° relative to the fast- and slow-axes of the sensing element in the plane normal to the light propagation direction. In fact, it is very difficult to align all optical components accurately in the sensor probe. Also, mechanical vibrations may cause changes of the relative positions between the sensing element and the polarizer. Thus, it is necessary to analyze the dependence of the temperature measurement uncertainties on the angle α .

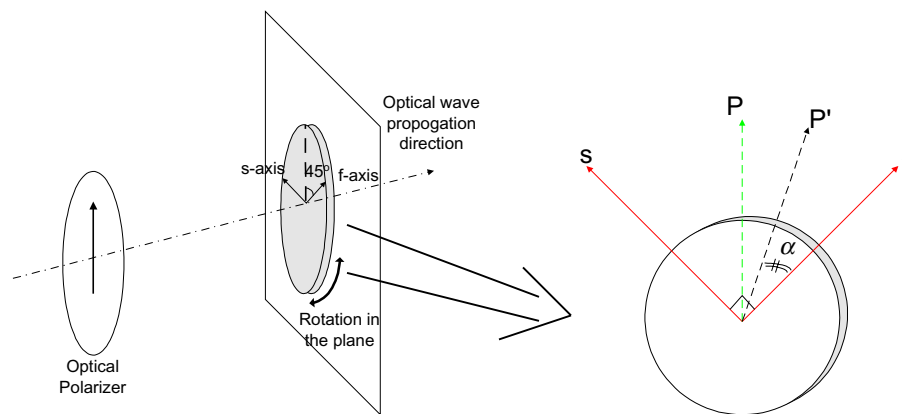


Figure.4.9. Misalignment between the optical polarizer and the sensing element.

When a linearly polarized light beam passes through the sapphire sensing element, the light behaves as if it is divided along the fast- and slow-axis separately as shown in Figure 4.10. The refractive index is n_e along the f-axis, and n_o along the s-axis. At the input surface of the sapphire sensing element, the ordinary wave and the extraordinary

wave are still in phase, namely the phase difference is $\delta=0$. After light passes through the sensing element, the phase difference δ will be changed to

$$\delta = 2\pi d\Delta n / \lambda \tag{4.23}$$

where d is the thickness of the sensing element, $\Delta n = n_o - n_e$ is the birefringence of the single crystal sapphire material, and λ is the optical wavelength. Depending on the magnitude of the δ value, as well as the alignment angle α between the linear polarization direction of the input light and the principal axes in the sensing element, the output light from the sensing element can be linearly polarized, circularly polarized or elliptically polarized.

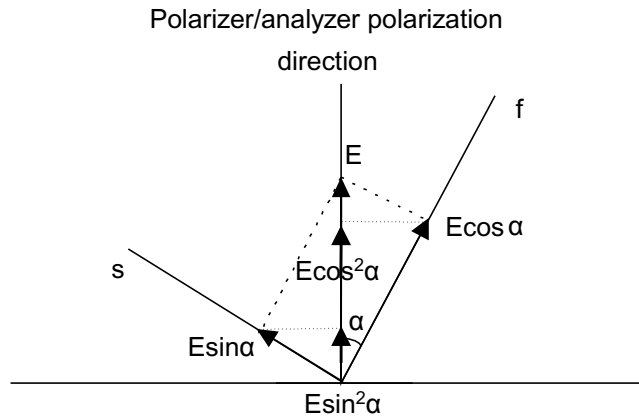


Figure 4.10. Decomposition and interference of the linearly polarized input light in the polarimeter.

If another polarization analyzer is placed behind the sensing element with its polarization direction parallel to the linear polarization direction of the input light, the electric field of the output optical wave can be expressed in a vector form as

$$\vec{E}_{out} = \vec{E}_0 \sin^2 \alpha + \vec{E}_0 \cos^2 \alpha \tag{4.24}$$

where \vec{E}_{out} , $\vec{E}_0 \sin^2 \alpha$ and $\vec{E}_0 \cos^2 \alpha$ are all vectors. The intensity of the output light will be:

$$I_{out} = |\vec{E}_{out}|^2 \tag{4.25}$$

The interference results will contain the information about the phase delay δ between the two linearly polarized beams in the sensing element, as well as the angle α :

$$\begin{aligned}
 I_{out} &= (E_0 \sin^2 \alpha)^2 + (E_0 \cos^2 \alpha)^2 + 2E_0^2 \left(\frac{\sin 2\alpha}{2}\right)^2 \cos \delta \\
 &= E_0^2 \left[1 + \frac{1}{2} \sin^2 2\alpha \times (\cos \delta - 1)\right] \\
 &= I_0 \left(1 + \sin^2 2\alpha \times \sin^2 \frac{\delta}{2}\right)
 \end{aligned}
 \tag{4.26}$$

From Equation (4.23), δ is a function of the product $d\Delta n$. When the temperature changes, the thickness d of the sapphire sensing element will change, as well as the birefringence $\Delta n = n_o - n_e$. Equation (4.26) is thus essentially a function of temperature.

The factor related to the angle α in Equation (4.26) will determine the visibility of the interferogram of the two polarized beams. After normalization of the measured spectral curve $I(\lambda)$ with the intensity $I_0(\lambda)$ of the input broadband optical source, the visibility of the interferogram will be

$$\gamma = \sin^2 2\alpha .
 \tag{4.27}$$

The dependence of the visibility on the angle α is plotted in Figure 4.11.

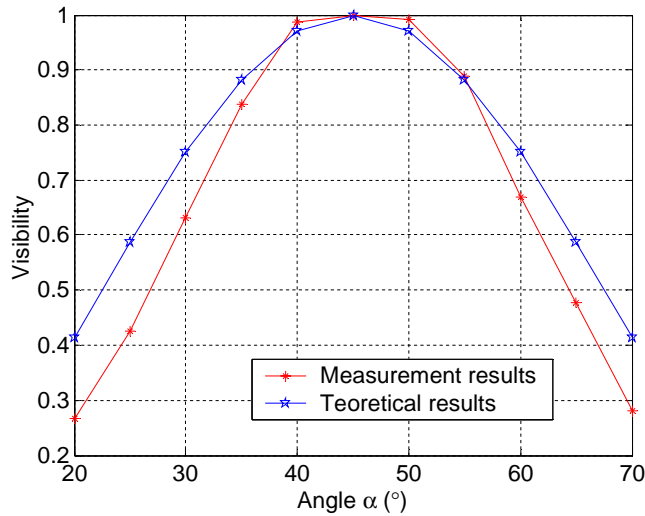


Figure 4.11. Visibilities dependence on the misalignment angle α between the light polarization direction and principal axes of the sensing element.

By changing the angle α , the measured optical spectra with different visibilities are plotted in Figure 4.12. The maximum and minimum intensities in these spectral curves,

corresponding to the peaks and valleys in the curves, are fixed. Since only these peaks and valleys are used to extract the temperature information, accurate temperature measurement results can thus still be obtained in a wide changing range of the visibilities. Experimental results demonstrate that the temperature can be measured accurately with the change of the angle α up to 10° , as shown in Figure 4.13. This tolerance of the angle α can be easily met in the laboratory environment as well as in the industrial environments, where mechanical vibration condition is usually severe.

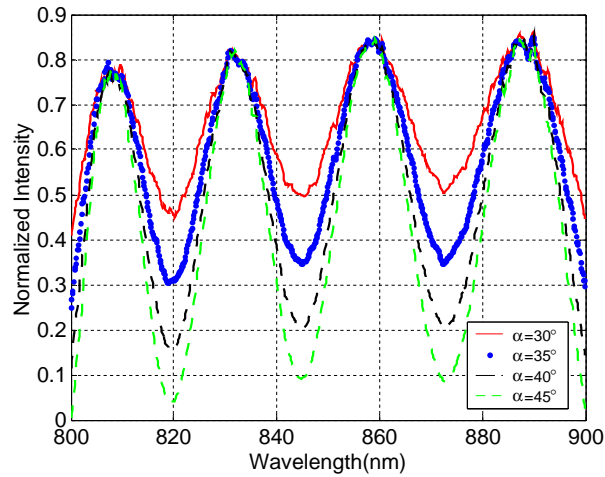


Figure 4.12. Experimental interferograms with different visibilities.

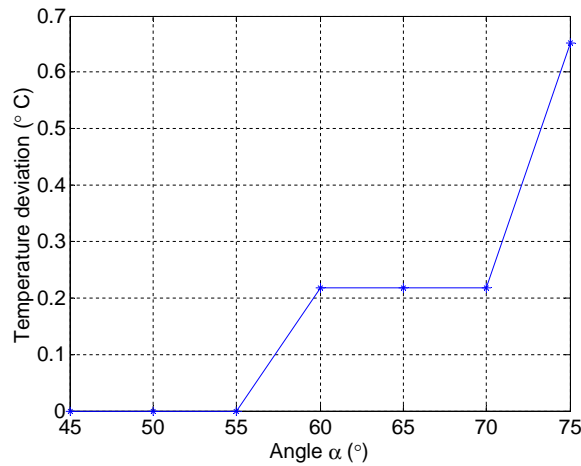


Figure 4.13. Measured temperature deviation caused by the changes in the visibility of the interferogram

4.3 Optical birefringence effects

As presented in Chapter 2, the BPDI technology measures the optical path difference

(OPD), or the phase retardation between the two orthogonal linearly polarized light beams in a single crystal sapphire element, which is a function of both the temperature dependent birefringence and the temperature dependent thickness. The retardation in the sensing element is a refractive index effect. It is known that as light passes from the vacuum into a material, the speed of light is reduced by a factor that is the reciprocal of the refractive index. An anisotropic material is completely characterized by three principal refractive indices, which can be represented by an index ellipsoid. In uniaxial materials, one principal refractive index is different from the other two. The rays that are used to define the unique (optic) axis are called ordinary rays and the refractive index is n_o . Those that are associated with the other axes are called extraordinary rays and the refractive index is n_e . Materials with different principal refractive indices are therefore referred to as birefringent.

The magnitude of the birefringence in an anisotropic material depends on the propagation direction of the optical wave in the material. As shown in Figure 4.14, the index ellipsoid is used to determine the magnitude of the two indices of the refraction (n_o and n_e corresponding to D_1 and D_2) for the two orthogonal linearly polarized waves in the material. This is done by finding the intersection ellipse between a plane through the center of the ellipsoid that is normal to the direction of light propagation. The axes of the intersection ellipse are equal in length to $2n_o$ and $2n_e$, where n_o and n_e are the indices of refraction corresponding to the two orthogonal linearly polarized light waves. The two waves are polarized in directions parallel to D_1 and D_2 .

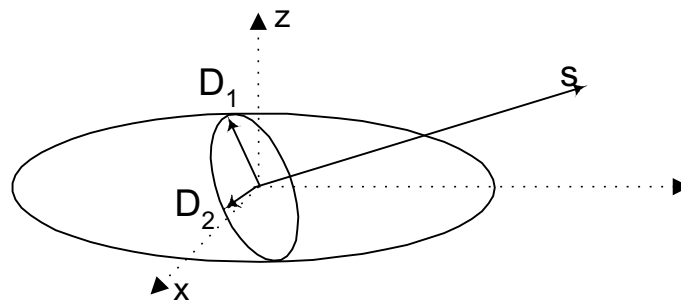


Figure 4.14. Method of the index ellipsoid to determine the refractive indices of light propagating along s direction.

Single crystal sapphire is a uniaxial crystal because of its hexagonal crystalline structure, as shown in Figure 3.2. The index ellipsoid corresponding to the hexagonal inner atomic structure is shown in Figure 4.15. The refractive index along the C-axis is n_o , the refractive index along the A-axis is n_e . Single crystal sapphire is a negative uniaxial crystal, meaning $n_o > n_e$; thus the C-axis is the slow axis and the A-axis is the fast axis. In the single crystal sapphire, the refractive index is constant in the x-y plane, there is no birefringence in this plane and is called the C-plane. In the y-z or x-z plane, the refractive indices along different axes are different; birefringence $\Delta n = n_o - n_e$ exists, and called the A-plane. With the propagation direction of the incident light wave perpendicular to the sapphire sensing disk surface (A-plane), the phase delay between the two orthogonal linearly polarized waves will be $\delta = 2\pi d \Delta n / \lambda$, where d and Δn are the only terms that are functions of temperature. Therefore temperature can be measured directly by monitoring the phase delay δ with the BPDI technology. For the case of non-normal incident light, the birefringence $\Delta n = n_o - n_e$ will be incident angle dependent, as well as the optical path length that the light passes through in the sapphire sensing element, thus a more general formula for the phase delay calculation should be:

$$\delta(T, \theta) = \frac{2\pi d(T, \theta) \Delta n(T, \theta)}{\lambda} \tag{4.28}$$

where T is the temperature, and θ is the light incident angle.

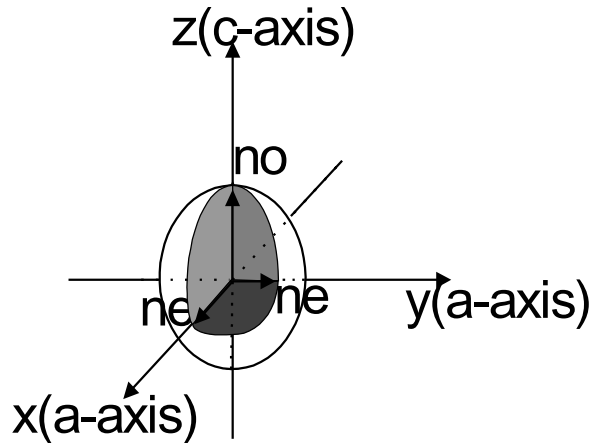


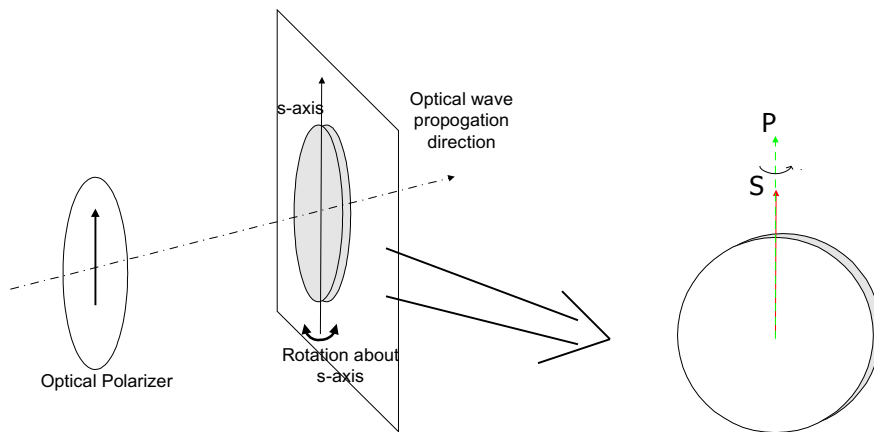
Figure 4.15. The refractive index ellipsoid for single crystal sapphire.

To analyze the temperature measurement uncertainty caused by the non-normal incident light on the sapphire sensing element, the sensing element is rotated about its fast axis,

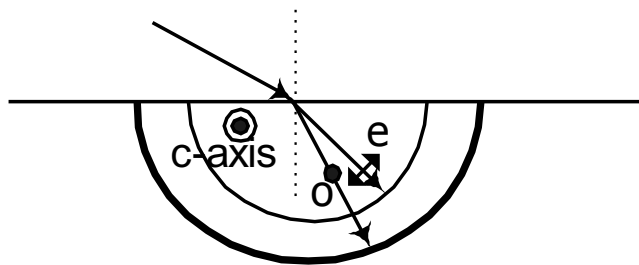
slow axis and an axis 45° from the slow/fast axis respectively to study their effects on the OPD measurement results.

4.3.1 Rotation about the slow-axis (i.e. C-axis)

The rotation is shown in Figure 4.16 (a). In this case, the refractive indices for the ordinary and extraordinary waves are all constant, shown in Figure 4.16(b), thus the birefringence $\Delta n = n_o - n_e$ is independent of the light incident angle. For this situation, the optical path L , along which light passes through the sapphire disk, is the only factor that is incident angle dependent.



(a) Rotation about the s-axis of the sensing element



(b) Wave vectors for the double refraction in the sapphire, with the optical axis parallel to the boundary and perpendicular to the plane of the incidence.

Figure 4.16. Optical refractive index ellipse for the rotation about the s-axis of the sensing element

In the room temperature environment, the refractive indices of the single crystal sapphire can be approximated by Equation (3.1), as plotted in Figure 4.17(a). The birefringence $\Delta n = n_o - n_e$ is plotted in Figure 4.17(b) as a function of the optical wavelengths.

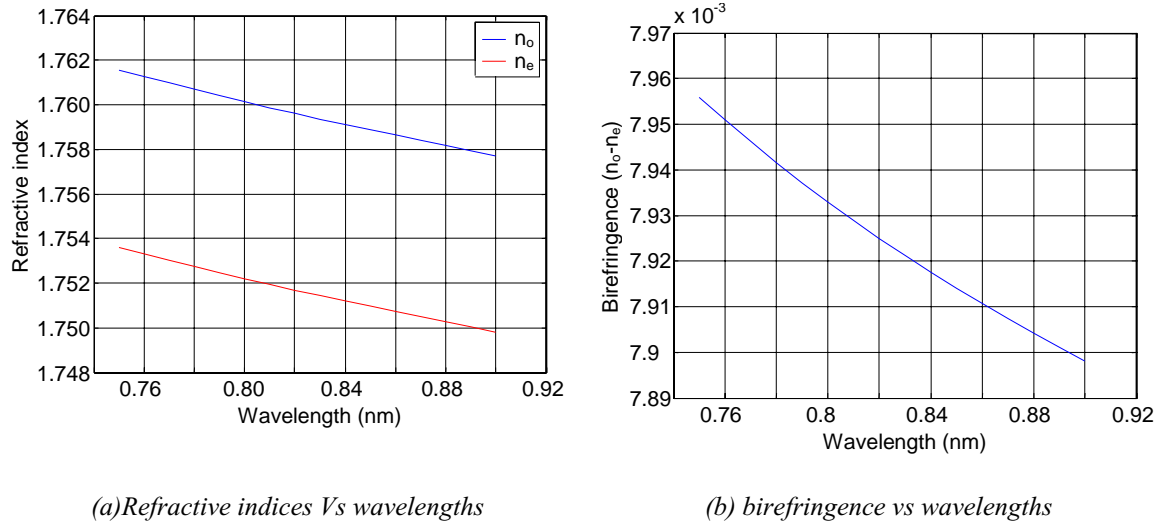


Figure 4.17. Refractive indices and birefringence vs. optical wavelength for sapphire.

Selecting the refractive indices at the wavelength of interest $\lambda=850\text{nm}$, $n_e=1.751$ and $n_o=1.7589$, the refraction angles vs. incident angles for the ordinary and extraordinary waves are plotted in Figure 4.18(a). The difference between the two angles is so small as shown in Figure 4.18(b), that they can be treated as equal in analyzing the rotation effects on the temperature measurements. As shown in Figure 4.19(a), the OPD change is only related to the change in L as a result of the disk rotation. The OPD values are:

$$\begin{aligned} OPD &= (n_o - n_e)L; && \text{(normal incident light)} \\ OPD' &= (n_o - n_e)L / \cos\theta_1 && \text{(the sensing disk rotated an angle } \theta_0) \end{aligned} \quad (4.29)$$

where θ_1 is the light refraction angle corresponding to the light with an incident angle θ_0 . Changes of the OPDs vs. rotation angles (θ_0) up to 50° have been measured, and the results are compared with theoretical simulations as shown in Figure 4.20.

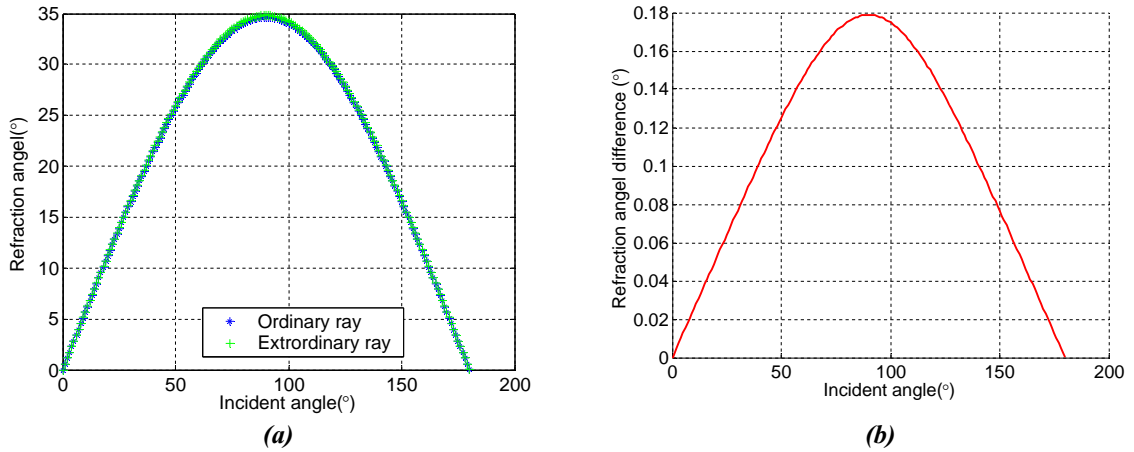


Figure 4.18. (a) Refraction angles of the ordinary waves and the extraordinary waves (rotation about the s-axis).

(b) The refraction angle difference between the ordinary waves and the extraordinary waves (rotation about the s-axis)

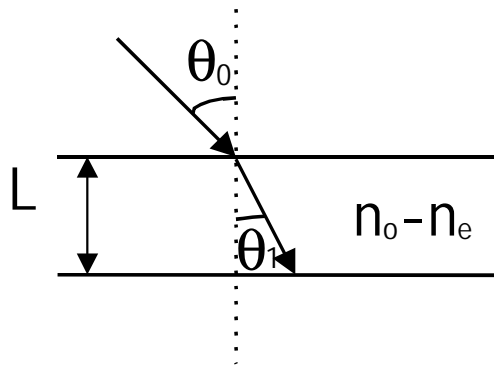


Figure.4.19. Sensing element rotation effect on the optical path difference (OPD) (rotation about the s-axis).

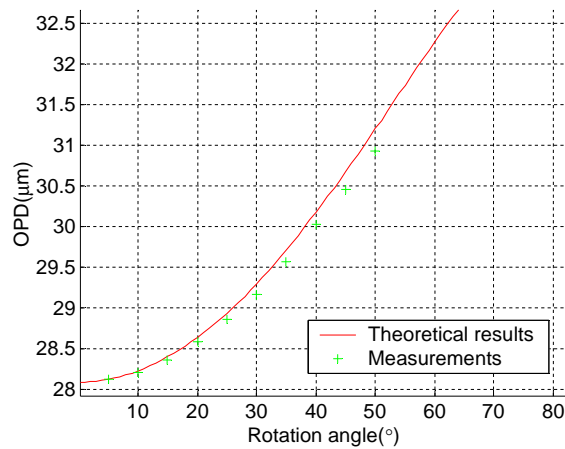


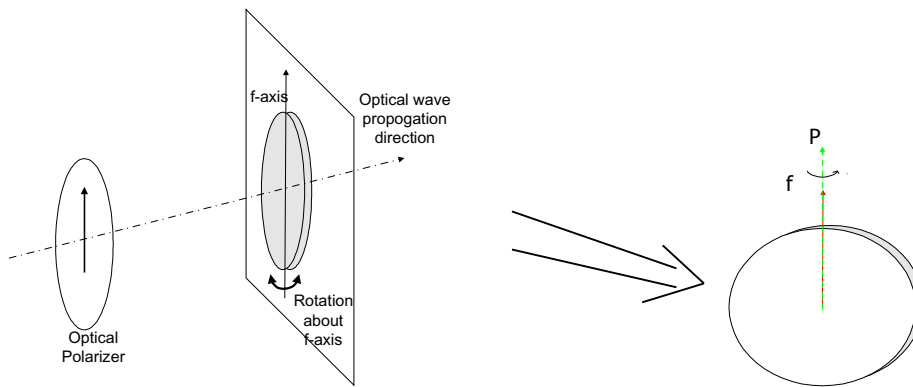
Figure4.20. Sensing element rotation effects along s-axis on the OPD measurements.

In both the theoretical analysis and experimental measurements, it was shown that the OPD values increase with the increasing of the rotation angles about the C-axis. In a constant temperature environment, if the sensing element rotates, the OPD values change rather than remain constant. This change in the OPD values will thus affect the accuracy of the temperature measurements. Using the OPD vs. rotation angle curves shown in Figure 4.20, the rotation effects on the temperature measurements can be estimated according to the calibrated relationship between the OPDs and the temperatures. It is shown that the temperature measurement uncertainty is less than 4°C for rotation angles up to 5°.

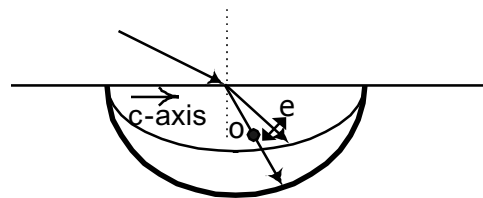
4.3.2 Rotation about the fast-axis (i.e. A-axis)

The rotation is shown in Figure 4.21 (a). In this case, the refractive index for the ordinary light wave is independent of the incident angles, and it obeys Snell’s law:

$$n_i \sin \theta_0 = n_o \sin \theta_1 \tag{4.30}$$



(a) Rotation about the s-axis of the sensing element



(b) Wave vectors for the double refraction in the sapphire, with the optic axis parallel to the boundary and perpendicular to the plane of incidence.

Figure 4.21. Optical refractive index ellipse for the rotation about the f-axis of the sensing element.

where n_i is the refractive index of the media from which the light is incident, and θ_0 and θ_i are the incident angle and refraction angle of the light, respectively.

For the extraordinary waves in the A-plane sapphire disk, the corresponding refractive index depends on the direction of light propagation. With rigorous mathematical analysis shown in Appendix I, the refraction angle θ_2 and refractive index n_e can be expressed as,

$$\theta_2 = \tan^{-1}\left(\sqrt{\frac{n_o^2 n^2 \sin^2 \theta_0}{n_{eo}^2 (n_o^2 - n^2 \sin^2 \theta_0)}}\right)$$

$$n_e = \frac{n_{eo}^2 n_o^2 (1 + \tan^2(\theta_2))}{n_{eo}^2 \tan^2(\theta_2) + n_o^2}$$
(4.31)

where n is the refractive index of the media from which the light is incident ($n=1$ for the incident light from the air); n_{eo} is a special n_e value, which is the refractive index of the extraordinary waves normal incident to the surface of the A-plane sapphire disk. Refractive indices for the extraordinary waves increase as the refraction angles increase, as shown in Figure 4.22.

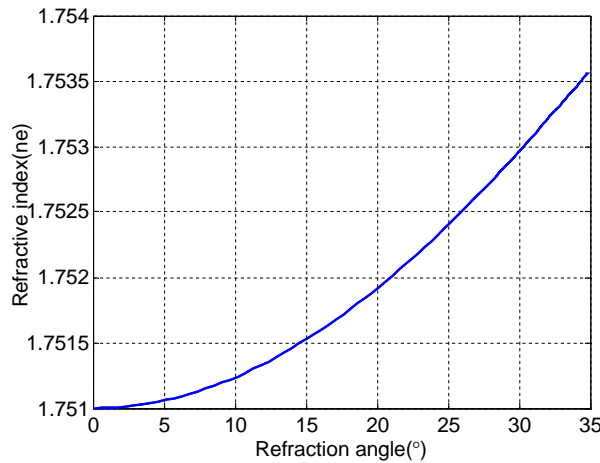


Figure 4.22. Refractive indices vs. light incident angles for the extraordinary waves.

Using the refractive index for the wavelength of interest, $\lambda=850nm$ ($n_{eo}=1.751$, $n_o=1.7589$), the refraction angles for the ordinary wave and the extraordinary wave are plotted in Figure 4.23(a). The difference between the two angles is so small, as shown in Figure 4.23(b), that the refraction angles in the sapphire disk for these two waves can be approximated as equal for the analysis of the rotation effects on the temperature

measurements. The changes in the OPDs are related to the L changes as a result of the disk rotation, as well as the changes in the refractive indices for the extraordinary wave, as shown in Figure 4.24.

$$\begin{aligned}
 d &= (n_o - n_e)L; \\
 d' &= (n_o - n_e)(\theta_2)L / \cos\theta_2
 \end{aligned}
 \tag{4.32}$$

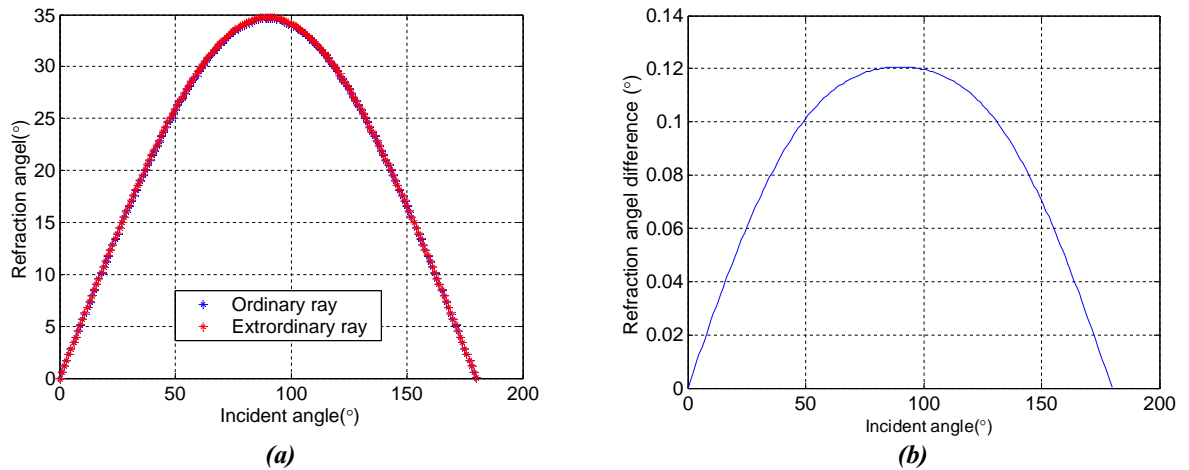


Figure 4.23. (a) Refraction angles of the ordinary waves and the extraordinary waves (rotation about the f -axis)
 (b) The refraction angle difference between the ordinary waves and the extraordinary waves (rotation about the f -axis)

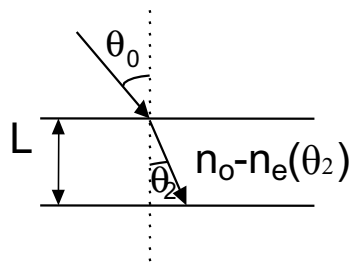


Figure 4.24. Rotation effects on the optical path difference (rotation about the f -axis)

The changes in the OPDs vs. rotation angles up to 50° have been measured; the results are compared with the theoretical simulations in Figure 4.25.

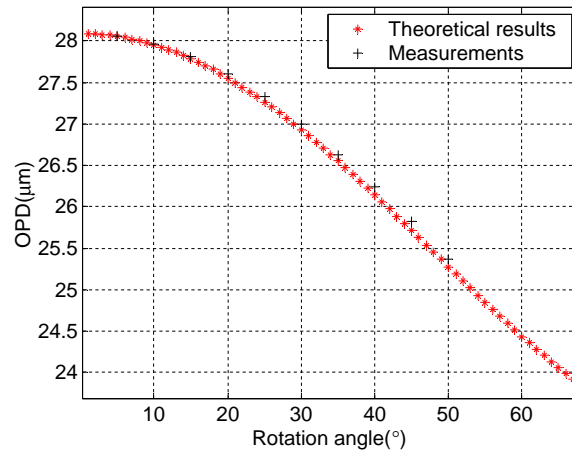


Figure 4.25. Effect of rotation about the f-axis on the OPD measurements.

According to the theoretical analysis and experimental measurements, the OPD values decrease when the sensing element rotates about its A-axis. By comparing curves shown in Figure 4.20 and Figure 4.25, it is evident that the magnitude of the OPD changes are smaller when the rotation is about the A-axis instead of the rotation about the C-axis for a given rotation angle. These results can be explained as following: when the sensing element rotates about the A-axis and the light incident angles increase, the L' value increases from the initial value L , the birefringence decreases from the initial value $\Delta n = n_{e0} - n_o$, and the combined effects cause the OPDs to decrease; when the rotation is about the C-axis, OPDs increase because the L' value increases from the initial value L , and the birefringence is fixed constant at its initial value $\Delta n = n_{e0} - n_o$, the changing magnitude is then larger than the OPD changes corresponding to the same angle rotation about the A-axis.

With the relationship between the OPDs and rotation angles shown in Figure 4.25, we can estimate that the temperature measurement uncertainty is less than 3°C for rotation angles up to 5° about the fast axis, based on the calibrated relationship between the OPDs and the temperature values.

4.3.3 Rotation about an axis 45° from the slow-axis/fast-axis

According to the analytical and experimental results presented in the two previous

sections, it is expected that the dependence of OPD values on rotation angles will be reduced if the rotation occurs about an axis between the slow axis and fast axis. The total rotation effect on temperature measurements can thus be partially cancelled between the increasing and decreasing values of OPDs. We tested the rotation of the sensing element about the z-axis, shown in Figure 4.26. The direction of the z-axis is at 45° relative to both the slow axis and the fast axis of the sensing element. This rotation can be treated as partial rotation about the fast axis, which will cause the OPDs to decrease, and partial rotation about the slow axis, which will cause the OPDs to increase. Experimental results are shown in Figure 4.27. With a rotation angle less than 5°, the effect on the temperature measurement uncertainty is less than 2°C.

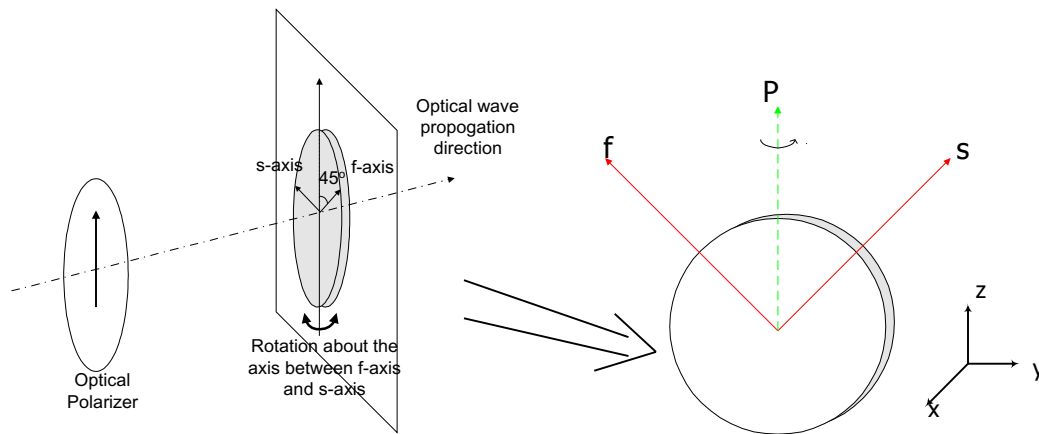


Figure 4.26. Rotation about an 45° from the s-axis/f-axis of the sensing element.

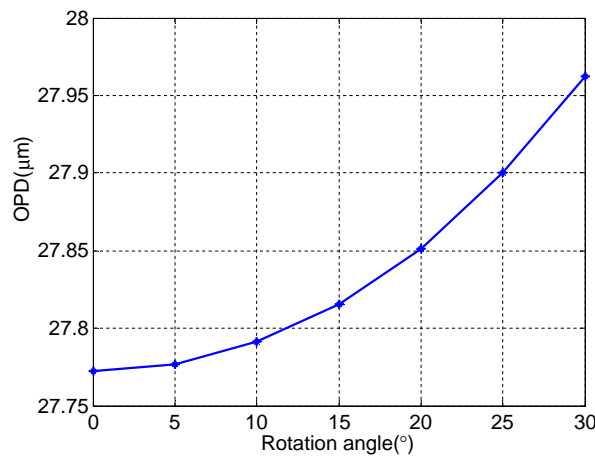


Figure.4.27. Effect on the OPD measurements of rotation about an axis 45° from the f-axis of the sensing element.

4.4 Opto-electronic noise in spectrum measurements

The opto-electronic noise in this system is generated inside the optical spectrometer, where dispersed light from the grating is scanned electronically by a 2048-element linear silicon CCD array and converted into electric signals, then processed in the computer, as shown in Figure 4.28. The CCD detecting system is a solid-state sensor consisting of a wafer of silicon crystal, and has 2048 photodiode-capacitor pairs. Radiation coming from the optical grating hits the photodiodes, causing the capacitors to discharge. These capacitors contain charges proportional to the photon flux. At the end of the integration period, a series of switches close and transfer the charge to a shift register. The charges on the shift register are digitized and the values are amplified and sent to the computer, which plots an optical spectrum. The noises associated with the CCD array are mainly readout noise and dark current noise.

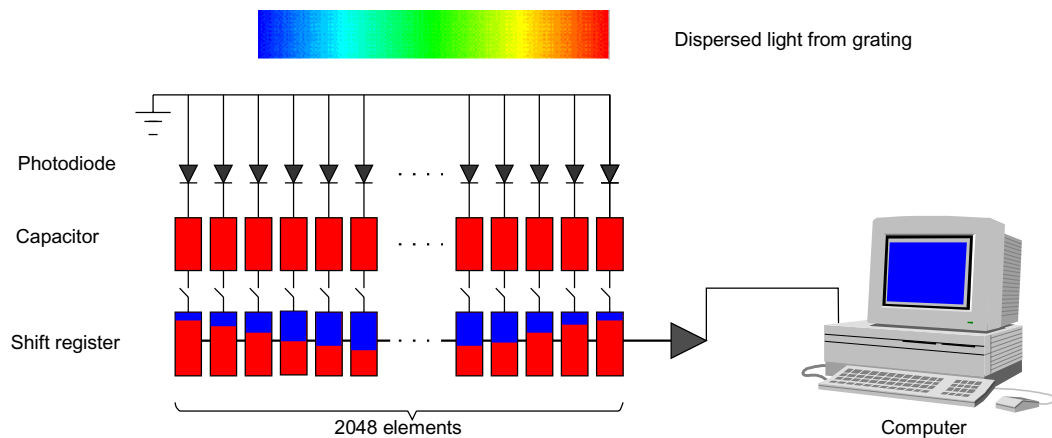


Figure 4.28. CCD detecting array for the optical signal detection in the optical spectrometer

Readout noise:

The readout noise of the CCD detector is a combination of thermal white noise, $1/f$ noise from its electrical components, i.e. photodiodes, capacitors, shift registers and the on-chip amplifier. The white noise and the $1/f$ noise depend on the on-chip amplifier size of the CCD detector, and become lower when the amplifier sizes increase. But, as the amplifier size grows, its input capacitance from the sensing pixels (each pixel is composed of one photodiode, one capacitor and one shift register), also grows, lowering the sensitivities of

the sensing pixels and increasing the readout noise. With an optimum design, typical readout noise is 4-5 electrons for the current commercial products.

Dark current noise:

The CCD array liberates electrons in the photodiode to generate electric signals. The amount of electrons generated by each CCD pixel depends on the photo flux. This process is extremely temperature dependent. Even without optical illumination, electrons can also be generated by the finite temperature of the CCD. The thermally generated electrons are called the dark current. The dark current noises can be minimized by cooling the CCD detector.

The goal of the measurement of the optical spectrum electronically is the unambiguous determination of the OPDs between the two orthogonal linearly polarized light waves, which can be calculated by Equation (3.14) with the known spectral positions of the peaks and valleys in the interference spectral curves. The opto-electronic noise in the CCD detector affects the accurate determination of the peak and valley positions in the interference spectral curves. Since the ideal measured signal intensities corresponding to the valley positions are zero, the SNR at those points are thus very small and affected by the noise more seriously than the peaks points. To be conservative, we analyze the opto-electronic noise effects on temperature measurements by considering the valley points with noises. By differentiating Equation (2.4), the noise amplitude δI , or the signal uncertainty, is related to the uncertainty of the valley positions $\delta\lambda$:

$$\begin{aligned} \delta I &= I_s(\lambda)\gamma \frac{2\pi L \delta\lambda}{\lambda^2} \sin\left(\frac{2\pi L}{\lambda}\right) \\ \sin\left(\frac{2\pi L}{\lambda}\right) &= 1, \text{ for the valleys,} \end{aligned} \tag{4.33}$$

where L is the OPD value, λ is the optical wavelength, $I_s(\lambda)$ is the optical signal, and γ is the visibility of the interference spectral curves. This equation can be transformed into:

$$\left. \begin{aligned} \delta\lambda &= \frac{\lambda^2}{2\pi\gamma L(I_s(\lambda)/\delta I)} \\ SNR &= (I_s(\lambda)/\delta I)^2 \end{aligned} \right\} \Rightarrow \delta\lambda = \frac{\lambda^2}{2\pi\gamma L \sqrt{SNR}} \tag{4.34}$$

Also according to Equation (2.14), the measurement uncertainty of the valley position will affect the OPD calculation by the following relation:

$$OPD = f(T) = \frac{\lambda_1 \lambda_2}{\lambda_1 - \lambda_2} \tag{4.35_a}$$

$$\delta f = \left[\left(\frac{\partial f}{\partial \lambda_1} \delta \lambda_1 \right)^2 + \left(\frac{\partial f}{\partial \lambda_2} \delta \lambda_2 \right)^2 \right]^{1/2} \tag{4.35_b}$$

The CCD array used in the optical spectrometer is Sony® ILX511 linear CCD array, with a SNR of 250. Assuming $\gamma=1$, then the uncertainties of both OPD measurement and temperature measurement are OPD value dependent. Combing Equation (4.34), Equation (4.35_a) and Equation(4.35_b), where $L=f(T)$, the OPD measurement uncertainties are calculated and plotted in Figure 4.29. Based on the calibration curve between OPD and temperature, Figure 4.30 shows the temperature measurement uncertainty related to the results shown in Figure 4.29. We can see that the opto-electronic noise contributes significantly to the measurement uncertainties of temperature. With the OPD increase, the temperature measurement uncertainties increase. To control the opto-electronic noise effect on temperature measurements, the OPD values should be selected properly for temperature measurement over a wide dynamic range. To increase the SNR of the spectrum measurement, there is another effective way to minimize the opto-electronic noise, and will be discussed in section 4.6.

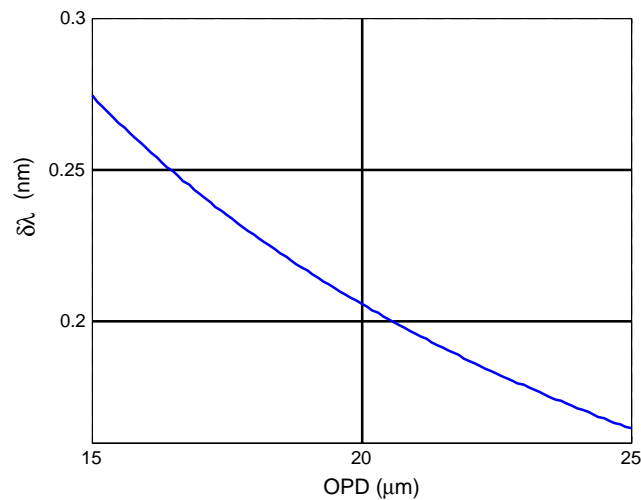


Figure 4.29. Opto-electronic noise effects on the valley point locations determinations

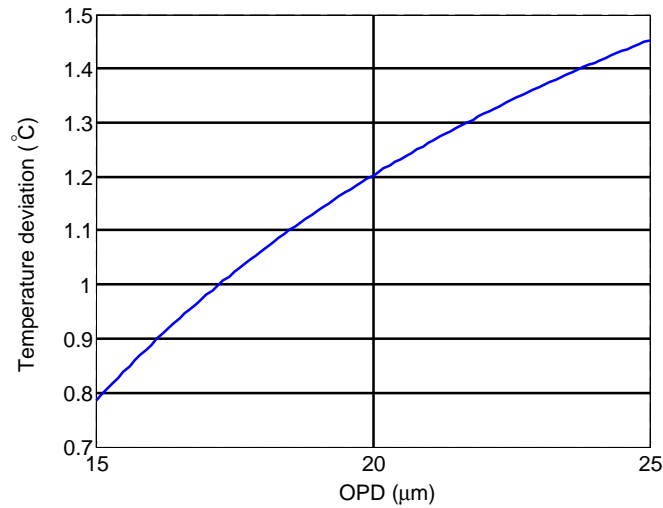


Figure 4.30. Opto-electronic noise effects on the temperature measurement uncertainties

4.5 Optical fiber induced noises

Optical fiber is used in the BPDI sensor system to guide light into the sensing probe, recollect light reflected from the end of the sensing probe, and then guide the optical temperature signature into the spectrometer for signal processing. Because of its small size, immunity to EMI and chemical corrosion resistance, optical fiber offers great system deployability in harsh environments. At the same time the optical polarization effects, optical dispersion, fiber bending-induced transmission spectrum drift in the optical fiber might induce noises in the temperature measurement (signal distortion is viewed as noise in this discussion).

Since the sensing scheme for the BPDI sensor system is based on polarimetric interferometry, the state of polarization of the light is very important for the sensor to perform accurate temperature measurements. The temperature information is encoded into the polarization states and the spectrum of light inside the sensing element, the output temperature signature from the sensing probe is a linearly polarized light. When coupled back into the multimode optical fiber, its polarization state usually becomes random, and the light waves with different polarization states still contain the same spectrum information, thus the same temperature information. The polarization mode

dispersion (PMD) may be a concern in single mode fibers for long haul transmission. However for multimode fiber, it is not a problem for a few kilometer transmission distances. Multi-mode optical fiber increases the energy coupling efficiency between the LED source and the optical fiber; collimation of light is also easier for multimode fiber with larger numerical aperture compared to single mode optical fibers.

The optical fiber dispersion in a multimode fiber includes inter-modal dispersion and chromatic dispersion. Chromatic dispersion occurs because different colors of light travel through the fiber at different speeds; inter-modal dispersion is also called multipath dispersion, where different rays or modes in the multimode fiber travel along paths of different lengths. The inter-modal dispersion is dominant in multimode fibers. Graded-index multimode fibers used in the system have less inter-modal dispersion compared to step-index multimode fibers with the same geometrical structure and numerical aperture. A graded index multimode fiber with optimized index profile has a capacity of 100Mb/s over a distance of up to 100km [68]. Experiments with a 3km long multimode fiber in the BPDI sensor system revealed no obvious degradation effects on the optical pulse signals with a repetition rate of 8Hz.

When light propagates inside the fiber, the spectrum may be distorted because of fiber bending, so the center wavelength and the bandwidth of the transmission light may be changed. Compared to the optical source spectrum distortion caused by the environmental temperature fluctuations, this effect in the fiber is much small, and was not observed in the BPDI sensor system.

4.6 Summary of system noises and their optimization

A summary is listed in Table 4.1 for system noises and their degradation effects on temperature measurements. The design of the system, including the software and the hardware, is optimized based on systematic analyses of these noises.

Table 4.1. Noise in the BPDI sensor system and compensation methods

Noise type		Noise source	Temperature measurement uncertainty
Electrical noise	1). Dark current 2). Thermal white noise 3). 1/f noise	CCD detector in the spectrometer	2°C (0.063% full measurement scale)
Optical noise	1). Spectral center wavelength drift 2). Spectral bandwidth broadening/narrowing 3). Visibility changes of the spectrum	Optical source: LED; Optical spectrometer; Polarizer (analyzer); Transmission fiber;	1) 3°C (0.19% full measurement scale) 2) 0.05°C (0.00312% full measurement scale) 3) 1°C (0.06% full measurement scale)
Mechanical noise	Mechanical vibration	Polarizer and sensing element relative position changes	5°C (0.3% full measurement scale) in the range of 5° rotation

Opto-electronic noise reduction

In a relatively constant room temperature environment, to remove the dark current noise of the CCD detector, a dark spectrum can be pre-stored in the computer and then subtracted from each of the measured spectra. In Figure 4.31, the spectrum is measured with dark current subtraction, readout noise can still be observed. To further improve the signal-to-noise ratio (SNR) of the optical spectrum measurements for the accurate peak and valley location determinations, a boxcar algorithm is developed to smooth the raw data.

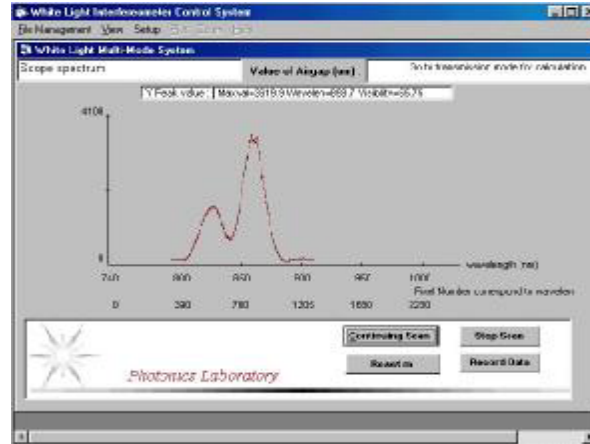


Figure 4.31. The measured interference spectrum after dark current subtraction

Since the noise from each of the CCD pixels is independent, noise in each individual detector pixels can be minimized with information from the adjacent pixels, so that the spectrum curves can be smoothed. Suppose the measured spectrum is $\{f(i), i=1,2,\dots, 2048\}$, the detector pixel i is smoothed using the adjacent $-w \sim +w$ pixels in the boxcar smoothing process, the smoothed result $f_s(i)$ will be:

$$f_s(i) = \frac{1}{2w+1} \sum_{j=-w}^{j=w} f(i+j) \quad (4.36)$$

where $2w$ is defined as the smoothing window width.

One important parameter of the boxcar-smoothing algorithm is the window width, which must be selected very carefully. Obviously, the larger the window width, the better the performance can be achieved. On the other hand, a large window width will cause two problems. First, the visibility of the spectrum will decrease when the window width is increased, this is the character of the averaging algorithm. Second, because the interference spectrum is not a symmetric function of the wavelength, the averaging process will induce the deformation of the interference spectrum and shift the peak/valley positions. These effects are shown in Figure 4.32, Figure 4.33 and Figure 4.34.

Figure 4.32 shows the simulated result for a small smoothing window width ($w=5$; $OPD=11\mu\text{m}$). In this figure, no obvious deformation can be observed, and a high visibility of the interferogram was achieved.

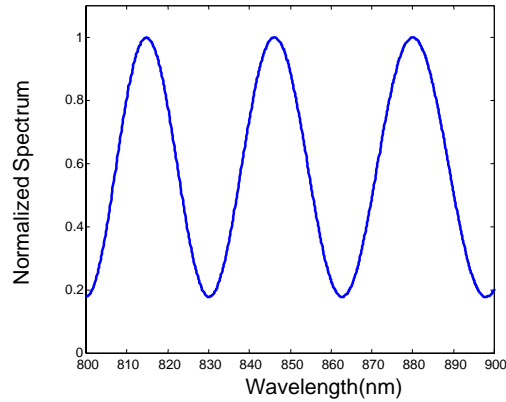


Figure 4.32 Simulated result for spectrum curve smoothing with small window width ($w=5$)

Figure 4.33 shows the simulated result for spectrum curve smoothing with a large window width ($w=80$). The visibility of the interference spectrum decreases dramatically and obvious deformation can also be observed. Figure 4.34 shows the measured normalized spectrum when a large window width was used ($w=61$), the spectrum deformation is very similar to the simulated results shown in Figure 4.33.

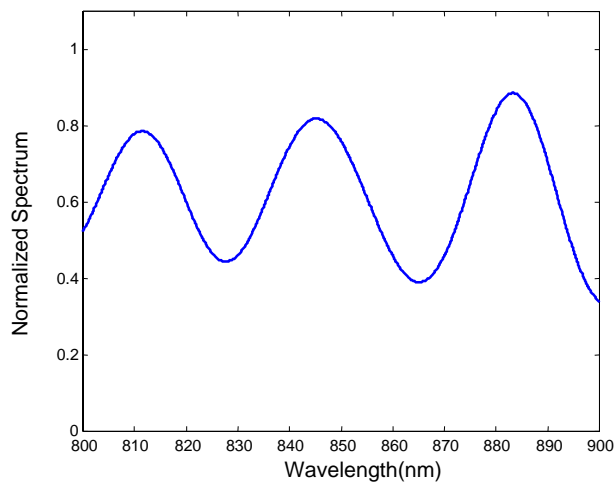


Figure 4.33 Simulated result for spectrum curve smoothing with a large window width ($w=80$)

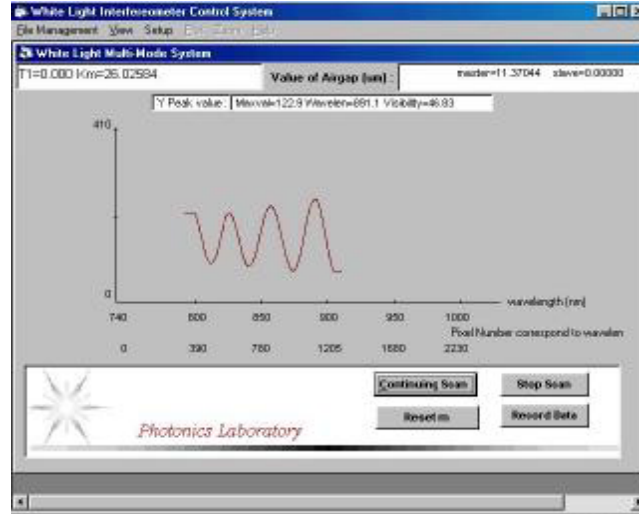


Figure 4.34 Measured spectrum after curve-smoothing with a window width ($w=61$)

To obtain the best performance and prevent the deformation of the interference spectrum, the window width needs to be optimized for different CCD detectors, the light source and the OPD values of the sensing elements. The basic principles are: the more the CCD pixels in a unit wavelength space, the larger window width can be used; the smaller the OPD values of the sensor (which means the space between adjacent peaks/valleys is large), the larger window width can be used.

Optical noise reduction

When the center wavelength of the optical source shifts, the positions of the valley points in the interference spectrum are also affected. For the valley points in the interference spectrum Equation (4.4) becomes:

$$\begin{aligned}
 \cos\left(\frac{2\pi L}{\lambda_v}\right) &= -1 \\
 \sin\left(\frac{2\pi L}{\lambda_v}\right) &= 0 \\
 \frac{2\pi L}{\lambda_v} &= (2k+1)\pi
 \end{aligned} \tag{4.37}$$

For the shift in the valley wavelength λ_{ν}' , the demodulated OPD is:

$$L_{\lambda}^{\nu} = L - \frac{(1+\gamma)\lambda_{\nu}^3}{4\pi^2\gamma L w^2} \delta_{\lambda} \quad (4.38)$$

Choosing the peak point and the valley point to be close to the central wavelength of the light source, then $\lambda_p \approx \lambda_{\nu} \approx \lambda_0$, and Equation (4.13) and Equation (4.38) become

$$L_{\lambda}^p = L + \frac{(1+\gamma)\lambda_0^3}{4\pi^2\gamma L w^2} \delta_{\lambda} \quad (4.39-a)$$

$$L_{\lambda}^{\nu} = L - \frac{(1+\gamma)\lambda_0^3}{4\pi^2\gamma L w^2} \delta_{\lambda} \quad (4.39-b)$$

With a first order approximation, Equation (4.39) shows that the location changes of the peaks and the valleys caused by the center wavelength drifts affect the OPD measurement in opposite manners, thus the wavelength drifts effect can be partially compensated by combining Equation (4.39(a)) and Equation (4.39(b)), i.e. using both peaks and valleys to calculate the OPD instead of using peaks or valleys alone,

$$L = \frac{L_{\lambda}^p + L_{\lambda}^{\nu}}{2} + O(\delta\lambda^2) \quad (4.40)$$

In analogy to the compensation method used for the center wavelength shifts, the effect from the bandwidth variations can also be compensated using both the valley points and the peak points in the interference fringes. Applying Equation (4.37) on the valley points, the calculated OPD based on the shift in the valley wavelength λ_{ν}' is obtained as,

$$L_{\lambda-w}^{\nu} = L - \frac{(1+\gamma)\lambda_p^3}{2\pi^2\gamma L w^3} \delta_w \quad (4.41)$$

Both the peak point and the valley point are chosen to be the ones closest to the central wavelength of the light source, thus $\lambda_p \approx \lambda_{\nu} \approx \lambda_0$, and Equation (4.22) and Equation (4.41) become,

$$L_{\lambda-w}^p = L + \frac{(1+\gamma)\lambda_0^3}{2\pi^2\gamma L w^3} \delta_w \quad (4.42-a)$$

$$L_{\lambda-w}^v = L - \frac{(1+\gamma)\lambda_0^3}{2\pi^2\gamma L w^3} \delta_w \quad (4.42-b)$$

With a first order approximation, Equation (4.42) shows that the spectral bandwidth narrowing/broadening effects will also affect the OPD measurement in opposite manners. Then, by combining equation (4.42-a) and Equation (4.42-b), i.e. using both peaks and valleys to calculate the OPDs, the spectral bandwidth can also be partially compensated.

$$L = \frac{L_{\lambda-w}^p + L_{\lambda-w}^v}{2} + O(\delta_w^2) \quad (4.43)$$

Mechanical noise reduction

Most likely, the rotation of the sensing element relative to the polarizer is caused by the environmental mechanical vibrations. To prevent the optical misalignment caused by the rotation of the sensing element in the sensing probe, a single crystal sapphire inner tube is used to hold the sensing element tightly in a fixed position. The single crystal sapphire holder has the same coefficient of thermal expansion (CTE) as that of the sensing element, thus the holder is stable and no significant thermal stress is generated at different temperature levels.

4.7 Power budget

The power attenuation factors in the BPDI sensor system include fiber transmission losses; coupling losses between the optical fiber and the optical collimator; reflection losses at the surface of the optical components; power losses at the polarizer/analyzer because light with only one linear polarization direction can pass. These attenuation factors are shown in Figure 4.35 and their magnitudes are estimated as follows:

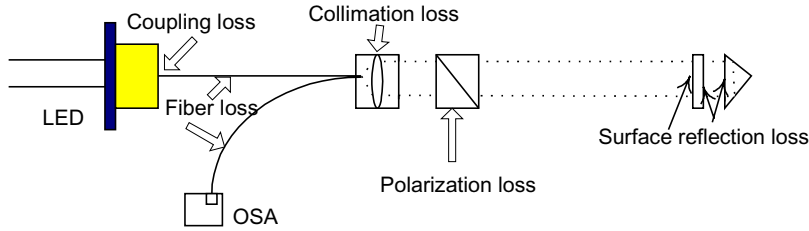


Figure 4.35. Optical power losses in the BPD sensor system.

Fiber coupling loss ($L_{coupling}$)

The coupling efficiency between the edge-emitting LED (Honeywell HFE4854-014) and the multimode optical fiber (200 μm core diameter) with a ST connector is 80%, so the loss is about 1dB.

Fiber loss (L_{fiber})

The attenuation in the multimode fiber is 2.2dB/km at optical wavelength of 850nm; the total loss in the transmission fiber depends on the length of the fiber used for both guiding light into the tube and transmitting light to the optical spectrometer.

Collimation loss ($L_{collimator}$)

This loss includes the collimator insertion loss, which is a result of the surface reflection from the collimation lens, and power loss because of the optical beam divergence (0.3 degree) relative to the ideal collimated propagation direction. The collimation loss in the selected collimator is about 1dB.

Surface reflection loss of the optical components ($L_{reflection}$)

For single crystal sapphire, each of the optical quality surface reflection loss is 7%; and for single crystal zirconia, each of the optical quality surface reflection loss is 10%.

The output optical power from the sensing probe should be:

The sensing probe with a SP structure:

$$P_{out} = P_{in} (1 - L_{coupling}) (1 - L_{fiber}) (1 - L_{collimator}) (1 - L_{reflection-sapphire})^2 \quad (4.44)$$

The sensing probe with a SDZP structure:

$$P_{out} = P_{in} (1 - L_{coupling}) (1 - L_{fiber}) (1 - L_{collimator}) (1 - L_{reflection-sapphire})^4 (1 - L_{reflection-zirconis})^2 \quad (4.45)$$

Experimentally, the input power to the SP-structured sensing probe from the 2-meter multimode fiber is 480.4 μ W, the output power from the sensing probe after a 2-meter long multimode fiber is 54.3 μ W, the power loss in the system is then about 89%, or 9.6 dB.

Chapter 5. Performance evaluation of designed temperature sensors

With the design, implementation and optimization of the sensor system described in the previous chapters, this chapter will summarize the experiments and results associated with the single crystal sapphire based BPDI optical fiber sensor system. Some of the most commonly used terminology for optical sensing system specifications and performance characteristics are defined first. The evaluation of the system includes the characterization of the spectral domain white light signal processing unit, sensor system calibration, and overall performance evaluations.

5.1 Definitions of performance characteristics

A wide range of terms has been used to describe the essential performance characteristics of measurement instruments and sensors. The most widely used terms include repeatability, precision, accuracy, resolution, sensitivity, stability, hysteresis, and frequency response [68]. There is always a trade off among these specifications that can be achievable at a given cost. The intention of this section is to provide clear definitions for the terms used to describe the performance of the BPDI temperature sensing system.

Repeatability

The repeatability of an instrument is an indication of its ability to give the same measurement results on the same quantity with repeated measurements under the same conditions. An instrument with good measurement repeatability needs a good design and should be carefully manufactured, so it can provide the same readout. But an instrument with a good measurement repeatability, does not necessarily mean that it has a good accuracy, since it could give the same wrong answer all the time.

Accuracy and precision

The accuracy of an instrument indicates the deviation of the measurement results from the true value of the measurand, so it is a measure of its ability to tell the truth. Accuracy

can be expressed as a percentage of the full scale readings, or as an absolute value over all working ranges of the instrument. Accurate calibration on repeated measurement results against a standard is necessary for a good accuracy for the instrument.

Resolution (Sensitivity)

Resolution or sensitivity of an instrument is defined as the minimum resolvable change in the value of the measurand. The resolution of an instrument can be interpreted by the statistical standard deviation of a series of measurements under stable circumstances. It is common to use twice the standard deviation as the direct measurement of the resolution. The resolution for an instrument usually has different values for different measurement scales.

Stability (Drift)

It is defined as the capability of an instrument to maintain the same output within a specific length of a time period. The stability of an instrument is usually measured by the quantity of drift compared to a standard, which is a well-calibrated measurement instrument.

Hysteresis

If there is a difference between outputs for a given value of the measured quality when the value is approached from above or below, an instrument is said to exhibit hysteresis. It can be significant when rapid level fluctuations are likely to occur, as the result of mechanical friction, magnetic effect, elastic deformation or thermal effects.

Frequency response

This is a measure of the sensor's capability to track dynamic changes of the temperature. For the thermometer, it is characterized by a rise time, which is defined as the time required for the sensor to respond to an instantaneous step function, measured from the 10% to 90% points on the response waveforms [68].

5.2 Characterization of white light signal processor

By incorporating a spectrometer for the purpose of measuring polarization properties as a function of the optical wavelength, the optical broadband polarimetric differential interferometric (BPDI) temperature sensor system provides absolute measurement of the optical path differences (OPD) between the two orthogonal linearly polarized light waves in the single crystal sapphire sensing element. The BPDI sensing system extracts temperature information by calibrated relationship between the OPDs and the temperatures. The absolute temperature measurement is very attractive for harsh environment applications because it requires no initialization and/or calibration when the power is switched on. To make the absolute measurement meaningful, self-compensating capability is desired so that the optical power fluctuations and fiber transmission loss variations can be fully compensated.

5.2.1 Capability of compensating optical source power fluctuations

To evaluate the self-compensating capability of this optical temperature measurement system, the output temperature variations were monitored when the optical source power was altered by changing its driving current. Theoretically speaking, changing the driving current of a semiconductor optical source, such as an LED, would also change the spectrum in addition to the optical power levels. Figure 5.1 shows the measured output powers under different driving currents. The power increases as the driving current increases. The spectral characteristics profiles also change with different driving currents, as shown in Figure 5.2. The distortion of the source spectrum would introduce errors into the measurement results through the normalization process, since the normalization of the interferometric signals is carried out with respect to the pre-stored LED output spectrum, which is fixed. The measured spectral curves after normalization are shown in Figure 5.3 for different driving currents.

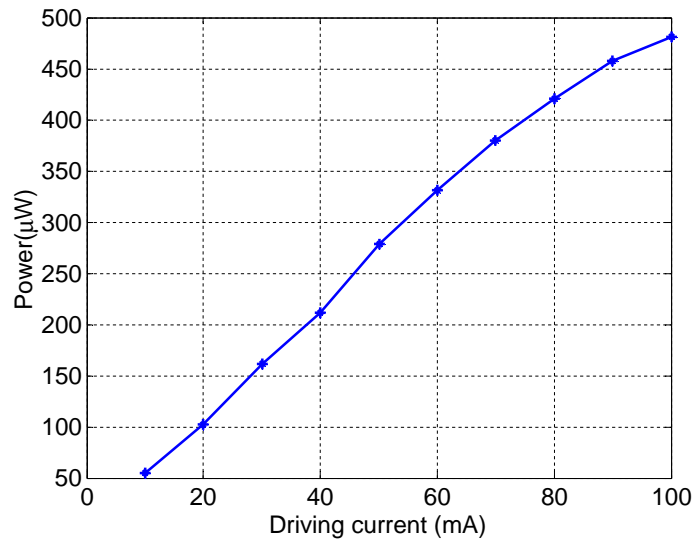


Figure 5.1. Output power levels of the LED with different driving currents

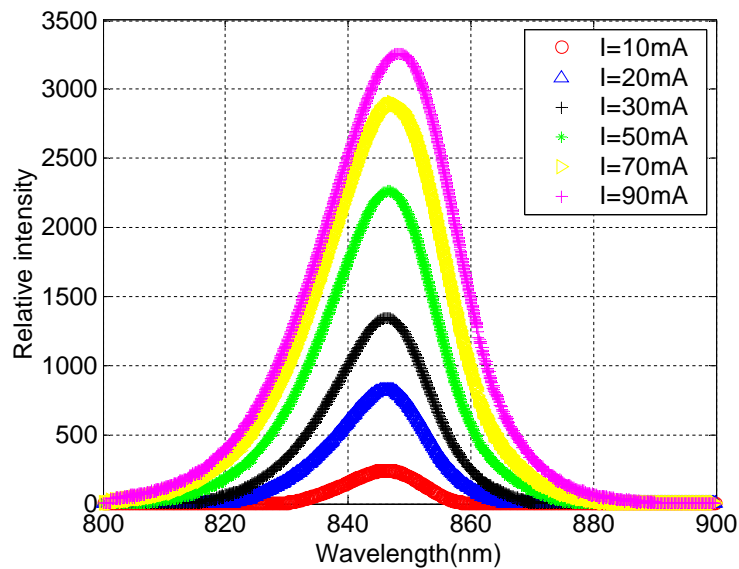


Figure 5.2. Output spectra of the LED with different driving currents.

Figure 5.4 shows the output temperature variations as a function of the normalized optical power of the optical source (LED). As shown, the temperature variation range is limited to $\pm 0.45^{\circ}\text{C}$ for total optical power changes up to 90%. The measurement results shown in Figure 5.4 also indicate the contribution from the source spectrum distortions.

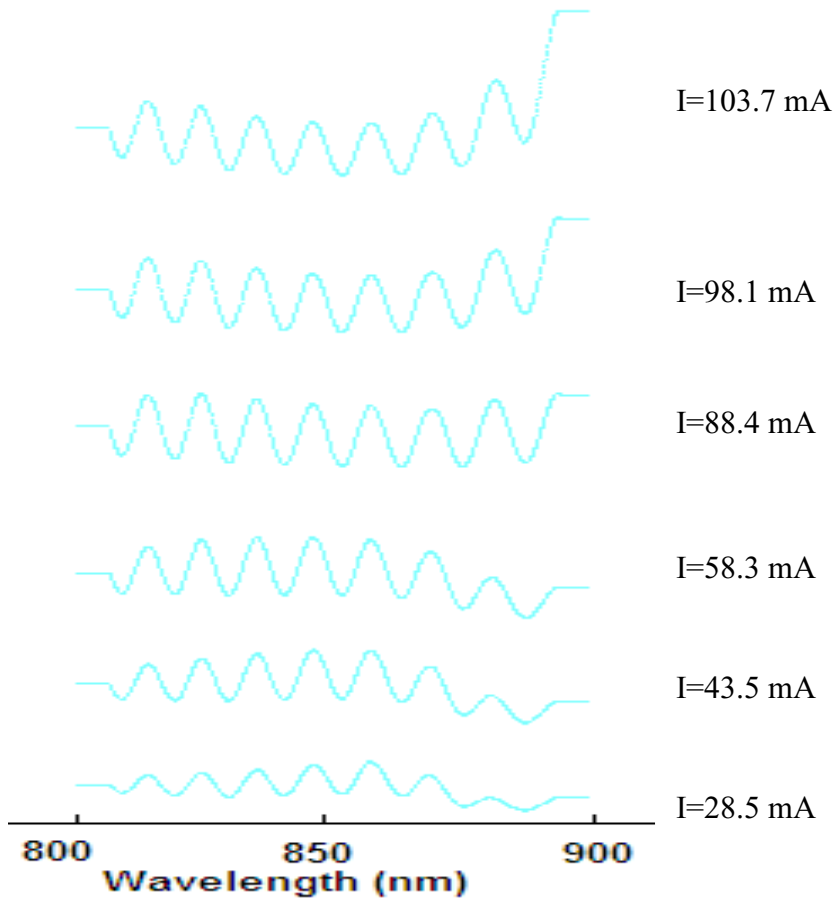


Figure 5.3 Normalized interference fringes for the LED with different driving currents

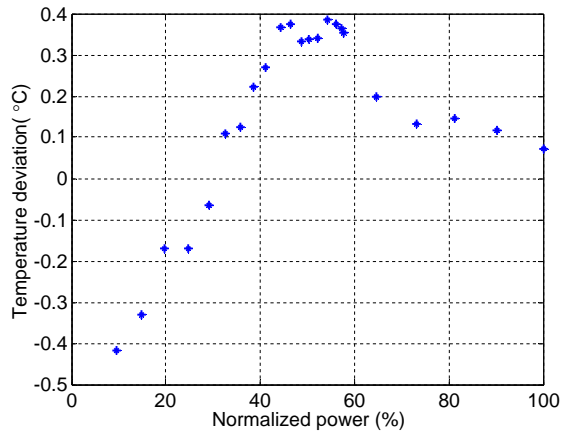


Figure 5.4 Temperature deviations vs. optical source output powers

5.2.2 Capability of compensating optical fiber transmission loss

To evaluate the self-compensating capability of this optical temperature measurement system, the output temperature variations were also monitored when the attenuation in the multimode transmission fiber was changed. Keeping the spectral bandwidth and center wavelength fixed with changes only to the power levels, the observed interferometric signal after normalization is shown in Figure 5.5. Some of the detecting pixels in the CCD array are saturated with 0 dB and 1.8 dB attenuation, thus the curves are deformed. Figure 5.6 shows that the temperature variation is in the range of $\pm 0.4^\circ\text{C}$ for the transmission fiber attenuation up to 9 dB.

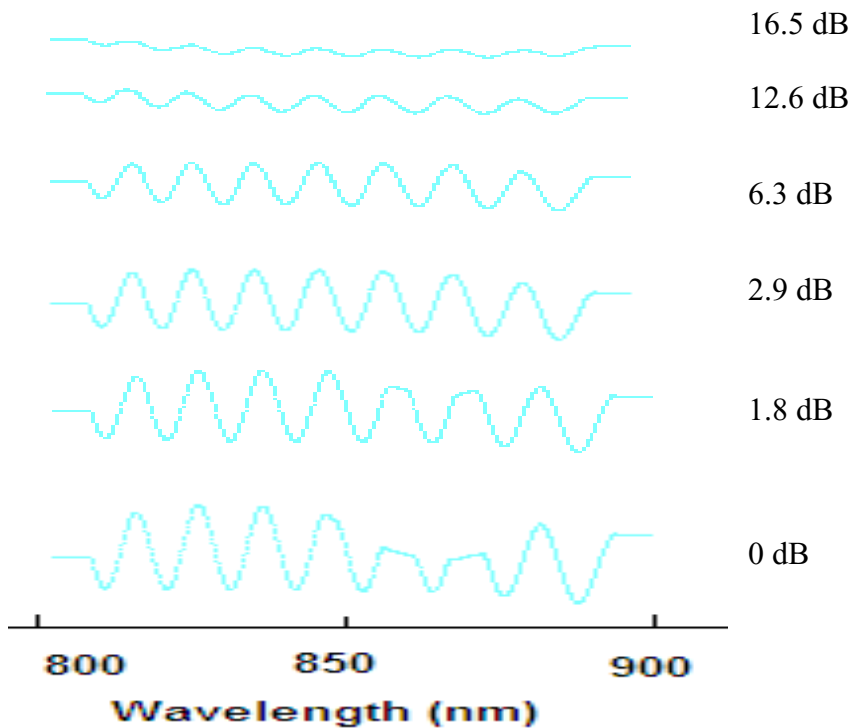


Figure 5.5. Normalized interference fringes for transmission fiber with different attenuations

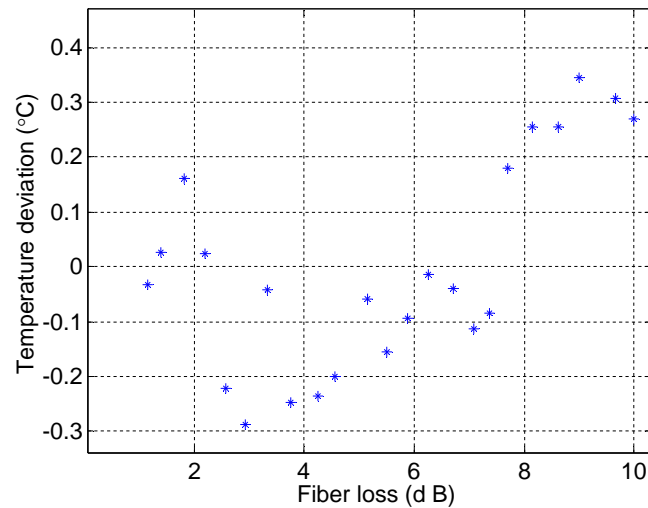


Figure.5.6. Temperature deviation vs fiber transmission loss

5.2.3 Capability of compensating temperature fluctuations

To prove the effectiveness of the first order compensation method for the spectral center wavelength drift and bandwidth broadening/narrowing, which mainly are caused by the environment temperature fluctuations, the whole white light signal processor, including the optical source and spectrometer, was placed inside a Testequity 1000 temperature chamber. The interferometric sensing head structure was kept unchanged in a constant temperature and pressure environment, so the OPD in the sensing element is fixed in order to evaluate the performance of the white light signal processor alone. The temperature in the chamber was set to increase by a step of 5°C in the range from 10°C to 45°C then decrease with the same steps. These temperature increase and decrease processes were carried out twice. The white light signal processor was also tested at room temperature for about 5 hours between the temperature increasing and decreasing processes. The whole test lasted for about 90 hours and the results are shown in Figure 5.7.

The top curve in Figure.5.7 shows the temperatures inside the chamber during the test process, the temperature values were sampled by a K-type thermocouple inside the white light signal processor. The middle curve shows the OPD fluctuations relative to the true

OPD values. The measured OPD is obtained by using only the valley points for signal processing. Its temperature dependence was predicted by Equation (4.38) and verified in this test. In the temperature range of 10°C to 45°C, the temperature dependence of the OPD fluctuations is in the range of about $\pm 9\text{nm}$ before using compensation. The bottom curve shows the OPD fluctuations relative to the true OPD values. The measured OPD is obtained by using the white light signal processor with Equation (4.40) for the compensation. Over the entire tested temperature range, the temperature dependent OPD measurement by the white light signal processor is about $\pm 1.5\text{nm}$, which is improved dramatically compared to the $\pm 9\text{nm}$ deviation shown in the middle curve.

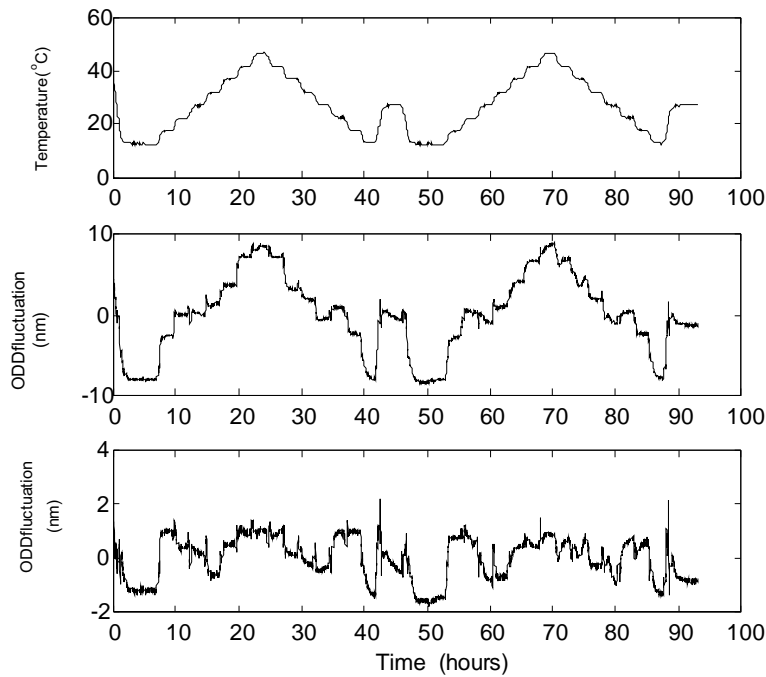


Figure.5.7 Experimental results of temperature compensation with the first order approximation

5.3 Blackbody radiation subtraction

As discussed previously, with a low coherence, broadband spectral light source illuminating the polarimeter, the interference spectral signal contains the OPD information. After normalization of the measured spectral curves $I(\lambda)$ with respect

to the pre-stored spectrum $I_s(\lambda)$ of the broadband input light source, the interference spectrum would form a sinusoidal curve if plotted in the wave numbers, as shown in Figure 5.8. The normalized interferometric spectral curve consists of a series of maxima and minima (peaks and valleys of the interference spectral curves) at certain wavelengths. Based on these peaks and valleys, the OPD values can be calculated.

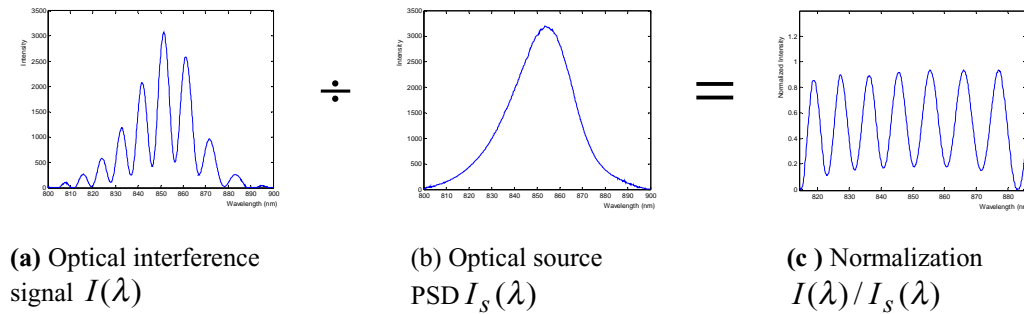


Figure 5.8. Normalization of the optical spectrum

As temperature increases, the blackbody radiation is superimposed on the optical interference signals used for the temperature monitoring, and becomes increasingly stronger with the increasing of temperature. The measured optical spectral curves will then be elevated with the addition of the undesired background, as shown in Figure 5.9. Theoretical simulations of the normalized intensity distribution of blackbody radiations at different temperatures are plotted in Figure 2.12 for the wavelength range of interest, which shows that the effect of the blackbody radiation becomes more apparent for temperatures over 1000 °C.

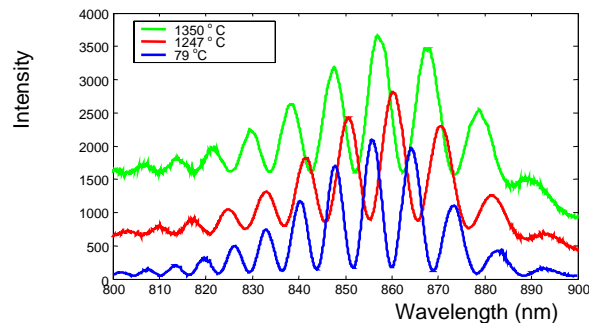


Figure.5.9. Blackbody radiation effect on the measurements of optical temperature signatures

When those background-raised spectral curves are normalized with respect to the $I_s(\lambda)$, deformed sinusoidal curves are obtained and the calculated OPD values are not accurate, and therefore the temperature measurements would be inaccurate.

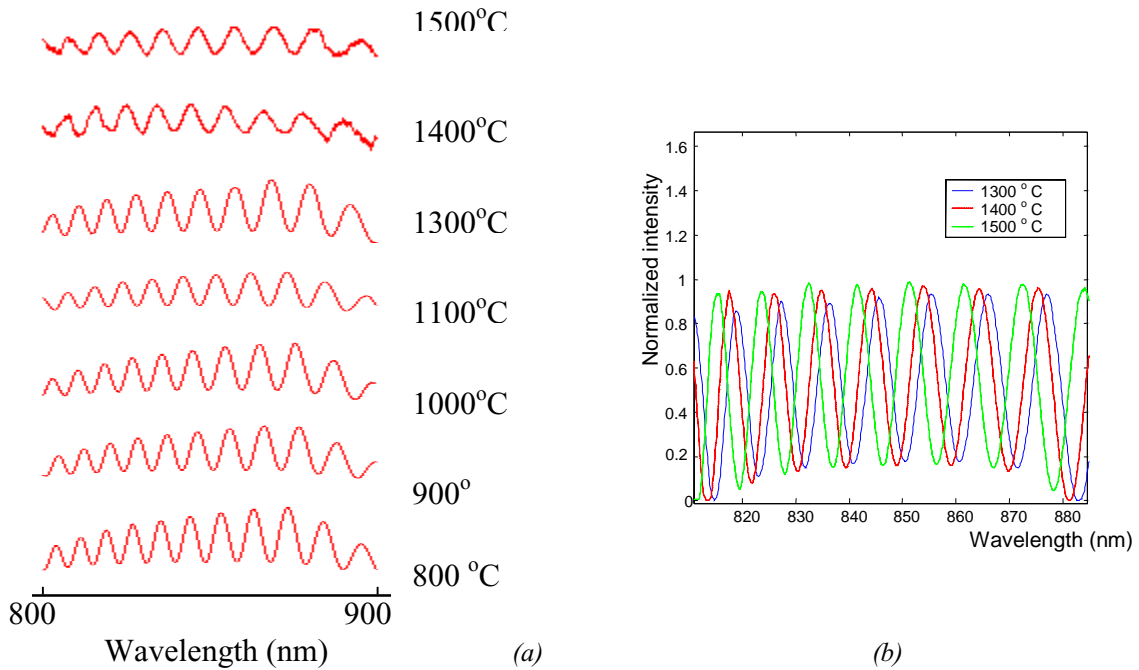


Figure. 5.10. Normalized optical spectra measured at different high temperature levels

In order to minimize the influence of the blackbody radiation background, especially for the situation of temperature over 1000 °C, a signal generator is used to modulate the LED driving current with low frequency square-wave signals, thus the output light from the LED will be modulated and converted into alternating component (AC) signals. The background from the blackbody radiation is essentially a direct component (DC) signal. The AC signal from the modulated optical source carries temperature information. Digital signal filtering techniques, described in Chapter 4 are used to block the DC signal. The AC signal will be filtered out for further signal processing for temperature measurement. With the optical source modulation and the digital signal filtering techniques, the blackbody background is subtracted sufficiently for the high temperature measurements, as shown in Figure 5.10. The modulation frequency is selected to be 8Hz, such that the CCD detector in the spectrometer can measure the spectrum without being affected by its

“deadtime” for electric charge transfer. The data transfer rate for the CCD array is 13ms for the full scan into the computer memory, shown in Table 3.1.

5.4 Calibration of BPGI sensing system

In order to use the BPGI sensor system for temperature measurement, it must be calibrated to relate the OPD values to the applied temperatures. The sensor calibration is usually conducted by applying known temperatures within its operating range. The one-to-one relation between the OPD and the applied temperatures forms the calibration curve which can be stored in the host computer and later used to convert the OPD into the temperature readings.

5.4.1 Construction of temperature calibration system

A temperature acquiring subsystem is constructed to obtain the real-time temperature for the calibration purpose. In this subsystem, real time temperature values from a thermocouple are displayed in the temperature monitor and then acquired by a computer using a RS232 interface, as shown in Figure 5.11. In the computer, the temperature values will then be one to one related to the OPD in the sapphire sensing element by software communication between the temperature acquiring subsystem and the OPD measurement and calculation subsystem.

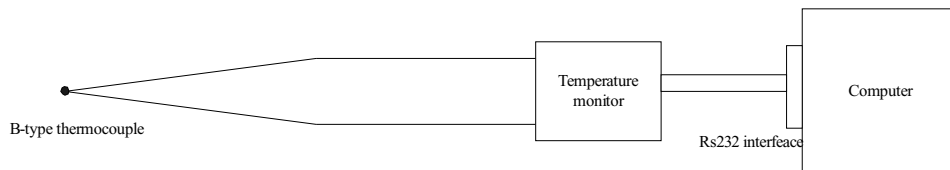


Figure 5.11. Temperature acquisition subsystem for the calibration purpose

One DPi32-C24 temperature monitor from Omega[®] is used to acquire the temperature values from the K-type and the B-type thermocouples. A type K thermocouple (with resolution of 0.05 °C) is used for temperatures below 200 °C, and a type B high-temperature thermocouple (with resolution of 0.2 °C under 500 °C and of 0.1°C above 500 °C) is used for temperatures above 200 °C. An RS-232 serial digital communication

port is used to communicate with the computer directly. By employing the Microsoft® Visual Basic software, a graphical user interface (GUI) is designed to display the real-time temperature and the related OPDs simultaneously. Each of these temperature values is uniquely related to one OPD value. As shown in Figure 5.12, the OPD value is 20.10391 μm at temperature 1181.0 $^{\circ}\text{C}$.

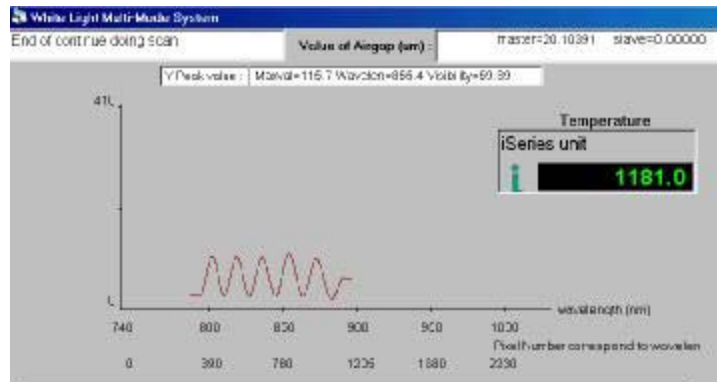


Figure 5.12. Real time temperature is related to an OPD value through a GUI interface

5.4.2 Temperature sensor calibration

During the calibration process, the sensing element was heated in a high temperature furnace up to 1600 $^{\circ}\text{C}$. Each OPD value obtained from the optical spectral temperature signature and each of the real-time temperatures acquired from the thermocouple are related simultaneously and stored in the computer. To ensure the accuracy of the calibration, thermal equilibrium between the sensing element and the environment is necessary. The system is thus held at a stable temperature level for about half an hour before moving to the next level. Figure 5.13 shows the typical applied temperature data, and Figure 5.14 shows the OPDs recorded from the BPGI sensor system during the sensor calibration process. The sensing element used in the tests was a single crystal sapphire disk with a thickness of 1.5mm and an initial OPD value of 25.887 μm at room temperature environment. Figure 5.15 is a plot of the OPD versus the applied temperature after averaging. By taking the average of the temperatures within the temperature-holding period, the measurement error is minimized. The one-to-one relation of the applied temperature and the OPD was then used to find the calibration equation through a

polynomial curve-fitting. With the minimum root mean square error between the experimental results and the fitting-curve, experimental results revealed that the optimal order of the polynomial curve-fitting is 3:

$$T = 0.320d^3 - 29.836d^2 + 604.86d - 1085.7 \quad (^\circ\text{C}) \quad (5.1)$$

With a single crystal sapphire prism as a sensing element, its initial OPD is $66.894\mu\text{m}$ under room temperature, and the calibrated polynomial equation is:

$$T = 0.011d^3 - 2.66d^2 + 94.06d + 2419.7 \quad (^\circ\text{C}) \quad (5.2)$$

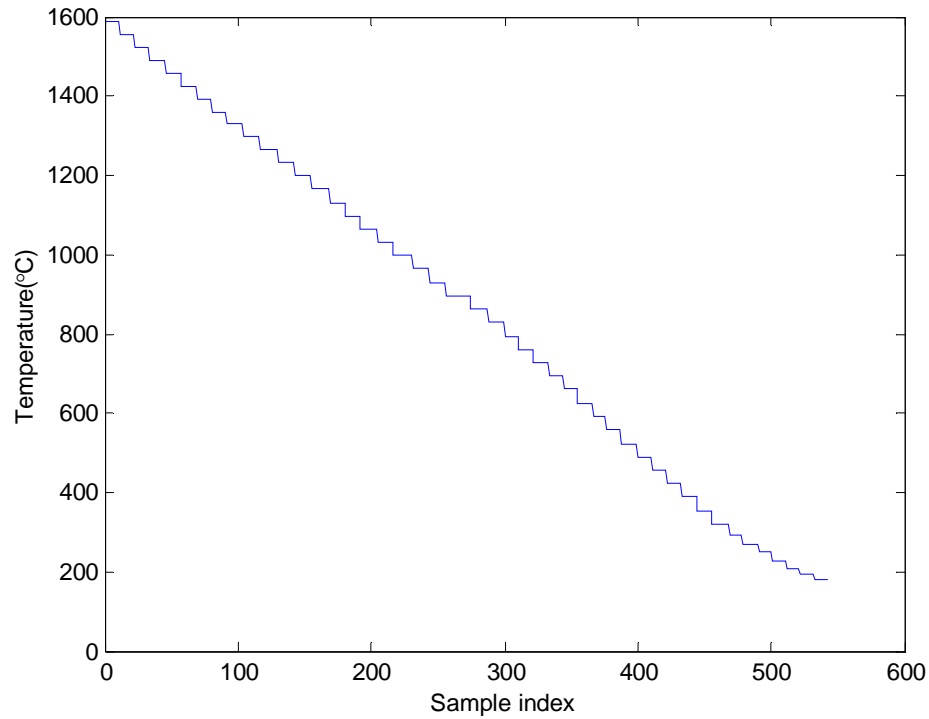


Figure 5.13. Applied temperature during the sensor calibration process

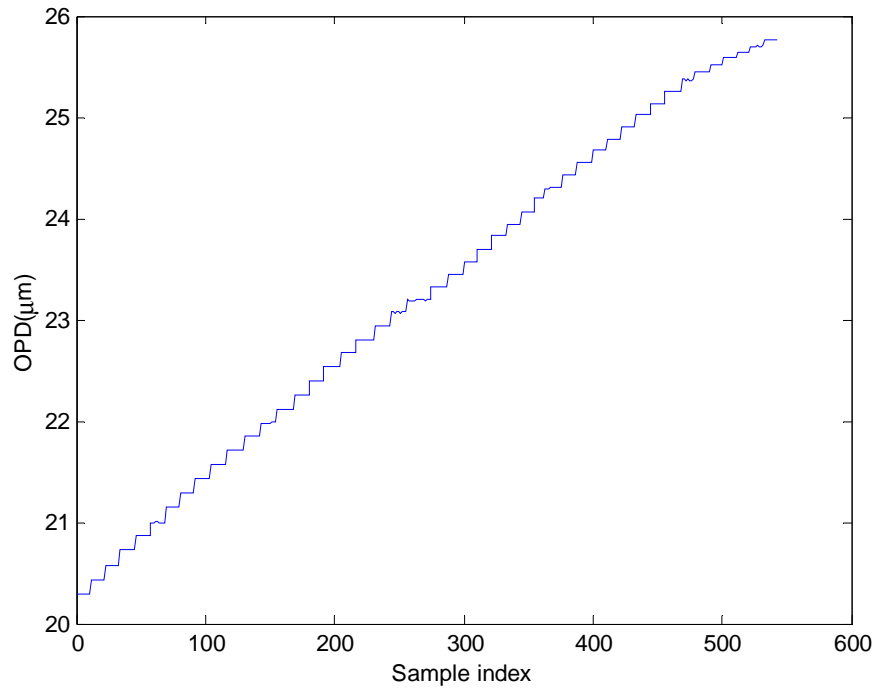


Figure 5.14. OPDs measured with the BPDI sensor system during the sensor calibration process

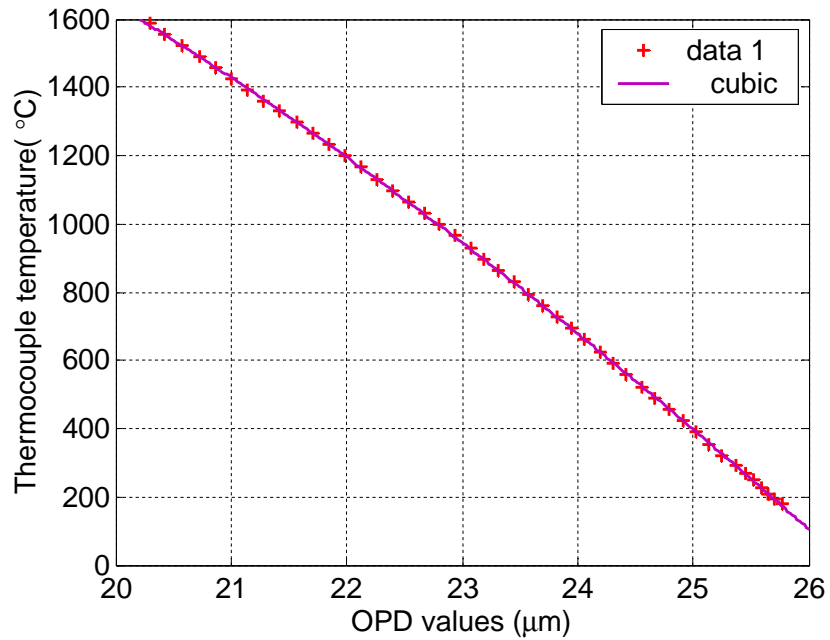


Figure 5.15. The BPDI sensor system calibration curve for a sapphire sensing disk with thickness of 1.5mm

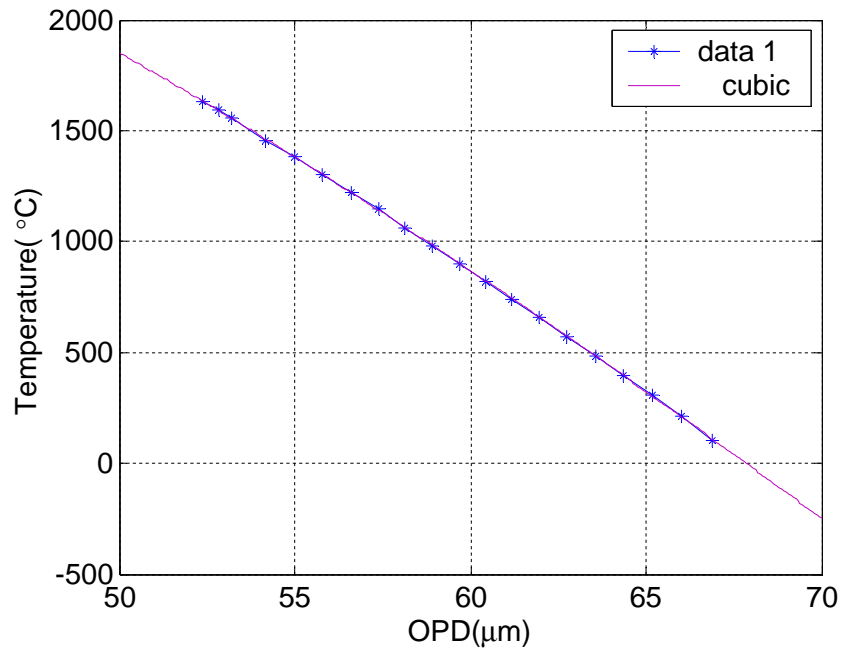


Figure 5.16. The BPD sensor system calibration curve for a sapphire sensing prism (equivalent to a sensing disk with thickness of 8mm)

For one sensing element, the accurate calibration curve was usually obtained by taking the average of several consecutive calibration data to further ensure the accuracy of the calibration. With the calibrated sensor, the performance of the developed BPD temperature sensing system, such as repeatability, accuracy compared to the thermocouple and temperature measurement resolution can then be evaluated in detail.

5.5 Performance evaluations of BPD sensing system

5.5.1 Repeatability of the measurements

Repeatability of the sensor measurement can be evaluated by applying temperature to a certain preset point repeatedly from one direction (increasing or decreasing). The largest difference of the sensor output readings can be used to specify the repeatability of the sensor. With a 1.5mm sapphire disk as the sensing element, four consecutive measurements were performed for the temperature cooling down processes from 1600 °C to 280 °C, the results are shown in Figure 5.17. The temperature values on the x-axis are the thermocouple reference readouts.

As shown in Figure 5.18, the maximum deviation between the measured temperature and the calibrated temperature was within the range of ± 2.5 °C. The normalized repeatability of the sensor system with respect to its dynamic range is therefore $\pm 0.14\%$ of the full measurement scale; this represents the measurement precision that this system can achieve.

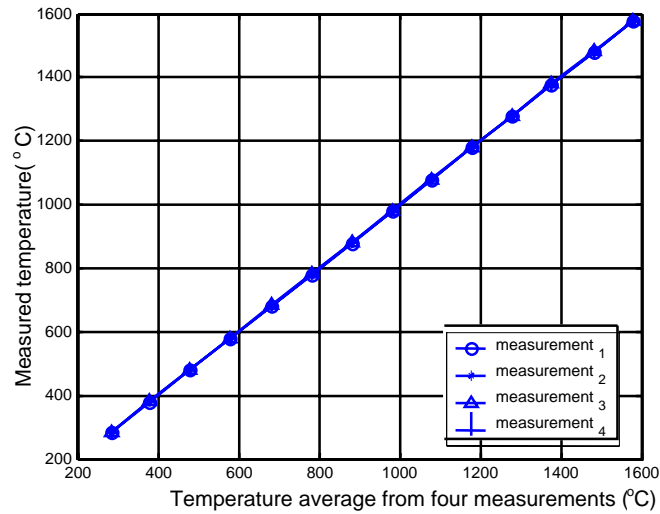


Figure 5.17. Repeatability testing results of the temperature measurements

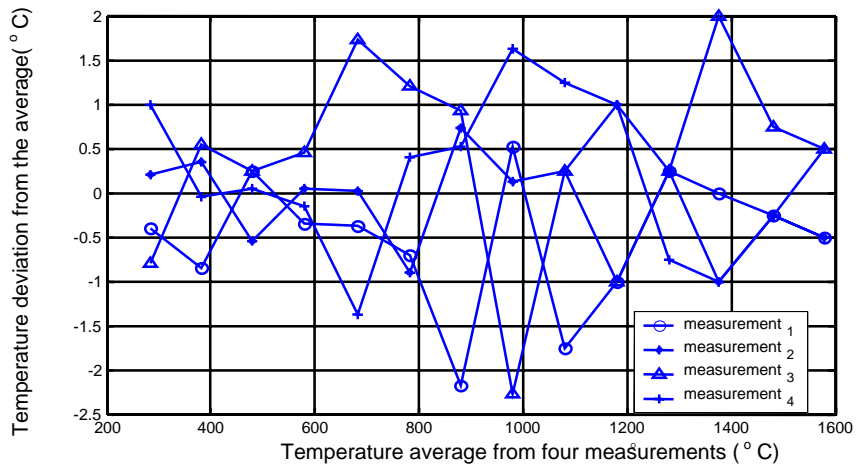


Figure 5.18. Deviation of the measured temperatures with respect to the reference data

5.5.2 Evaluation of accuracy

A K-type thermocouple is employed for the system calibration from room temperature up to 200 °C, and a B-type thermal couple is used from 200°C up to 1600 °C. The type K thermocouple has a resolution of 0.05 °C, with an accuracy of ± 1.5 °C, type B high-temperature thermocouple has a resolution of 0.2 °C under 500 °C and of 0.1°C above 500 °C, with an accuracy of ± 2 °C. With a 3rd order polynomial as a calibration curve, Figure 5.19 shows four measurement results, and Figure 5.20 shows their deviations from the thermocouple reference for each of the measurements, which gives an accuracy in the range of ± 6 °C, and 0.43% for the full measurement range.

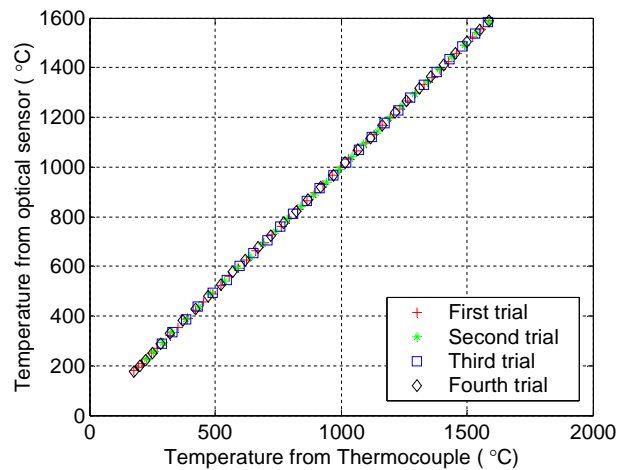


Figure 5.19. Optical sensing system measurement results vs a B-type thermocouple measured temperatures.

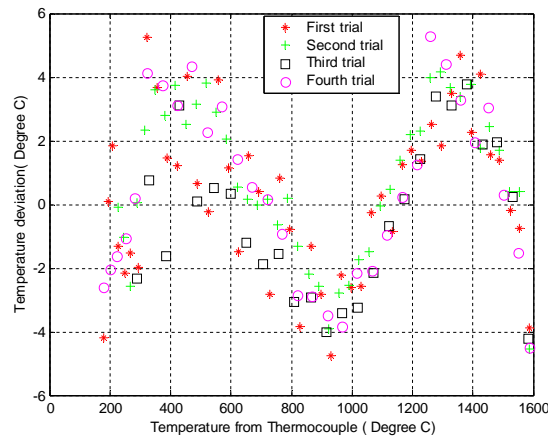


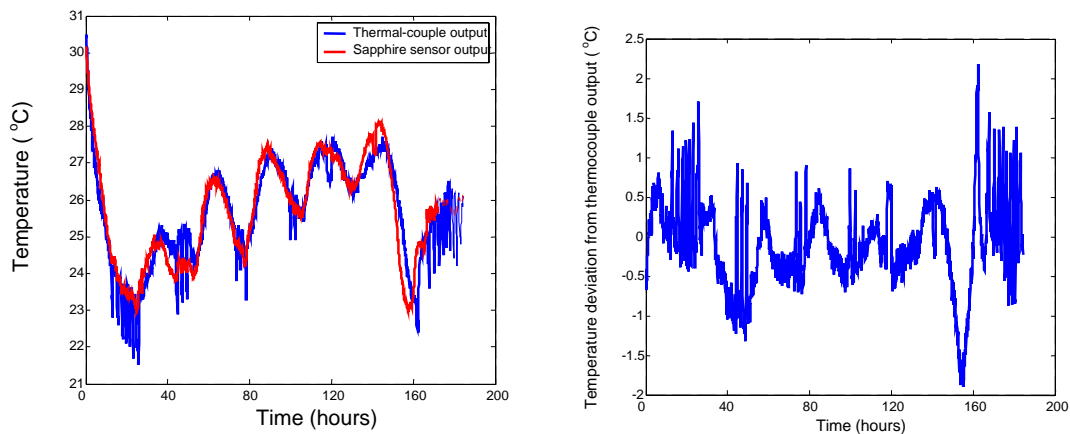
Figure 5.20. Deviation between the temperature measurement results from the B type thermocouple and the optical sensing system

5.5.3 Long-term stability tests

Most optical sensors require accurate optical alignments, and mechanical vibration-proof working environments to maintain its long-term stable operation. The BPDI optical thermometer takes advantages of both optical fibers and bulk optics to ensure its long-term stability for industrial field applications. Bulk optics is convenient for alignment and also relaxes requirements on vibration proof devices. And optical fibers can transmit light for a long distance with small attenuation, as well as are implemented easily in the industrial environments because of their small size, light weight and their immunity to the electromagnetic interference (EMI). The spectral domain optical signal processing technique also provides better stability than intensity based optical signal processing techniques.

The long-term stability testing results are shown in Figure 5.21. These experiments were carried out at different temperature levels: 26°C, 300°C, 600 °C , 900 °C and 1200 °C. The temperature readout differences between the thermocouple and the optical thermometer is in the range of ± 2 °C for tests over 160 hours, which means the normalized maximum variation is 0.13% of the full dynamic measurement range.

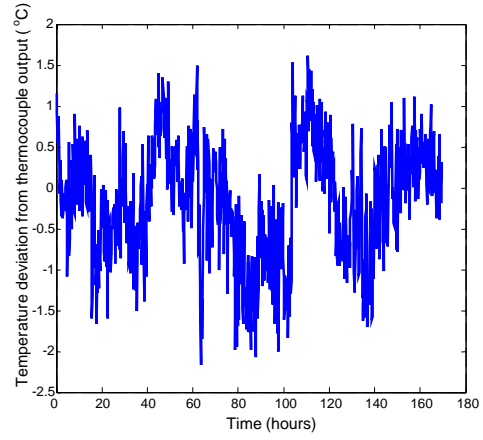
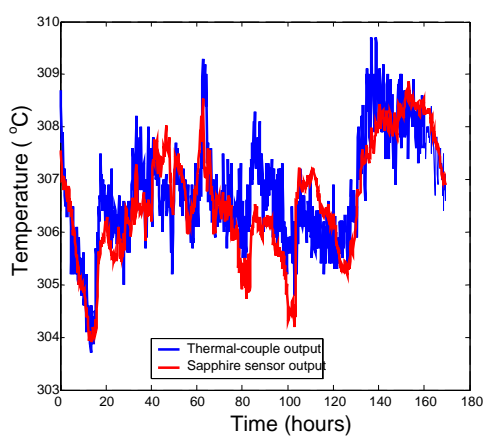
Figure 5.21 (e) also shows the long term performance degradation of the thermocouple operated at 1200 °C, while optical thermometer performed well.



(1) Long-term operation

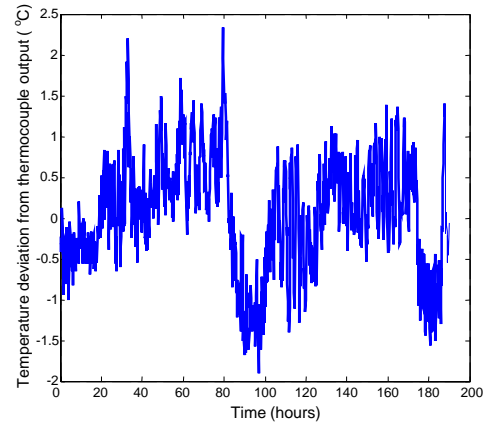
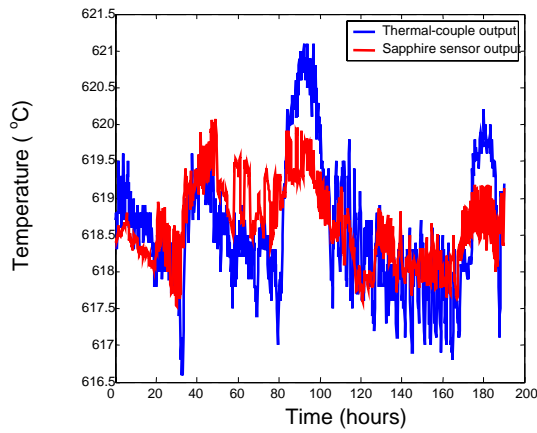
(2) Deviation between the thermocouple and the optical sensor

(a) At 26°C



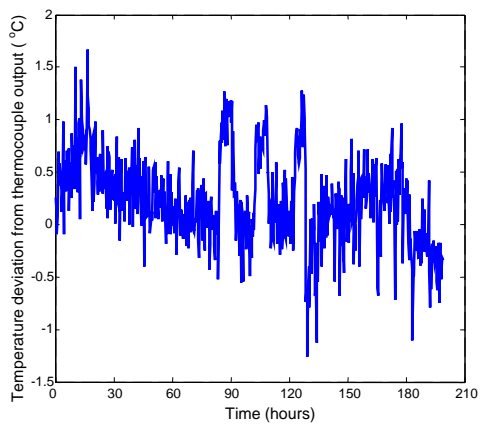
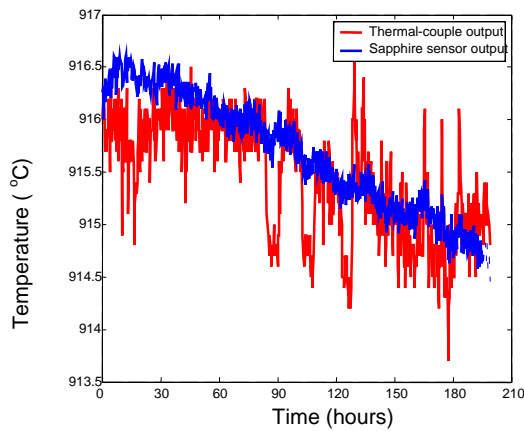
(1) Long-term operation
(b) At 306°C

(2) Deviation between the thermocouple and the optical sensor



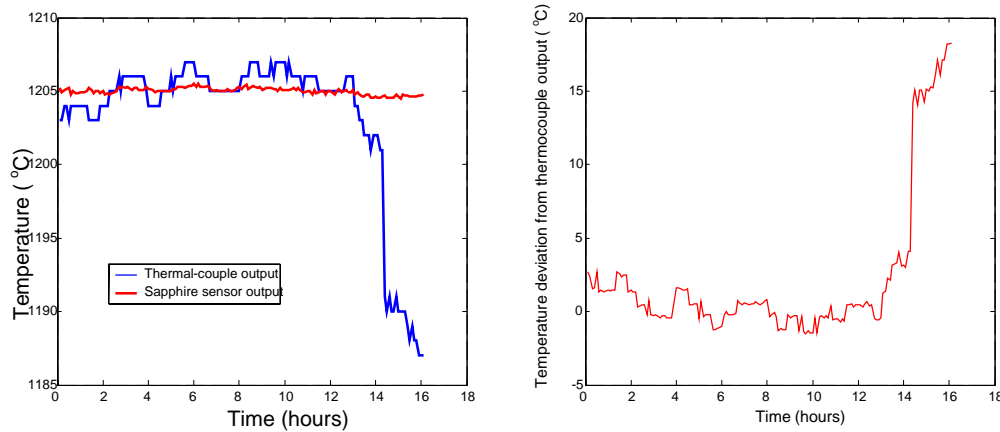
(1) Long-term operation
(c) At 619°C

(2) Deviation between the thermocouple and the optical sensor



(1) Long-term operation
(d) At 915°C

(2) Deviation between the thermocouple and the optical sensor



(1) Long-term operation (2) Deviation between the thermocouple and the optical sensor
(e) At 1205 °C

Figure 5.21. Long-term stability testing results

It must be noted that the complete evaluation of the system stability needs much longer testing period (for example, one year). Therefore, the stability testing results of 160-hour period are not quite conclusive.

5.5.4 Sensitivity (resolution) tests

Interferometric sensors have the reputation of being extremely high sensitive by detecting the differential phase changes. The resolution of the sensor system can be interpreted by its standard deviation of a series of temperature measurements at one constant temperature value. It is common to use twice the standard deviation as the direct measurement of the resolution. The evaluation of the sensor resolution was performed using a calibrated sensor at room temperature and also at 618°C. In the tests, 1000 temperature values were acquired continuously and the resulting histogram is plotted in Figure 5.22. The standard deviation of the temperature data was calculated to be $\sigma=0.0348^{\circ}\text{C}$ and $\sigma=0.0343^{\circ}\text{C}$. Therefore, the resolution of the sensor system was estimated to be $2\sigma=0.0696^{\circ}\text{C}$ and $2\sigma=0.0686^{\circ}\text{C}$. The normalized resolution with respect to the dynamic range of the system was 0.005% of the full scale.

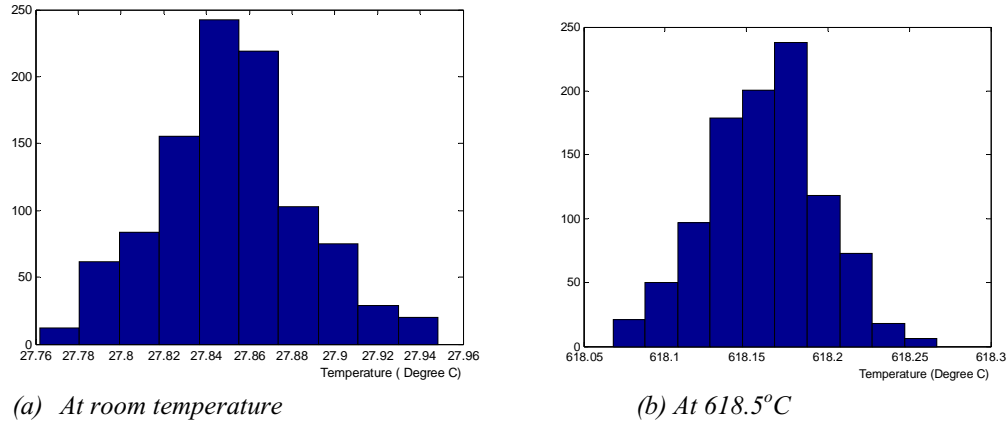


Figure 5.22: Histogram of temperature measurement

5.5.5 Hysteresis in the temperature measurements

Hysteresis of the temperature sensor can be measured by cycling the applied temperature between the minimum and the maximum of the operating range in both increasing and decreasing directions. The hysteresis can be calculated as the largest difference among the output readings of the temperature cycles.

To accurately measure the temperature in a coal gasifier, it is important to reach the temperature equilibrium between the host media and the sapphire sensing element, which is enclosed by a sapphire tube as protection housing. The process to build the thermal equilibrium is determined by the heat transfer between the sensing element and the host media, which highly depends on the thermal properties of the sapphire material, such as thermal conductivity, heat capacitance, and the dimensions of the sensing element. protection housing as well as the temperature levels. Since all of these contribution factors are temperature dependent, a well-designed thermal model is necessary to analyze the hysteresis of the system. The theoretical descriptions and experimental data of the thermal properties of the single crystal sapphire are reasonably well known at low temperature levels, but its thermal properties at high temperature levels have not been extensively studied so a pure theoretical description is not possible, the hysteresis has to be derived experimentally.

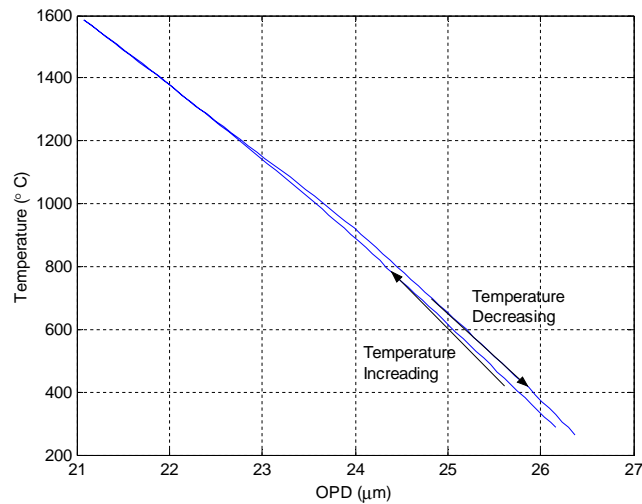


Figure 5.23. Hysteresis of the BPD temperature sensor

The experimental evaluation was conducted using the high temperature furnace after the sensor system was calibrated. The applied temperature was first increased to the temperature of 1580°C at a rate of $2^{\circ}\text{C}/\text{minute}$. The temperature was then decreased to 250°C at the same rate after it was maintained at 1580°C for half an hour. The measurement results are shown in Figure 5.23. It is shown that the hysteresis can be as little as $3\text{--}5^{\circ}\text{C}$ for the operating temperature over 1200°C , which is in the range of the measurement accuracy of the system, while for temperature below 1200°C , the maximum hysteresis is about 50°C .

This experimental result is understandable since the thermal properties of the single crystal sapphire material, and the dimensions of the sensing element and the protection housing will not change much at different temperature levels. It is the temperature dependent heat transfer processes that result in the larger hysteresis at low and medium temperature levels. Usually, three mechanisms of heat transfer—conduction, convection and radiation—regulate the sapphire probe's temperature in a coal gasifier. Gases have relatively low thermal conductivities so conduction will not be important at all temperature levels. The convection heat transfer will dominate the heat transfer to the sensing element at low and medium temperatures (up to a few hundred degrees) because of the gases circulation in the chamber. At high temperatures (above $\sim 800^{\circ}\text{C}$), radiation becomes stronger for the heat transfer between hot walls and protruding probes in

addition to the convection. Radiation transfer is defined fundamentally by the Planck function, and is proportional to the fourth power of the temperature. The single crystal sapphire protection housing can absorb the radiation at its exterior surface and the absorbed radiation thermal energy is then conducted to the sensing element to reach the thermal equilibrium. It also transmits electromagnetic energy from a wavelength of 0.25 μm in the UV range to the visible range of 6 μm in the IR range with a transmission larger than 80%, so the sensing element can also absorb the radiation energy directly. Radiation plus convection can then transfer thermal energy to the sensing element more efficiently than convection heat transfer alone, then the thermal equilibrium can be reached fast enough at the high temperature level, and no large hysteresis can be noticed. The goal for the designed sensor is to measure high temperature over 1200 °C in coal gasifiers. These testing results show that the hysteresis can be negligible at those temperature levels.

5.5.6 Frequency response

The frequency response of a sensing system describes its dynamic response capability. In certain application environments, such as in gas turbine engines, gas temperature can reach over 1000°C in a few seconds; the dynamic response of the temperature measurement equipment is critical in such applications. While for the temperature measurement in coal gasifiers, the temperature variations are in the low frequency range, and the frequency response is not so critical compared to the requirements on its long term survivability and stability. In this section, the frequency response characteristic is evaluated for the developed BPGI temperature sensing system.

The frequency response of the developed sensor system depends on three factors, including the response time of the sensing element to the dynamic environmental temperature changes; the heat transfer rates between the sensing element and the host media; and the signal processing time needed for the temperature information extraction from the optical signals.

The response time of the sensing element describes its thermal transient response characteristic. Assuming that the temperature distribution in the sapphire-sensing element is uniform at any instant of time, the temperature (T) of the sensing element is an exponential function of time [68],

$$\frac{T - T_{env}}{T_0 - T_{env}} = e^{(-hA/mc)t} \quad (5.5)$$

where T_{env} is the environmental temperature, T_0 is the temperature of the sensing element at time zero, h is the thermal conductivity of the sapphire material, A is the heat transfer area of the sapphire material, m is the mass of the sensing element, and c is the heat capacity of the sensing element. The thermal response rise time for the sensing element is the time required to achieve a response from 10% up to 90% of the step input of the temperature, represented by τ , and given by:

$$\left. \begin{aligned} e^{(-hA/mc)t_1} = 0.9 &\Rightarrow t_1 = 0.105 \frac{mc}{hA} \\ e^{(-hA/mc)t_2} = 0.1 &\Rightarrow t_2 = 2.303 \frac{mc}{hA} \end{aligned} \right\} \Rightarrow \tau = t_2 - t_1 = 2.198 \frac{mc}{hA} \quad (5.6)$$

From Equation (5.6), we can see that the rise time depends on the thermal properties of the sensing element material, its dimensions and mass. These factors set the ultimate limitation on the frequency response of the sensor.

Usually, the three types of heat transfer mechanisms, including conduction, convection and radiation, transfer thermal energy to the sensing element with different rates. As discussed in addressing the hysteresis of the system, the heat transfer mechanisms between the sensing element and the environment are mainly convection and radiation in a coal gasifier. Convection heat transfer is dominant from room temperature up to several hundred degrees Celsius, while the radiation and convection heat transfer will co-exist at high temperature levels. Thus, the frequency response of the sensor will thus be faster at high temperature levels than at low temperature levels.

The frequency response of the BPDI sensing system also depends on the signal processing time on the optical temperature signatures. The signal processing time of the

signal processing unit, which is composed of an optical spectrometer and a computer in the BPDI sensor system, is determined by the data sampling frequency, time delay between each electrical scan, and the boxcar width used to smooth the spectral curves, as well as the speed of digital signal processing in the computer.

It is difficult to predict the rise time of the sensor theoretically by taking all these three factors into account. Instead, experimental tests are carried out to measure the rise time of the sensor system. The probe and the sensing element are single crystal sapphire material, and the thickness of the protection tube is 3.0mm with 25mm inner diameter. The sensing element is a right-angle prism with a base size of $8\text{mm}(\text{width}) \times 25\text{mm}(\text{length})$. In the optical spectrometer, the data sampling frequency is 100Hz, and time delay between each scanning is 3ms. The boxcar width is 5 pixels for the spectral curves smoothing. The computer is a Pentium II desktop with a CPU frequency of 300MHz.

The first test was performed in a boiling water bath. The sensor and the thermocouple for temperature reference, are kept at room temperature (26.5°C), then inserted into the boiling water (95.4°C) instantly while the water was kept boiling to maintain its temperature, the temperature change can then be approximated as a step function from 26.5°C to 95.4°C , the temperature increasing process was monitored and plotted in Figure 5.24. The rise time can then be determined from these curves. The rise time for the thermocouple is 3.19 seconds, and is 153.96 seconds (2.6 minutes) for the single crystal sapphire optical sensor. The heat transfer mechanisms in the boiling water are mainly convection and conduction.

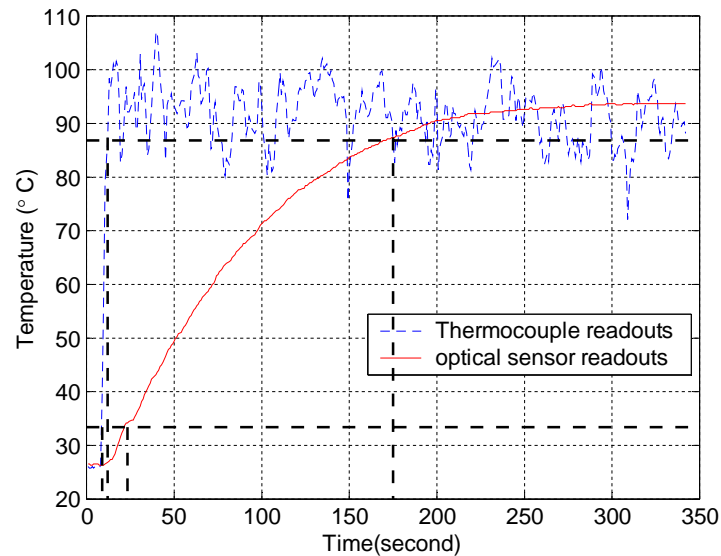


Figure 5.24. Rise time characterization of the BPD sensor system with boiling water

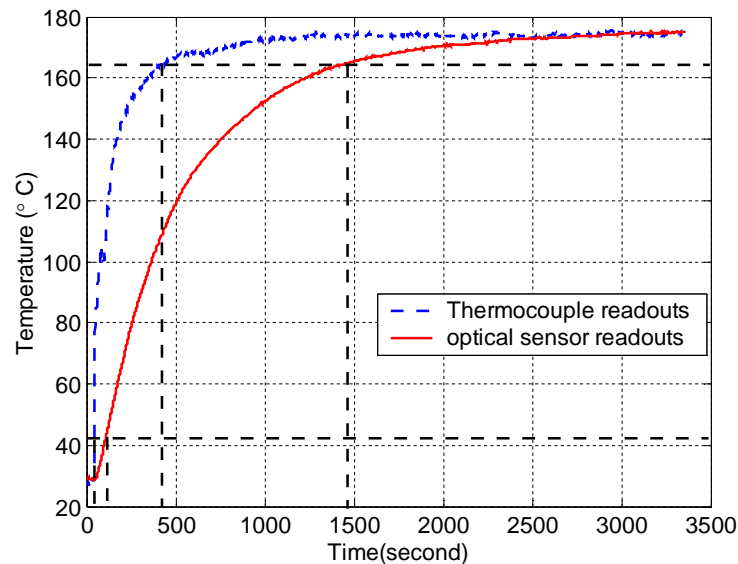


Figure 5.25. Rise time characterization of the BPD sensor system with high temperature furnace

The second test was performed in a high temperature furnace, which is closer to the environment in an actual coal gasifier. Here the dominant heat transfer mechanism is convection at the tested temperature level of 174.4°C. The step change of the temperature is from 26.5°C up to 174.4°C, as shown in Figure 5.27. The rise time for the reference K-type thermocouple is 305.65seconds (about 5 minutes), and the rise time for the single crystal sapphire optical sensor is 1133.01 seconds (about 19 minutes).

Chapter 6 Expansion of the BPDI sensing technology for other measurements

This chapter presents several different sensor designs and testing results using the BPDI technology, including a pressure sensor, an angular rotation sensor, and an electrical voltage sensor.

6.1 Multi-parameter measurement toolbox based on optical birefringence

In the broadband polarimetric differential interferometric (BPDI) sensing technology, when a broad spectrum linearly polarized light passes through a polarimeter, the state of polarization (SOP) of the light is modulated by a sensing element. The output light becomes a wavelength-encoded signal, which can be detected directly by an optical spectrometer. This wavelength-encoded signal is actually the signature of the optical path difference (OPD) between the two orthogonal linearly polarized light beams propagating inside the sensing element. By relating the OPD to the measurands of interest through calibrations, the measurements of multi-parameters, such as pressure, rotary displacement, electrical current/voltage, and materials characterization can be realized. The sensing schemes are really rooted in the sensitivities of the birefringence and dimensions of the sensing element to these parameters through corresponding physical, chemical or biological phenomena.

With the other existing technologies, most of the physical, chemical and biological parameter measurements are usually carried out in the separate systems, and each measurement system has its own signal-processing unit. Measurement schemes are usually quite different. By simply changing the sensing elements, the BPDI sensing system, with its self-calibration capability associated with the optical polarimetric characteristics and the spectral domain signal processing method, could be employed to measure several parameters, with high resolution, great accuracy, and long-term stability.

The chief advantages of this measurement toolbox are its simplicity and compactness. By changing different sensing elements, the same system setup (optical source, and signal processing unit) for the BPD temperature sensing system described in Chapter 3, can be used for multi-parameters measurements, either in a one-end portable structure, where a 45-45-90 degree cubic prism is used to reflect light back from the end of the sensing head, and only one optical polarizer is used to work both as polarizer and polarization analyzer, as shown in Figure 6.1, or in a two end structure, where two optical polarizers are used, and the sensing element is sandwiched between them, as shown in Figure 6.2.

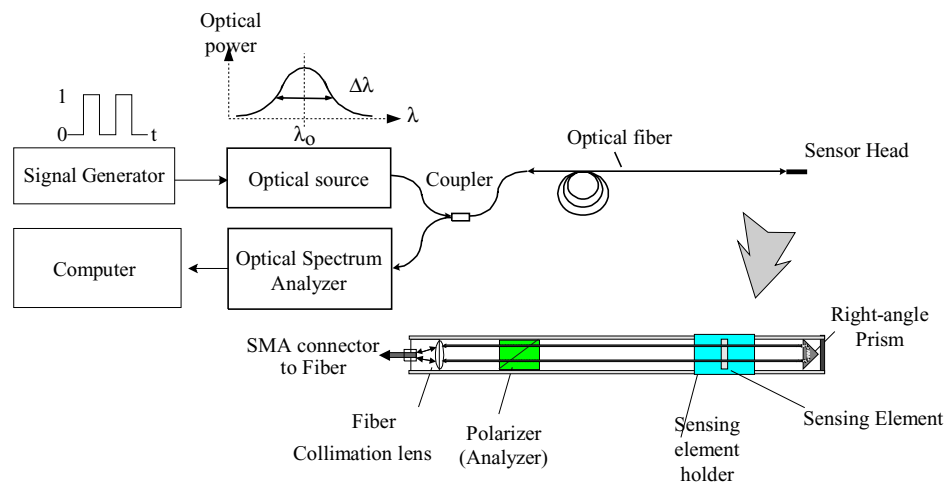


Figure 6.1 An one-end structure version BPD sensor system

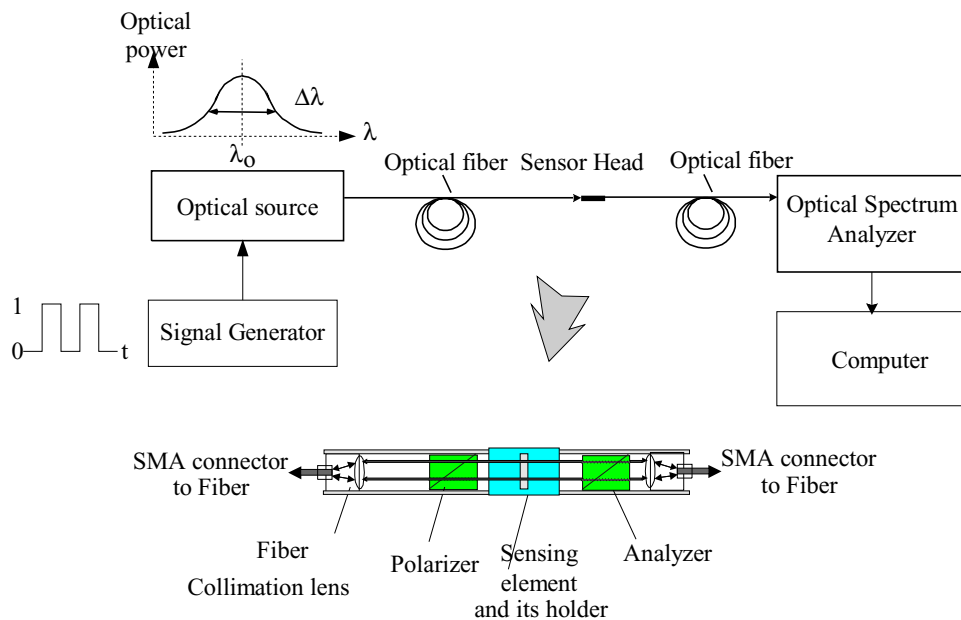


Figure 6.2. A two-end structure version BPD sensor system

6.2 Pressure sensor with temperature compensation capability

Most conventional optical pressure sensors are based on movable diaphragms, small Fabry-Pérot interferometers, or fiber micro-bendings. The problem with these pressure sensors is often the high cross-sensitivity with temperature. The pressure measurement based on photoelastic phenomena has been proposed and tested [70], in which the pressure generates or changes the birefringence. At the same time, the dimensions of the sensing element also varies if the surrounding pressure changes, thus the OPD is uniquely related to the integrated effects from the changes of both the birefringence and the dimensions of the sensing element, all related to the surrounding pressures. The BPDI sensor system interrogates the optical signal by directly detecting the spectrum instead of optical intensity, which provides immunity to the optical source fluctuation and transmission losses, thus high stability can be achieved.

By redesigning the structure of a sapphire temperature sensor head, the pressure-birefringent polarization-based pressure sensors with temperature compensation capability can be obtained. This new design provides temperature compensation capability by utilizing a birefringent sapphire prism as a sensing element. A birefringent sapphire disk is used as a temperature compensator outside the pressure environments. By positioning these two sapphire elements closely and aligning the fast axis of the temperature compensator parallel to the slow axis of the pressure transducer, temperature sensitivity of the system can be fully compensated by the temperature compensator with a proper size.

Preliminary tests were carried out to test the pressure sensor. The schematic setup of the sensing head is shown in Figure 6.3. One sapphire prism is put in a pressure chamber and a white-light system is used to monitor the OPD changes caused by the pressure. As shown in Figure 6.4 and Figure 6.5, there is a unique relation between the pressure and the photoelasticity generated OPD in the single crystal sapphire sensing element. Figure 6.6 shows the calibrated pressure sensor measurement results.

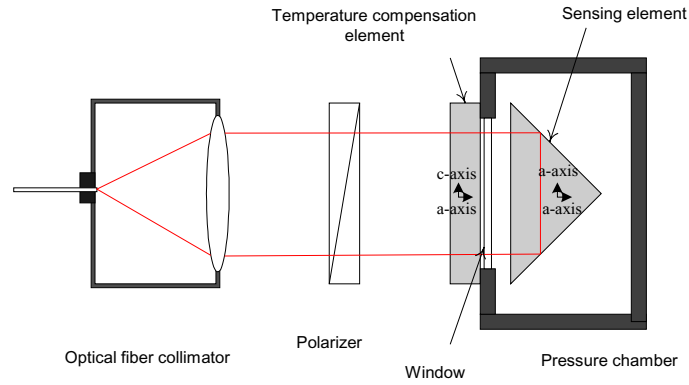


Figure 6.3 Schematic design of BPD based optical single crystal sapphire high-pressure sensing head

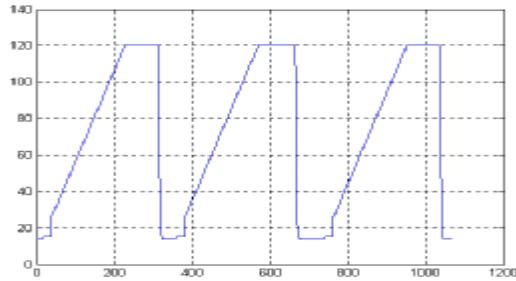


Figure 6.4. Applied pressure signals on the sapphire sensing element

X-axis: sampling points, function of time.

Y axis: pressure values (Unit: psi)

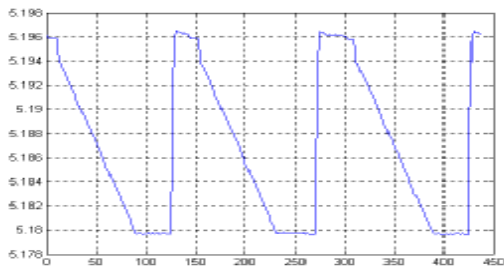


Figure 6.5. Pressure signals from the optical sensor

X-axis: sampling points, function of time.

Y axis: optical path difference (Unit: micron)

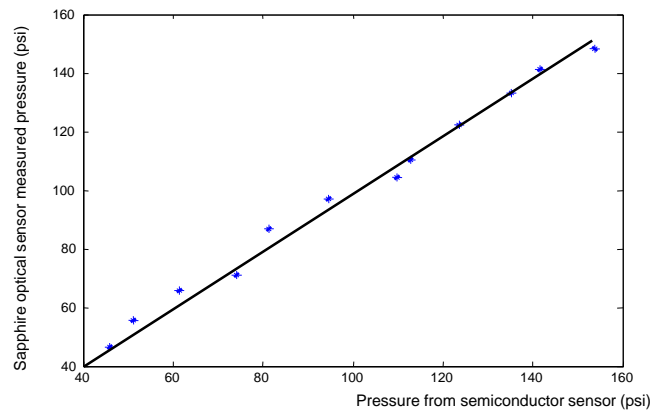


Figure 6.6. Pressure measurements with the calibrated sapphire pressure sensor

6.3 Rotary displacement sensor

Spillman reported the rotary displacement sensor based on an optical retardation plate [71]. When a retardation plate is sandwiched between two polarizers and rotates along its fast axis, a “notch” intensity minimum is created in the broadband input optical signal. The wavelength position of the notch in the detected spectrum envelope is related to the rotation angle. This reported sensing scheme utilizes only one notch in the spectral curve, which is determined by the intensity minimum. When the rotation angle changes, the notch will move in the spectral curve. The measurement range of the rotary displacement will be limited by the bandwidth of the optical source and the optical spectrometer measurement range. The accuracy and resolution of the rotary displacement measurement are limited by the optical source drift, optical fiber modulation, etc.

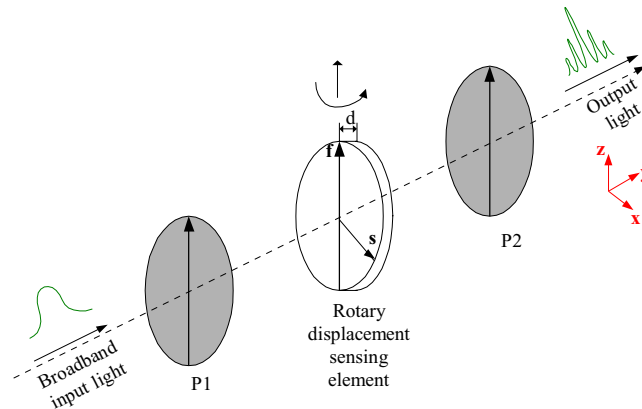


Figure 6.7. Fiber Optic rotation sensor

In the BPDI sensor system, the wavelength modulation produced by the rotated retardation plate is identical to that produced by the temperature sensor. In the rotation sensor, the rotation of a retardation plate about its optical axis (fast or slow axis) rather than the thermal expansion, produce the same effects in the sensing element. With a proper thickness of the retardation plate, several optical minima and maxima can be generated simultaneously in the spectrum envelop of the broadband input optical signal. The BPDI sensor utilizes these special points in the spectral curves instead of one notch, so high resolution and accuracy can thus be achieved because of its self-compensation capability to optical source center wavelength drift and bandwidth

changes, as well as fiber transmission losses. The rotation displacement measurement range is not limited by the measurement range of the optical spectrometer measurement range. Based on a single crystal sapphire disk with a thickness of 1.5mm as a sensing element, a preliminary sensor was constructed and tested. Figure 6.8 shows the rotation angle measurement results.

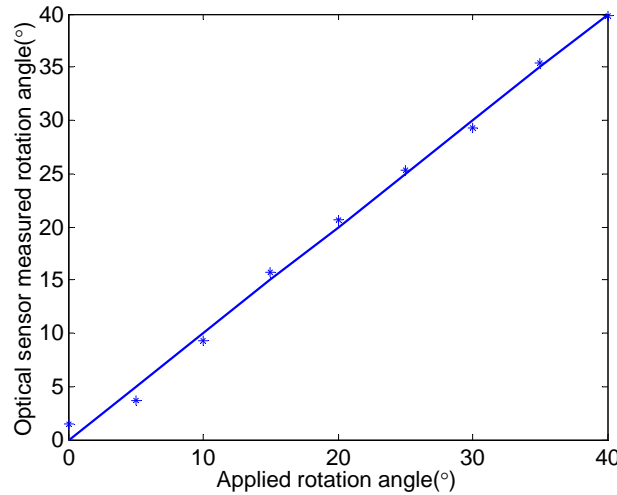


Figure 6.8. Rotation angle measurements with the calibrated fiber optic rotation sensor.

6.4 High electrical voltage sensor

When an electro-optic crystal is exposed to an electric field, polarization states of light in the electrooptic crystal will be changed due to the Pockels effect or the Kerr effect. The BPDI sensing technology can also be applied to the electrical voltage measurement by selecting an appropriate sensing element. Preliminary tests were carried out with a single crystal lithium niobate by utilizing its Pockels effect, which is the linear electro-optic effect in the crystal.

As shown in Figure 6.9, in the presence of an electric field along the x-axis, the refractive index ellipsoid of the lithium niobate becomes [44]:

$$\frac{x^2}{n_x^2} + \frac{y^2}{n_x^2} + \frac{z^2}{n_z^2} + 2r_{51}E_xxz + 2r_{61}E_xxy = 1 \quad (6.1)$$

where $r_{51} = 28, r_{61} = 6.8$ for low frequency electrical signals. The electric field generates birefringence in the x-y plane. The magnitude of the induced birefringence depends on the electric field according to:

$$\Delta n = n_o^3 r_{61} E_x \tag{6.2}$$

A piece of lithium niobate with dimensions of $x(9mm) \times y(9mm) \times z(25mm)$ is used for the electric voltage measurement. To minimize the temperature effect and pyroelectric effect in the crystal, the electric field is applied in the x-axis and the light propagates along the z-axis [72]. The electrical voltage was measured up to 10KV and results are shown in Figure 6.10.

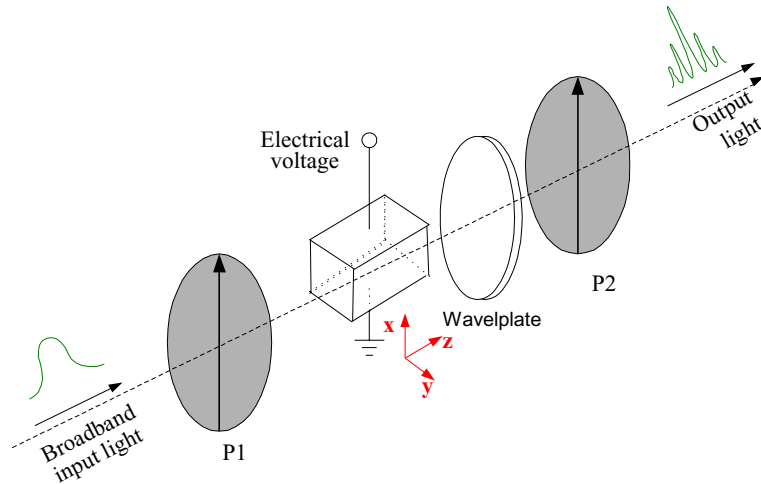


Figure 6.9. Sensing head designs for electrical voltage measurement.

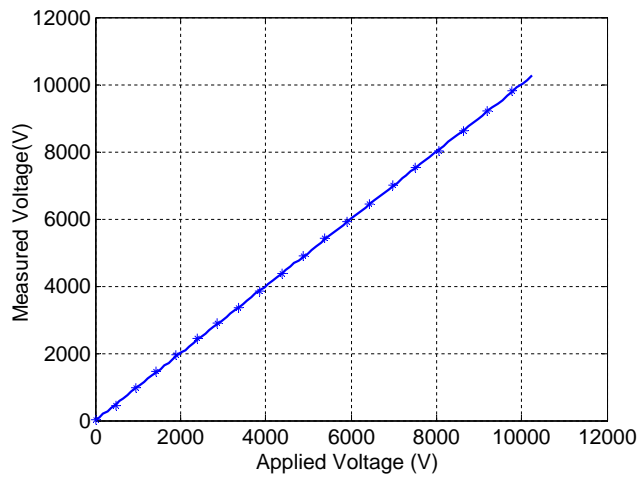


Figure 6.10. Electrical voltage sensor based on the BPDI technology.

Chapter 7 Conclusions and recommendations for future work

By incorporating a spectrometer with a polarimeter for the purpose of measuring polarization properties as a function of optical wavelengths, an optical broadband polarimetric differential interferometric (BPDI) sensing technology was developed in this research. It has been applied for temperature measurement and proven to be able to provide reliable self-calibrating measurement of temperatures up to 1600°C with excellent repeatability, as well as high resolution. This optical sensing technology possesses many advantages, such as wide dynamic measurement range, intrinsic immunity to electromagnetic interference (EMI), high sensitivity, simplicity and especially long-term stability in harsh environments.

This chapter summarizes the major conclusions obtained during the research. Future research work to further improve the system performance are also outlined in this chapter.

7.1 Conclusions

In this research work, an optical broadband polarimetric differential interferometric (BPDI) temperature sensor system was proposed and tested using single crystal sapphire material, which possesses a high melting temperature (over 2000°C), superior optical transparency, and ability to resist chemical corrosions. With a simple mechanically-structured sensing probe, in conjunction with an optical spectrum-coded interferometric signal processing technique, the single crystal sapphire optical sensor can potentially measure high temperature in harsh environments with great accuracy, corrosion resistance and long-term measurement stability. Contrary to intensity based optical sensing schemes, spectrum measurement based BPDI sensor system encodes temperature information in the wavelength of an optical signal, which is then decoded by an optical spectrometer; this sensor guarantees that encoded spectrum data is not corrupted by intensity fluctuations in the optical signals.

Due to the crystallographic arrangement of atoms in single crystal sapphire, the material exhibits an inherent birefringence: the propagation speeds of light in the crystal are different depending on their polarization directions. The BPDI sensing system provides absolute measurement of the optical path difference (OPD) between two orthogonal linearly polarized light beams in the single crystal sapphire used as a sensing element. The OPD values are determined by the birefringence and the dimensions of the sapphire sensing element. Since both the birefringence and the dimensions of the sensing element are temperature dependent, OPD values can be related to temperature by calibration. The mathematical models of the sensor in response to the temperature have been studied in order to provide guidelines for optimal design of the sensor.

Detailed implementation of the BPDI sensing system has been described, including signal processing unit and sensing probe assembly. High performance sensor probes integrate a sensing element and an optical polarizer/analyzer with a fiber collimator to form a compact unit, thus the mechanical stability is improved. The sensing head can either be a SP structure including one right-angle Sapphire Prism with a special crystallographic orientation, acting both as a sensing element and as a light reflector, or a SDZP structure including a single crystal Sapphire Disk (as a sensing element) and a right-angle single crystal Zirconia Prism (as a light reflector). A single crystal sapphire tube is employed to protect the sensing element and hence increase its survivability in harsh environments. Testing results show that the sensor probe exhibits excellent reliability and stability needed to survive the high temperature (up to 1600⁰C) environments. Spectral domain white light interferometry was employed to interrogate optical temperature signature in real-time. The integration of white light interferometry signal processing scheme and the specially designed single crystal sapphire sensor probe augment the sensor's survivability when operating in the harsh environments.

In order to achieve all the potential advantages of the BPDI technology, a detailed noise analysis has been presented to gain a better understanding of the performance limitation of the BPDI sensor system. The optical noise analysis of the system identifies the largest error results from the rotation of the sensing element relative to the optical polarizer. The

optical noise analysis also indicates that the change of the spectral characteristics of the optical source, such as spectrum wavelength drift and bandwidth broadening/narrowing contributes to the error of the system. The fiber bending induces spectrum wavelength shift and bandwidth changes that can affect the system performance as well. The optoelectronic noise analysis indicates that the $1/f$ noise and the thermal noise together form the ultimate limit on the optical spectrometer performance.

Based on the system noise analysis results, optimization of measurement techniques is suggested to improve the system performance. The algorithm used to perform the signal demodulation and the OPD calculations are optimized to compensate the error due to spectrum changes and the optoelectronic noises.

Comprehensive experiments have been performed to systematically evaluate the performance of the optical signal processing unit and the sensor system, including measurement repeatability and accuracy, long-term system stability, measurement resolution, self-calibration capability, hysteresis, and frequency response. Measurement repeatability of $\pm 2.5^\circ\text{C}$ was obtained. The measurement accuracy is about $\pm 6^\circ\text{C}$. By keeping the sensor head at certain temperature levels for a relatively longer time period, the long-term drift, which is the deviation of the temperature readouts from the designed optical temperature measurement system compared to the thermocouple readouts, were evaluated to be within the range of $\pm 2^\circ\text{C}$. Resolution of the system was estimated to be about 0.07°C . The excellent self-calibration capability of the system was tested, which proves that the system is relatively immune to transmission fiber losses, optical source power fluctuations and spectrum distortions. For high temperatures over 1200°C the hysteresis of the BPDI sensor system is negligible. The rise times of the system are also evaluated on two different temperature levels.

In conclusion, the BPDI sensor system offers the following major advantages over other sensors designed for the high temperature applications:

1. BPDI technology extracts absolute temperature information by absolute measurement of phase delays between two orthogonal linearly polarized light

waves, which is more attractive for applications in harsh environments, because of no requirement of initialization and recalibration when power is switched on and off.

2. The BPDI optical temperature measurement system takes advantages of both fiber optics and bulk optics to simplify the design of the sensing head. Bulk optics is convenient for reducing the required tolerances on optical alignment and also for reducing the sensitivity to mechanical vibrations. The optical fibers can transmit light over a long distance with small attenuation and can be easily implemented in industrial environments because of their small size, light weight and immunity to electromagnetic interference (EMI).
3. The BPDI sensor system offers high measurement resolution (better than 0.1°C) because of its intrinsic interferometric characteristics.
4. The BPDI sensor system monitors temperatures in real-time through measuring optical spectrum instead of optical intensity. This guarantees its relative immunity to optical source power fluctuations and fiber transmission losses, thus providing a high degree of long-term measurement stability.
5. The BPDI temperature sensor provides a wide dynamic measurement range. It was tested from room temperature up to over 1600°C .

7.2 Suggestions for future works

A complete and systematic performance evaluation of this sensor provides feedback information for further improving the system design. Based on the work done so far, future works are suggested to further enhance the robustness and reliability of the BPDI temperature sensor systems, to achieve the final goal of conducting accurate temperature measurements in practical harsh environments, especially in the coal gasifier. An outline of further investigation is given below.

1. Sensor protection

Temperature, pressure, and harsh chemicals are commonly used in the industrial processes; however, they degrade conventional sensor probes quickly. Temperature-related degradation mechanisms include: thermal shock, thermal cycling, thermal stress, thermal fatigue, and high heat fluxes. All of these factors must be considered in the elevated temperature environments.

For the temperature measurement in the coal gasifier, although the corrosion resistance of the single crystal sapphire material has been documented by laboratory testing, special consideration should be given to the required mechanical protection of both the sensor probe and the associated signal demodulation system, since the sensor probe is subjected to the extreme mechanical stress when the gasifier is heated up from room temperature to 2800F. The same stresses will also be experienced when the gasifier is shutting down and cooling down. If the sensor needs to be retrieved, it needs to be designed to handle the shutdown as well as heatup processes. An ideal sensor probe should contain an inexpensive and rugged shell, marginally larger than the probe. The shell can be made of high temperature metals for the mechanical stress protection on the inner sensing element and housing tube.

2. Sensor assembly

The sensor probe material not only has to survive the environment, but also it has to be compatible with the thermal expansion of the inside sensing element and the joining or sealing techniques. An optical probe must consist of a corrosion-resistant body hermetically sealed to a sapphire sensor head, so that the sapphire sensor head can be physically exposed inside the coal gasifier for temperature measurements. The whole probe design and assembly must address the problem of the operating temperature and heat flux to the sensing element. Other concerns are the operating temperature of the probe, the internal diameter of the probe, and the outside diameter of the envelope shell. External constraints consist of the port size in the refractory wall of the coal gasifier

chamber, directness of the access, reactivity and temperature of the environments, period of use, and other optical requirements.

In order to install the designed sensing system in the coal gasifier, slagging conditions at the temperature measurement points, length into the hot zone, width of the refractory wall, and location of electronics, need to be specified for the system integration with the existing coal gasification facility.

3. Improvement of the signal processing in digital domain

The performance of the BPDI sensor system can be further improved with filtering techniques in the digital domain by the host computer. Digital filters can be implemented to reduce the blackbody radiation background noise. The electronic noise associated with the spectrum measurements can also be minimized with digital filtering techniques, thus the temperature measurement accuracy and resolution can be improved.

4. Field evaluation

Based on the requirements of industrial fields, a complete field test of the system is necessary to comprehensively evaluate the overall performance of the BPDI sensor system. The field test results should also serve well to further optimize the sensor and system design for the successful commercialization of the BPDI sensing technology.

For the field tests, consideration of the required environmental performance in a slagging gasifier was a prime concern in the design of the optical sensor components, which must physically reside in the gasification unit. The sensor instrumentation should be made for continuous operation in an actual coal gasification facility under high temperatures and extremely corrosive conditions. The field test should run for multiple months in order to be able to reliably demonstrate the capability of the operation in extremely harsh gasification environments.

Reference

1. E. Udd, *Fiber optic sensors: an introduction for engineers and scientists*, John Wiley & Sons, Inc., 1991.
2. R. Baierlein, *Thermal physics*, Cambridge University Press, 1999.
3. E. Magison, "Temperature measurement-physical principles underlie the four common methods," *Industrial temperature measurement*, November 2001, pp: 39-41
4. R. E. Bentley, "Temperature and humidity measurement," *Handbook of temperature measurement*, vol 1, Singapore; New York : Springer, 1998
5. L. C. Lynnworth and E. H. Carnavale, "Ultrasonic thermometry using pulse techniques," In H. H. Plumb, editor, *Temperature: its measurement and control in science and industry*, vol 4, Inst. Soc. America, Pittsburgh, 1972, pp: 715-732.
6. D. W. Varela, "Temperature measurement in industrial and laboratory furnace using ultrasonic thermometry," In J. F. Schooley, editor, *Temperature: its measurement and control in science and industry*, vol 6, Amer. Inst. Phys. New York, 1992, pp: 1027-1032.
7. S. F. Green, "Acoustic temperature and velocity measurement in combustion gases," *8th Int. Heat Transfer Conf.*, San Francisco, August 1986
8. S. M. Vaezi-Nejad, "Selected topics in advanced solid state and fiber optic sensors," Published by the Institute of Electrical Engineers, London, United Kingdom. 2000, *IEE circuits, devices and systems* series 11.
9. D. P. Dewitt and G. D. Nutter, *Theory and practice of radiation thermometry*, John Wiley&Sons, Inc. New York, 1988.
10. R. R. Dils, "High-temperature optical fiber thermometer," *J. Appl. Phys*, 54(3), March 1983, pp: 1198-1201.
11. B. E. Adams, "Optical fiber thermometry for use at high temperatures," In J. F. Schooley, editor, *Temperature: its measurement and control in science and industry*, vol 6 Amer. Inst. Phys. New York, 1992, pp: 739-743.

12. R. O. Claus, M. F. Gunther, A. Wang, K. A. Murphy, "Extrinsic Fabry-Perot sensor for strain and crack opening displacement measurement from -200 to 900 °C," *J. of Smart Materials and Structures*, vol 1, no.3, 1992.
13. H. Xiao, J. Deng, R. May, and A. Wang, "Single crystal sapphire fiber-based sensors for high-temperature applications," *Proc. SPIE 3201*, Bonston, MA, September 19, 1999.
14. M. Sun, "Fiberoptic thermometry based on photoluminescent decay times," In J. F. Schooley, editor. *Temperature: its measurement and control in science and industry*, vol 6, Amer. Inst. Phys, New York, 1992, pp: 715-719.
15. Z. Zhang, K.T.V. Grattan, and A.W. Palmer, "Fiber-optic high temperature sensor based on the fluorescence lifetime of alexandrite," *Rev. Sci. Instrum.*63, 1992, pp: 3869-73.
16. B. W. Noel, W.D. Turley, W. Lewis, K. W. Tobin, and D. L. Beshears, "Phosphor thermometry on turbine-engine blades and vanes," In J. F. Schooley, editor. *Temperature: its measurement and control in science and industry*, vol 6, Amer. Inst. Phys, New York, 1992, pp: 1249-54.
17. K. A. Wickersheim, and M. H. Sun, "Fiberoptic thermometry and its applications," *J. Microwave. Power.* 22(2) 1987, pp: 85-94.
18. O. Iida, T. Iwamura, K. hashiba, and Y. Kurosawa, "A fiber optic distributed temperature sensor for high-temperature measurements," In J. F. Schooley, editor. *Temperature: its measurement and control in science and industry*, vol 6, Amer. Inst.Phys, New York, 1992, pp: 745-749.
19. A. B. Murphy and A. J. D. Farmer, "Temperature measurement in thermal plasma by rayleigh scattering," *J. Phys. D: Appl. Phys.*, 25, 1992, pp: 634-43.
20. A. B. Murphy, "Laser-scattering temperature measurements of a free burning arc in nitrogen," *J. Phys. D: Appl. Phys.*, 27, 1994, pp: 1492-1498.
21. J. P. Dakin, D. J. Pratt, G. W. Bibby, and J. N. Rosss, "Distributed optical fiber Raman temperature sensor using a semiconductor light source and detector," *Electron. Lett.* 21: 1985 pp: 569-570.
22. H. D. Schilling, B. Bonn, and U. Krauss, *Coal gasification: existing processes and new developments*, [2nd rev. ed.], London, Graham & Trotman, 1981.

23. E. J. Hoffman, *Coal gasifiers*, Laramie, Wyo. Energon Co., 1981.
24. M. R. Werner, and W. R. Fahrner, "Review on materials, microsensors, systems, and devices for high-temperature and harsh-environment applications," *IEEE trans. Ind. Electron.*, vol. 48, no. 2, April 2001, pp: 249-257.
25. J. R. Leigh, *Temperature measurement and control*, Chapter 5, Perter Peregrinus Ltd, London, United Kingdom, 1988
26. G. B. Lu, and H. C. Yan, "Concurrent measurements of temperature and soot concentration of pulverized coal flames," *Instrumentation and Measurement Technology Conference*, 2001. IMTC 2001. Proc. the 18th IEEE, vol.2 pp: 1221 – 1226.
27. J. Castrellon, G. Paez, and M. Strojnik, "Radiometric analysis of a fiber optic temperature sensor," *Opt. Eng.* Vol. 41 No. 6, June 2002, pp: 1255-1261.
28. K. M. Koo, J. H. Kim, S. B. Kim, H. D. Kim, and D. Y. Ko, "Ultrasonis thermometry system for measuring very high temperatures using high resolution signal processing," *Proc. IECIC 2001*, Aug 2001.pp: 229-232.
29. E. P. Hastie, and D. Bonnell, "Alkali Vapor Transport in Coal Conversion and coal combustion systems," ACS Symposium Series, vol. 179 *Metal bonding and interactions in high temperature systems with emphasis on alkali metals* (1982)
30. T. Sun, "Alkali corrosion of ceramic materials", *Ceramic News*, 2(4)1-2, 1991
31. J. Schlichting, "Oxidation and hot corrosion behavior of SiN and SiAlON," *Nitrogen ceramics*, Edited by F. L. Riley. Noordhoff, Leyden, 1977, pp: 627-632.
32. J. Smialik and N. Jacobson, "Mechanism of strength degradation for hot corrosion of alpha-SiC," *J. Am. Ceram. Soc.* 59(10), 1986, pp: 741-752.
33. M. Feber, J. Ogle, V. Tennery and T. Henson, "Characterization of corrosion mechanisms occurring in a sintered SiC exposed to basic coal slags," *J. Am. Ceram. Soc.* 68(4), 1985, pp: 191-197.
34. M. Feber and V. Tennery, "Behavior of tubular ceramic heat exchanger materials in acidic ash from coal-oil-mixture combustion," *Ceram. Bull.*, 62(2), 1983, pp: 236-243.
35. D. Mckee and D. Chatterji, "Corrosion of silicon carbide in gases and alkaline melts," *J. Am. Ceram, Soc* 59(9-10), 1976, pp: 441-444.

36. T. Sun, *Alkali corrosion of coal gasifier linings*, Master's thesis, Virginia Polytechnic Institute, 1986
37. M. V. Roode and J. Price, "Corrosion resistant coatings for ceramic heat exchanger tubes operating in highly corrosive environments," *in high performance ceramic coatings and films*, published by Elsevier Science Publishers, 1991, pp: 625-633.
38. G. R. Pickrell, *High Temperature Alkali Corrosion of Low Expansion Ceramics*, Ph.D. Dissertation, Virginia Tech, 1994
39. A. Dandridge and A. D. Kersey, "Overview of Mach-Zehnder sensor technology and applications," *Proc. SPIE 985*, Fiber Optic and Laser Sensors VI, Boston, Sept. 1988
40. A. Wang, S. Gollapudi, R. G. May, K. A. Murphy, and R. O. Claus, "Sapphire optical fiber-based interferometer for high temperature environmental applications," *J. of Smart Materials and Structures*, 4, 1995, pp: 147-151.
41. A. Wang, S. Gollapudi, K. A. Murphy, R. G. May, and R. O. Claus, "Sapphire-fiber-based intrinsic Fabry-Perot interferometer" *Opt. Lett.* vol. 17, no. 14, 1992, pp:1021-23.
42. J. Schellman and H. P. Jensen. "Optical spectroscopy of oriented molecules," *Chem. Rev.* 87, 1987, pp: 1359-1399.
43. D. S. Kliger, J.W. Lewis, and C.E. Randall. *Polarized light in optics and spectroscopy*, Academic Press, Boston, 1990
44. A. Yariv, *Optical electronics in modern communications*, Chapter 1, Oxford, 1997
45. K. A. Murphy, M. F. Gunther, A. M. Vengsarkar, and Richard O. Claus "Quadrature phase shifted extrinsic Fabry-Perot fiber optic sensors", *Opt. Lett.* vol. 16, 1991, pp: 273-275.
46. D. A. Jackson, et al, "Pseudo-heterodyne detection scheme for optical interferometers", *Electron. Lett.* Vol. 28, 1982, pp: 1081-1083.
47. D. Hogg, D. Janzen, T. Valis, and R. M. Measures, "Development of a fiber Fabry-Perot (FFP) strain gauge," *Proc. SPIE vol. 1588*, 1991, pp: 300-307.

48. G. Stewart,; A. Mencaglia, W. Philp, and W. Jin, "Interferometric signals in fiber optic methane sensors with wavelength modulation of the DFB laser source," *J. Lightwave. Technol.* vol. 16, no.1, 1998, pp: 43-53.
49. T. K. Gangopadhyay and P. J. Henderson, "Vibration: history and measurement with an extrinsic Fabry-Perot sensor with solid-state laser interferometry," *Appl. Opt.* vol. 38, No.12, Apr., 1999, pp: 2471-2477.
50. A. Wang, H. Xiao, J. Wang, Z. Wang, W. Zhao, and R. G. May, "Self-calibrated interferometric/intensity-based optical fiber sensors," *J. Lightwave. Technol.* vol. 19, no. 10, 2001, pp:1495-1501.
51. S. A. Al-Chalabi, B. Culshaw, and D. E. N. Davies, "Partially coherent sources in interferometry," *Proc. 1st int conf optical fiber sensors*, London, 1983, pp: 132-135.
52. T. Bosselman, and R. Ulrich, "High accuracy position-sensing with fiber-coupled white light interferometers," *Proc. 2nd int conf optical fiber sensors*, Stuttgart, 1984, pp: 361-365.
53. J. G. Proakis and D. G. Manolakis, *Digital signal processing*, third edition, Prentice-Hall, 1996.
54. D. N. Nikogosyan, *Properties of optical and laser-related materials: a handbook*, Chapter 1. Chichester, England; New York : J. Wiley, 1997.
55. R. C. Jones, "New calculus for the treatment of optical systems," *J. Opt. Soc. Am* 31, 1941, pp: 488-495.
56. D. C. Harris, *Materials for infrared windows and domes*, SPIE Press, Bellingham WA, 1999
57. M. Bass, *Handbook of optics-fundamentals, techniques& design*, second edition, vol II. Sponsored by the OSA. McGraw-Hill, 1995.
58. J. B. Wachtman, Jr. and L.H. Maxwell, "Strength of synthetic single crystal sapphire and ruby as a function of temperature and orientation," *J. Am. Ceram. Soc.* 42, 1959, pp: 432-433.
59. R. L. Gentilman, E. A. Maguire, H.S. Starrett, T.M. Hartnett and H.P. Kirchner, "Strength and transmittance of sapphire and strengthened sapphire," *J. Am. Ceram. Soc.* 64, 1981, pp:116-117.

60. J. W. Fischer, W. R. Compton, N. A. Jaeger and D. C. Harris, "Strength of sapphire as a function of temperature and crystal orientation." *Proc. SPIE. 1326*, 1990, pp:11-22.
61. D. C. Haris and L.F. Johnson, "Navy mechanical test results from the sapphire statistical characterization and risk reduction program," *Proc, SPIE 3705*, 1999, pp: 44-50.
62. D. C. Harris, "Overview of progress in strengthening sapphire at elevated temperature," *Proc, SPIE 3705*, 1999, pp: 2-11.
63. F. Schmid, K. A. Schmid, C. P. Khattak, and P. Duggan, "Increase of the strength of sapphire by heat treatments," *Proc, SPIE 3705*, 1999, pp:36-43.
64. F. Schmid, C. P. Khattak, K. A. Schmid, and S. G. Ivanova, "Increase of high temperature strength of sapphire by polishing, heat treatments and doping," *Proc, SPIE 4102*, 2000, pp:43-51.
65. S. P. Bush and D. A. Jackson, "Numerical investigation of the effects of birefringence and total internal reflection on Farady effect current sensors". *Appl. Opt.* vol 31, No25. Spetember 1992, pp: 5366-5374.
66. B. Qi, G. Pickrell, et al. "High-resolution white light interferometer and its application". Submitted to *Opt. Eng.* SPIE.
67. J. P. Holman, *Experimental methods for engineers*, 6th edition, McGraw-Hill Inc. 1994
68. A. Tapia-Mercado, J. Khomenko, A.V. Garcia-Weidner, "Precision and sensitivity optimization for white-light interferometric fiber-optic sensors," *J. Lightwave. Technol.* Vol: 19 no:1, 2001, pp: 70 -74.
69. A. Wang, S. He, X. Fang, X. Jin, J. Lin, "Optical fiber pressure sensor based on photoelasticity and its application." *J. Lightwave. Technol.* Vol 10, no.10, 1992, pp1466-1470.
70. W. B. Spillman, Jr. P. L. Fuhr, and P. J. Kajenski, "Fiber optic rotary displacement sensor with wavelength encoding," *Appl. Opt.* 27 (15) 1988, pp: 3081-3085.
71. S. C. Abrahams, *Properties of lithium niobate*, London; New York: INSPEC, Institution of Electrical Engineers, 1989.

Appendix A: Determination of the refraction angle and refractive index corresponding to the extraordinary waves in the single crystal sapphire

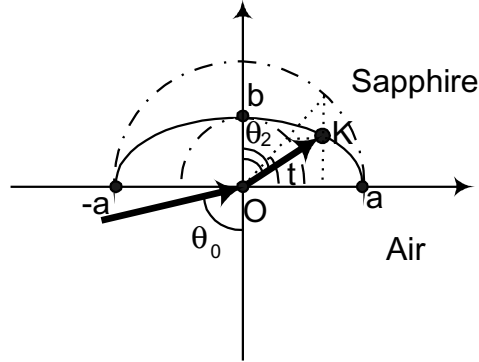


Figure 1. Light wave refraction at the surface of the A-plane cut single crystal sapphire

When light propagates at the interface of air and a single crystal sapphire with inherent birefringence (A-plane cut), the refractive index of the extraordinary wave inside the single crystal sapphire will depend on the incident angles. Shown in Figure 1, for light incident with an angle θ_0 , the refraction angle is θ_2 and the magnitude of refraction index is $|OK|$, it follows the Snell's law,

$$\sin^2 \theta_0 = |OK|^2 \sin^2 \theta_2 \quad (1)$$

Within the half ellipse (arc $-a-b-a$), the length of line OK is:

$$\left. \begin{aligned} X_K &= a \cos t \\ Y_K &= b \sin t \end{aligned} \right\} \text{cooriantes for the } K \text{ point} \quad (2)$$

$$|OK|^2 = a^2 \cos^2 t + b^2 \sin^2 t$$

Where t is an intermediate variable with no physical meanings. According to the simple trigonometric function, the relationship between t and θ_2 is:

$$\tan \theta_2 = \frac{X_K}{Y_K} = \frac{a \cos t}{b \sin t} = \frac{a}{b \tan t} \Rightarrow \tan t = \frac{a}{b \tan \theta_2} \quad (3)$$

By putting Equation (2) and (3) into Equation (1), we have:

$$\begin{aligned}
\sin^2 \theta_0 &= (a^2 \cos^2 t + b^2 \sin^2 t) \sin^2 \theta_2 \\
&= \frac{a^2 + b^2 \tan^2 t}{1 + \tan^2 t} \sin^2 \theta_2 \\
&= \frac{b^2 a^2 (1 + \tan^2 \theta_2)}{b^2 \tan^2 \theta_2 + a^2} \frac{\tan^2 \theta_2}{1 + \tan^2 \theta_2} \\
&= \frac{b^2 a^2 \tan^2 \theta_2}{b^2 \tan^2 \theta_2 + a^2}
\end{aligned} \tag{4}$$

Where the following trigonometric functions are used:

$$\left. \begin{aligned}
\sin^2 \beta &= \frac{\tan^2 \beta}{1 + \tan^2 \beta} \\
\cos^2 \beta &= \frac{1}{1 + \tan^2 \beta}
\end{aligned} \right\} \beta \text{ represents } t \text{ or } \theta_2 \tag{5}$$

Utilizing both Equation (4) and Equation (2), then:

$$\begin{aligned}
\theta_2 &= \tan^{-1} \left(\sqrt{\frac{a^2 \sin^2 \theta_0}{b^2 (a^2 - \sin^2 \theta_0)}} \right) \\
|OK| &= \frac{b^2 a^2 (1 + \tan^2(\theta_2))}{b^2 \tan^2(\theta_2) + a^2}
\end{aligned} \tag{6}$$

Corresponding to the index ellipse of the single crystal sapphire, where

$$a = n_o$$

$$b = n_{eo}$$

$$|OK| = n_e$$

n_{eo} is a special n_e value, it is the n_e for the normal incident light wave to the surface of the A-plane sapphire disk. Then Equation (6) is then converted into:

$$\begin{aligned}
\theta_2 &= \tan^{-1} \left(\sqrt{\frac{n_o^2 \sin^2 \theta_0}{n_{eo}^2 (n_o^2 - \sin^2 \theta_0)}} \right) \\
n_e &= \frac{n_{eo}^2 n_o^2 (1 + \tan^2(\theta_2))}{n_{eo}^2 \tan^2(\theta_2) + n_o^2}
\end{aligned} \tag{7}$$

These refraction angles and refractive indices are corresponding to the extraordinary waves with incident angle θ_0 in the single crystal sapphire.

Appendix B: Acronym

A/D card	Analog/Digital card
A/D converter	Analog/Digital converter
AC signal	Alternating Component signal
BPDI	Broadband Polarimetric Differential Interferometry
CCD	Charge Coupled Device
CPT	Center for Photonics Technology, Virginia Tech
CPU	Central Processing Unit
CTE	Coefficient of Thermal Expansion
DC	Direct Component
SOP	State of Polarization
GUI	Graphic User Interface
LED	Light Emitting Diode
OPD	Optical Path Difference
PS	Polarimetric Structure
EFPI	Extrinsic Fabry-Perot Interferometry
EMF	Electromotive Force
EMI	Electromagnetic Interference
FFT	Fast Fourier Transform
FP	Fabry-Perot
FWHM	Full Wavelength Half Maximum
IGCC	Integrated Gasification Combined Cycle
IR	Infrared Radiation
NA	Numerical Aperture
PMD	Polarization Mode Dispersion
RMS	Root-Mean-Square
RTD	Resistance Temperature Detector
SP	Sapphire prism
SDZP	Sapphire Disk Zirconia Prism

SNR	Signal Noise Ratio
SCIIB	Self-Calibrated Intensity/Interferometric Base
UV	Ultraviolet
USB	Universal Serial Bus

VITA

Yibing Zhang was born in China, 1973. He received his BS degree in physics in 1995 and MS degree in optics in 1998 from Nankai University, China. From 1998 to 1999, he studied Physics at Washington State University (WSU), and did research with Dr. Philip L. Marston on light scatterings at the Physical Acoustics and Optics laboratory, Department of Physics, WSU. He joined the Center for Photonics Technology at Virginia Polytechnic Institute and State University (Virginia Tech) in 2000. He has been working in the field of laser technologies for high-power laser and ultra-short laser pulse generations, photonic components (FBG, EDFA, fiber coupler, modulator, etc) design and implementation at the system level. Since 2000, he has worked on optical fiber sensors, optical fiber communication devices, and 3-D optical imaging systems for biomedical applications, and optical metrologies for environmental evaluation and material measurements. He is one of the winners of the Paul E. Torgersen Graduate Student Research Excellence Awards for year 2003, College of Engineering, Virginia Tech.